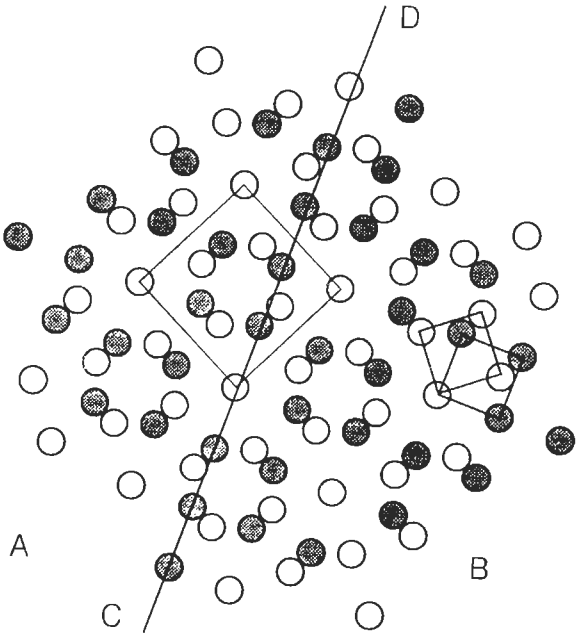

Fig. 1. Coincidence site lattice (Σ5) formed by interpenetration of two crystals. The unit cell of the CSL is outlined to the left, and the linear transformation relating the two lattices is shown on the right.

Coincidence Site Lattice, CSL.

Boundaries are classified according to the ratio of the volume of a unit cell of the CSL to the volume of a unit cell of A or B. This value is denoted by Σ. Thus a low value of Σ implies a high frequency of coincidences of the interpenetrating lattices, and at the other extreme, $\Sigma = \infty$ implies a completely incommensurate orientation. Boundaries with a relatively low (i.e., unambiguously measurable) value of Σ are referred to as *coincidence boundaries* and are sometimes associated with special properties. A boundary plane (e.g., CD in fig. 1) which is also a plane of the CSL has a certain planar density of coincidence sites Γ per unit area. The area $1/\Gamma$ is geometrically important. For CSL boundary planes, periodically repeating unit cells of the bicrystal can be defined (unit cells of the CSL) whose faces pave the boundary. An early idea was that boundaries with a high Γ would have a low free energy because the atoms occupying coincidence sites are in their bulk equilibrium positions relative to either crystal lattice.

2.2.1.2. O-lattice. A generalization of the CSL can be made and is called the *O-lattice*. Let us start with two ideal interpenetrating lattices A and B coinciding at one point which we take as the origin (fig. 2).

Consider a linear homogeneous mapping which brings A into complete coincidence with B at every site. In the simplest case, the mapping is a pure rotation or a shear. As all coincidence sites are completely equivalent, any one of them could be regarded as the origin of the transformation. In general, there are even more points which could be taken

as the origin of the mapping and all such points together form a set called the set of O-points (fig. 2, O stands for Origin) (BOLLMANN [1970]). A conceptual advantage of the O-lattice over the CSL is that the set of O-points moves continuously as crystal A is rotated or deformed with respect to crystal B, whereas CSL points disappear and appear abruptly. There are O-points even when there are no coincidences. Lines bisecting the array of Opoints in the boundary can be geometrically regarded as the cores of dislocations which accommodate the misfit. There is thus a close relationship between the O-lattice and the geometrical theory of interfacial dislocations (BOLLMANN [1974]) (fig. 2b). Such geometrical dislocations are a mathematical device, and do not necessarily correspond to physical dislocations, which are observable atomic structures. The principal utility of an O-lattice construction is that it enables the geometrical location and Burgers vectors of interfacial dislocations to be discussed. A weakness in the concept of an

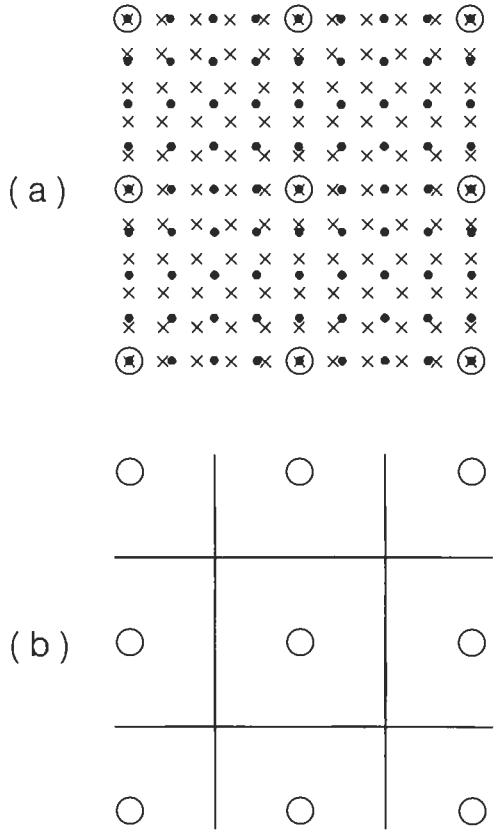

Fig. 2. An (001) projection of the O-lattice between two simple cubic lattices, called lattice A and B in the text, with different lattice parameters. (a) The atoms of each crystal are represented by dots and crosses and the O-points are circled. (b) Showing the lines midway between the O-points which can be geometrically regarded as the cores of dislocations. (After SMITH and POND [1976].)

O-lattice stems from the fact that for a given orientation of A and B, the transformation which brings A into coincidence with B is not representable by a unique matrix. This non-uniqueness is why one must be cautious about attaching any physical significance in terms of observable dislocations to the mathematical dislocations defined by means of the O-lattice.

2.2.1.3. DSC lattice. Another lattice which is of importance for the discussion of isolated dislocations and steps at boundaries is called the DSC lattice, sometimes referred to as *Displacement Shift Complete* (BOLLMANN [1970]) (fig. 3). This is defined as the coarsest lattice which includes the lattices of A and B (in an orientation for which there is some coincidence) as sublattices. Any vector joining a lattice point of crystal A to a lattice point of crystals A or B, and vice versa, is also a vector of the DSC lattice. Thus if either lattice is translated by a DSC vector, the complete pattern of the interpenetrating lattices and the CSL is either invariant or is simply displaced by the same vector. The DSC lattice is unique to the given orientations of A and B and is useful for predicting or explaining the observable (physical) dislocations in boundaries.

2.2.2. Coincidence models

The first attempt to correlate predictively the crystallographic parameters of a boundary (e.g., the lattice structure of the crystals forming the interface, the orientation relationship between the two crystals, the boundary inclination, etc.) with the actual atomic arrangement in the interface was made by KRONBERG and WILSON [1949] who

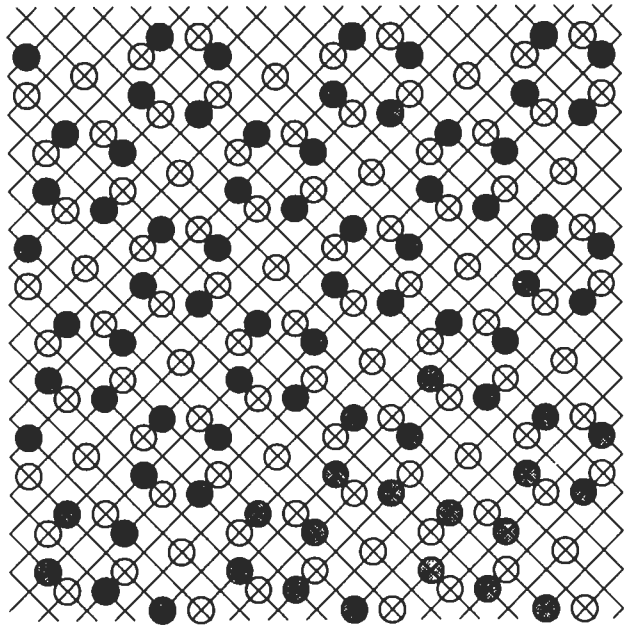

Fig. 3. The DSC lattice corresponding to the interpenetrating lattices illustrated in fig. 1. The DSC lattice points are the points of the fine grid.

applied the concept of lattice coincidence — which was developed independently by several crystallographers — to grain boundaries. An example of a coincidence lattice was shown in fig. 1.

It was also at this time that boundaries with "low" values of Σ were called "special" and all other boundaries were called "random" or "general". No limit on Σ for "special" boundaries was given. Hard-sphere models suggested that every atom at the boundary was at a site of one of the crystals or at a site common to both crystals. This led to the supposition that low-Σ boundaries had low energies because they contained high densities of atoms at shared sites. Such reasoning embodied the "coincidence model" of grain boundaries. BRANDON *et al.* [1964] subsequently pointed out that not all boundaries in a given coincidence system had the same density of coincidence sites. In fact, the density depends on the plane of the boundary. Indeed, one can always find boundaries in any coincidence system with extremely low densities of coincidence sites. They therefore proposed that the planar density, Γ, of coincidence sites in the plane of the boundary should be a more reliable indicator of low energy than Σ. This became known as the *planar coincidence site density*, or Γ *criterion*. Two arguments were given in support of this criterion: in a boundary with a high value of Γ there are more atoms at shared sites and hence the boundary "core" energy is lower. Secondly, by St. Venant's principle, the strain field of the boundary extends into the grains roughly as far as the period of the boundary structure: the higher Γ the smaller the period, and, hence, the lower the strain field energy. BRANDON *et al.* [1964] also extended the planar coincidence to non-coincidence boundaries by combining it with the dislocation model (§ 2.2.1.1).

Boundaries between crystals deviating from an ideal coincidence-orientation relationship were proposed to consist of areas with an array of coincidence atoms in the plane of the boundary (boundary coincidence) separated by (misfit) dislocations. The significance of boundary inclination was incorporated in the model by suggesting that the boundary follows the planes containing a high density of coincidence sites in order to minimize the misfit, as the boundary consists in these regions of atomic groups with little strain. Boundaries constrained to lie at an angle to the most densely packed coincidence-plane were visualized as taking a step structure.

2.2.3. Structural unit models

The concept of atoms occupying coincidence sites (in terms of boundary or lattice coincidences) had to be abandoned after it was discovered by means of computer simulations of the atomic structure of grain boundaries (WEINS *et al.* [1971]) that two crystals forming a coincidence boundary relax by a shear-type displacement (*rigid-body relaxation*) from the position required for the existence of coincidence-site atoms at the boundary (figs. 4a and b). This conclusion was confirmed in subsequent years by numerous more sophisticated computer simulations as well as by experimental observations.

The physical reason for the rigid-body relaxation may be seen from figs. 4 and 5. Figure 5 shows the boundary structure predicted by the lattice-coincidence model. Both closely and widely spaced pairs of atoms exist, resulting in a high-energy structure. The energy of the boundary may be lowered by translating the two crystals (without rotation) so that the "hills" on the "surface" of one crystal coincide with the "valleys" on the

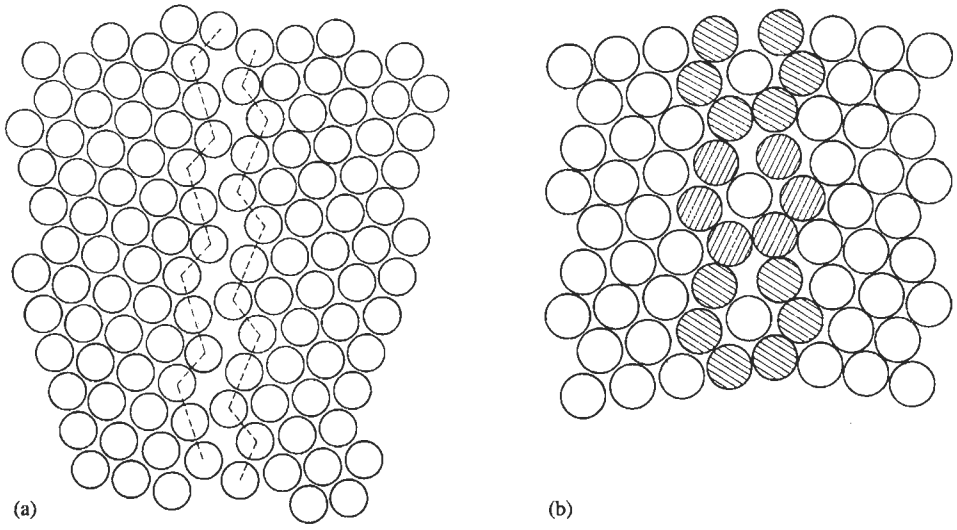

Fig. 4. Structure of the boundary shown in fig. 5 after a "rigid-body relaxation" of the two hexagonal arrays of atoms in order to remove large interatomic repulsion or attraction forces (a) and subsequent relaxation of individual atoms into positions of minimum energy (b). The interaction potential assumed between the atoms corresponds to gold. (From WEINS *et al.* [1971])

"surface" of the other crystal (fig. 4a) followed by the relaxation of individual atoms into minimum-energy positions (fig. 4b). The existence of rigid-body relaxations led CHALMERS and GLEITER [1971] to propose that the *boundary periodicity* rather than the existence of boundary coincidence per se is the physically meaningful parameter. In fact, the existence of small structural units with an atomic packing density comparable to that in a perfect lattice was hypothesized to result in low-energy boundaries (fig. 4b). By extending the structural unit concept originally proposed by BISHOP and CHALMERS [1968] for unrelaxed coincidence boundaries to boundaries with atomic relaxations, the following (relaxed) structural unit model of grain boundaries was put forward (CHALMERS and GLEITER [1971]): boundaries of low energy consist of only one type of (relaxed) structural units, whereas the structure of high-energy boundaries may be derived from a simple rule of mixing of the low-energy structural units of the nearest low-energy boundaries (GLEITER [1971]). This boundary model has been worked out in detail for different types of boundaries (POND and VITEK [1977]). One of the limitations of the model is its applicability to interpolate between two structures of short-periodic boundaries. When the misorientation between two crystals forming a boundary consisting of a mixture of different structural units is described in terms of an axis and an angle of rotation of one crystal relative to the other, and when the rotation axis is of high indices, the Burgers vector of secondary dislocations associated with the minority units may become unrealistically large. "Unrealistically large" means that the dislocation is unlikely to be localized within the minority unit unless the minority unit itself is large. If the dislocation is not localized then the assumption of the model, that local misorientation

References: p. 935.

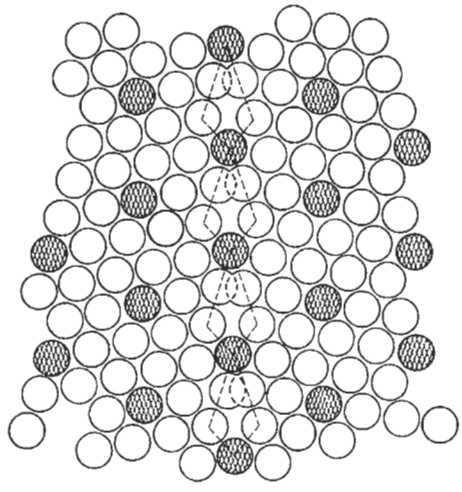

Fig. 5. Lattice-coincidence model of a 18° tilt-type grain boundary between two hexaqonal arrays of atoms. The atoms at coincidence sites are indicated by cross-hatching. The "surfaces" of the two crystals are marked by dashed lines.

changes occur so as to introduce structural units from other boundaries, breaks down. On the other hand, if large minority structural units are required then the misorientation range between the majority and minority structural unit boundaries is small and the predictive capacity of the model is limited. In practice this means that the model may usefully be applied pure tilt and pure twist boundaries with rotation axes of relatively low indices, i.e., <100>, <110>, <111> and possibly <112>.

A few years after the discovery of *quasiperiodicity* in crystals, the same concept was utilized to model grain and interphase boundaries (RIVIER [1986], GRATIAS and THALAL [1988], SUTTON [1989]) see ch. 4, Appendix). The simplest way to visualize quasiperiodicity at an irrational grain boundary is to apply the structural unit model to an irrational tilt boundary. Along the tilt axis (which is assumed to be rational) the structure of the boundary is periodic. However, perpendicular to the tilt axis in the boundary plane the boundary structure will be an aperiodic sequence of majority and minority structural units.

2.2.4. Broken bond model

While for free surfaces a broken-bond description of the structure-energy correlation has been commonly used for over half a century (HERRING [1953]), such an approach has only recently been adopted for grain boundaries, by WOLF and YIP [1992]. In an otherwise perfect crystal, thermal disorder is responsible for a broadening and shift of the interatomic spacings towards larger distances. Owing to the presence of planar defects, polycrystals are structurally disordered even at zero temperature, and their zero-temperature radial distribution function shows the same two effects. However, because of its localization near the interface, this type of disorder is *inhomogeneous,* by contrast with thermal disorder.

To illustrate this inhomogeneity in the direction of the interface normal, let us consider the radial distribution function (or the planar structure factor) for each of the atom planes near the interface. As seen from fig. 6 for the case of a symmetrical (100) twist boundary in the fcc lattice, the amount of structural disorder decreases rapidly from one (100) plane to another, indicating the existence of large gradients in structural disorder. Starting from the description of structural disorder in terms of the radial distribution function, $G(r)$, a broken-bond model seems to present a useful step towards simplification. By characterizing the atomic structure in terms of the number of broken nearest-neighbor (nn) bonds per unit area, essentially in a broken-bond model the detailed peak shapes in $G(r)$ are simply replaced by the areas under these peaks. Because all the

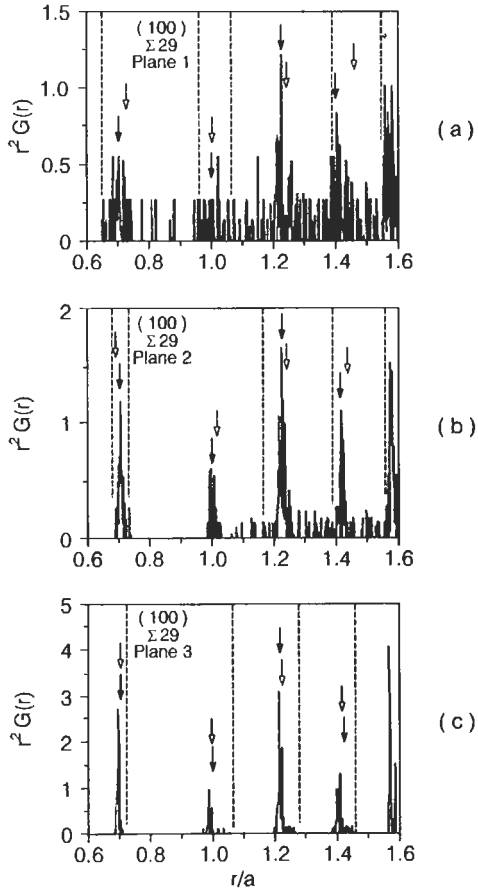

Fig. 6. Plane-by-plane zero-temperature radial distribution functions, $r^2G(r)$, on the three lattice planes closest to the (001) $\theta = 43.60°$ ($\Sigma 29$) symmetrical twist boundary simulated by means of an embedded atom potential for Cu. The full arrows indicate the corresponding perfect-crystal -δ-function peak positions; open arrows mark the average neighbor distance in each shell. The widths of these shells are indicated by dashed lines. (From WOLF and YIP [1992].)

References: p. 935.

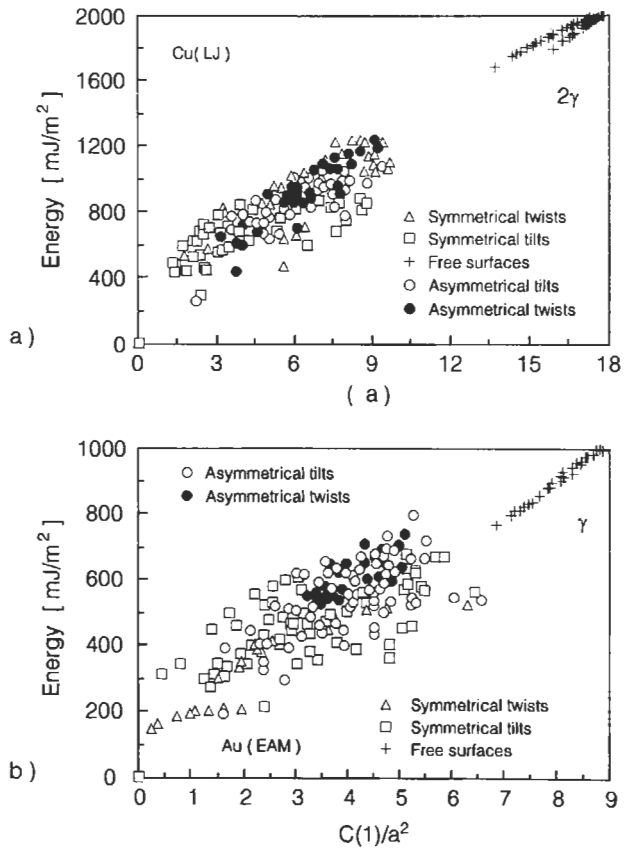

Fig. 7. Grain-boundary energy (mJ/m^2) versus number of nearest neighbor bonds per unit area, $C(1)$. The unit area is normalized by the lattice constant, a. The computations were performed for a Lennard–Johnes potential fitted to Cu (fig. 7a) and an embedded atom potential fitted to Au (fig. 7b). a is the lattice parameter. For comparison, the related free surface energies, γ, are also shown. (From WOLF and YIP [1992, p. 139].)

information contained in the detailed shapes of these peaks is thus lost, small long-range elastic strain-field effects associated, for example, with interface dislocations or surface steps are therefore not 'seen' in the coordination coefficient. This is an inherent limitation of a broken-bond model. Figure 7 indicates the correlation between the average number of broken nn bonds per unit grain boundary area, $C(1)$, and the grain boundary energy for the two fcc potentials (WOLF [1990]). While, in principle, more distant neighbors should also play a role, in fcc metals their contribution was found to be rather small (typically about 10–20% of the nn contribution). By contrast, in bcc metals the second-nearest neighbors were found to be practically as important as the nearest neighbors.

2.2.5. Dislocation models

The idea of modelling a high-angle grain boundary in terms of an array of closely spaced dislocations (fig. 8b, READ and SHOCKLEY [1950]) is an extension of the well established structure of small-angle boundaries (fig. 8a). If the dislocations are uniformly spaced in the plane of the boundary, a low-energy interface is formed because the strain fields of the dislocations extend into the lattices of both crystals over a distance comparable with the spacing of the dislocation array (St. Venant's principle), which is a relative minimum for periodic arrays. A uniform dislocation spacing can only result if the dislocation spacing is equal to an integral number of lattice planes terminating at the boundary. For all other tilt angles the boundary may be described as a boundary with a uniform dislocation spacing (e.g., a 53° tilt boundary, fig. 8b) and a superimposed small-angle tilt boundary that accounts for the deviation from the tilt angle required for uniformly spaced dislocations (fig. 8c). The idea of describing a boundary which deviates from a low-energy structure in terms of the superposition of a low-energy boundary and a small-angle boundary has been increasingly used in association with dislocation models as well as with boundary models that are not based on the dislocation concept.

The work of READ and SHOCKLEY, which is generally considered as a major achievement of the theory of interfacial structures, suffers from two inherent limitations. First, the singular behavior of the elastic strain fields near the dislocation centers was dealt with by removing the singularity mathematically with an inner "cut-off" radius. The second deficiency is the linear superposition of the strain fields of the individual dislocations, which results in complete neglect of the interactions among the dislocations in the array.

In order to ameliorate these deficiencies, the cores of dislocations in grain boundaries were modelled either by a hollow-core dislocation description (LI [1961]), by picturing the material in the core region as a second phase (MASAMURA and GLICKSMAN [1974]), or by assuming the dislocation cores to merge into a slab of core material. A special case of the latter group of boundary models is the "random grain boundary model" (WOLF [1991]). It applies to high-angle twist boundaries. From an investigation of the role of the plane of the boundary relative to the crystallographic orientation of both crystals it was concluded that two types of boundaries should be distinguished in metals with a bcc structure. If the boundary plane is parallel to a set of widely spaced lattice planes, the boundary behavior (energy, cleavage fracture energy, etc.) is governed by the interplanar lattice spacing only. In this case, the interaction of the atoms across the interface is independent of the relative orientation of the two crystals. This suggestion is based on the physical reasoning (WOLF and YIP [1992]) that atoms are shoved more closely together when creating a twist boundary on a plane with small rather than large interplanar spacings. As a consequence of the short-range repulsion between the atoms, the bicrystal then expands locally at the grain boundary, and this expansion is largest for the grain boundaries with the smaller interplanar spacings, resulting in boundaries with higher grain-boundary energy. More precisely, two criteria for low interfacial energy were suggested (WOLF [1985]). The first criterion applies to twist boundaries: On a given lattice plane local minima in the energy vs twist angle relationship are expected at twist angles corresponding to the "locally smallest" CSL unit-cell area. The second criterion

References: p. 935.

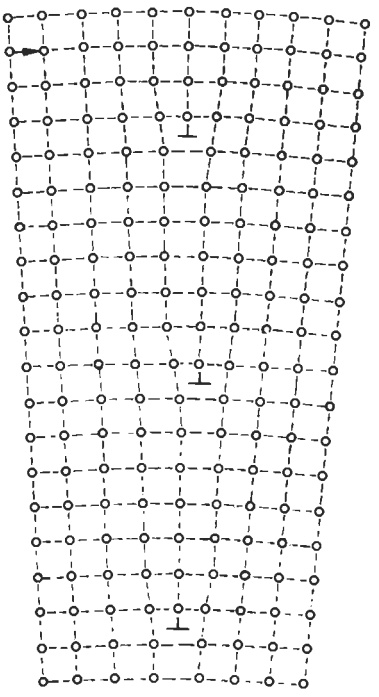

(a)

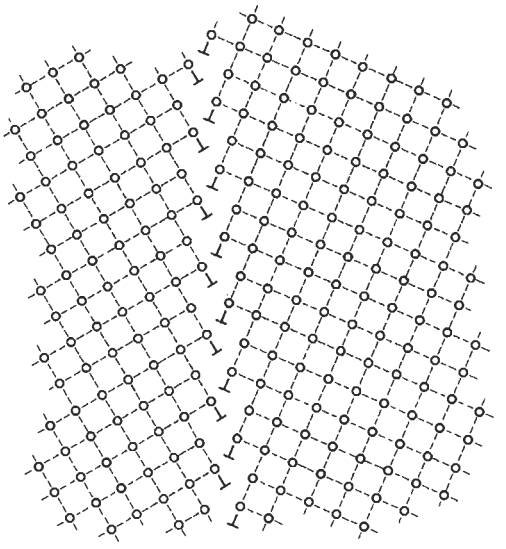

(b)

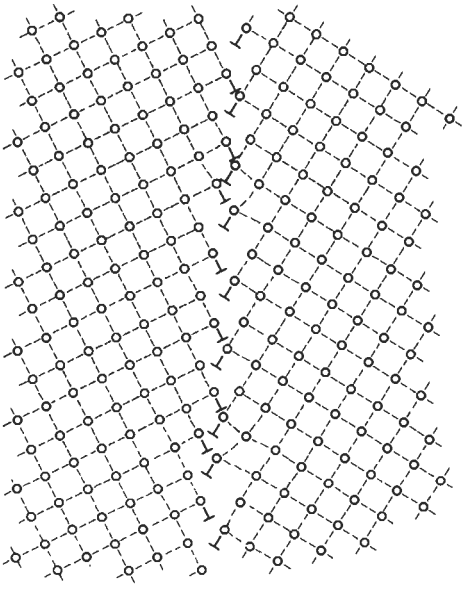

(c)

Fig. 8. Dislocation models of symmetrical tilt boundaries in a simple cubic structure: (a) small-angle boundary; (b) 53° (high-angle) boundary; (c) 60° boundary.

applies to tilt boundaries. This criterion states that local minima in the energy vs tilt angle relationship correspond to planes with "locally large" interplanar spacing. Thus, for symmetrical tilt boundaries high values of d(hkl) are suggested to correspond to local minima in the energy vs tilt angle relationship. In order to see that Wolf's criterion of the interplanar spacing is distinct from the criterion of a high density of coincidence sites (§ 2.1.1) in the boundary plane (Γ), let us consider non-periodic grain boundaries. There are no exactly periodic {111} {100} grain boundaries, for example. Thus, for all {111} {100} boundaries $\Gamma = 0$, whereas the interplanar spacing would attain a relatively high value.

The arguments discussed so far do not apply to grain boundaries on vicinal planes. Vicinal planes are planes that deviate little from the widely spaced ones. In this case, the "surfaces" of both crystals forming the boundary contain a pattern of ledges. In the case of boundaries of "vicinal" planes, the energy of the boundary will depend on the degree of matching between the two ledge patterns. The spacing of the lattice planes is of little relevance (see also ch. 20, § 6).

2.2.6. Polyhedral unit models

The concept of describing the atomic arrangements in grain boundaries in terms of densely packed atomic groups (e.g., the groups existing in amorphous structures) led to the development of the *polyhedral unit models.* Apparently, the idea of comparing the atomic arrangements in a grain boundary with the atomic arrangements existing in amorphous structures was first proposed by POTAPOV *et al.* [1971]. They analyzed the three-dimensional atomic structure of grain boundaries in tungsten by means of field-ion microscopy. Boundaries were found to consist of periodically arranged rings formed by five atoms with a central atom between the rings (fig. 9). On the basis of these observations it was concluded that a grain boundary may be represented in terms of the atomic configurations existing in amorphous metals. Some years later, a similar structural concept was worked out in detail by several other authors (ASHBY *et al.* [1978] and POND *et al.* [1978]). For example, fig. 10 shows the interpretation of the structure of a 36.9° [100] tilt boundary between fcc crystals in terms of the polyhedral unit model.

The comparison between grain-boundary structures and structural elements of amorphous materials is not without problems as the atoms in a boundary cannot relax to the same extent as in a glass. In an interface, the boundary conditions are given by the periodic structure of the two crystals on both sides, whereas an atomic group in a glass has no such periodic boundary conditions for its relaxation. This difference is borne out by several experiments. For example, positron annihilation measurements (CHEN and CHANG [1974]) and Mössbauer studies (OZAWA and ISHIDA [1977]) suggest that the atomic packing in grain boundaries is more "open" than in a glassy structure. This conclusion is supported by recent studies of the atomic arrangements in the interfaces of nanostructured materials (§ 5 of this chapter). Investigations of the atomic arrangements formed in the grain boundaries of nanostructured metals (e.g., by means of density measurements, X-ray diffraction, thermal expansion and various types of spectroscopies) suggest that the atomic structures of glasses differ from those of grain boundaries.

References: p. 935.

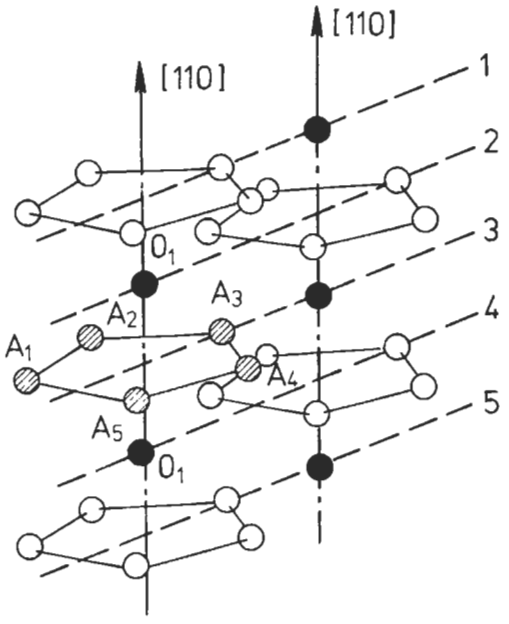

Fig. 9. Schematic diagram of the arrangement of the atoms in a 40° < 110> tilt boundary in tungsten, derived from a sequence of field-ion microscopy images. The position of the < 110 > common tilt axis in the two grains is indicated. Numbers 1–5 indicate subsequent layers of the boundary. Letters A_1–A_5 label one of the polyhedral rings proposed by POTAPOV *et al.* [1971].

2.2.7. Limitations of existing models

A detailed comparison of the experimental observations (SUTTON and BALLUFFI [1987]) indicates that none of the above models seems to predict the boundary energy reliably in all cases, i.e., for metal/metal, ionic/ionic and metal/ionic interfaces. Apparently, no geometric criterion can enshrine the universal answer to the question about the atomic structure of intercrystalline interfaces. This is not surprising since a severe shortcoming of all existing boundary models is the neglect of electronic effects. In fact, studies (HERRMANN *et al.* [1976] and MAURER *et al.* [1985]) of low-energy boundaries in metals with the same lattice structure but different electronic structure suggest a division of all low-energy boundaries into two groups: "electron-sensitive" and "electron-insensitive" boundaries. Physically, this different behavior was interpreted in terms of the different atomic arrangements in the boundaries. If the atomic arrangement is similar to the lattice structure (e.g., in a twin boundary), the boundary energy is low irrespective of the contribution of the conduction electrons to the boundary energy. However, for boundaries with complex atomic structures, the electronic contribution to the boundary energy is crucial so that any difference in the electronic structure (e.g., two materials with different Fermi energies) leads to different boundary behavior. In fact, free-electron calculations showed that the positive charge deficit associated with a grain boundary may

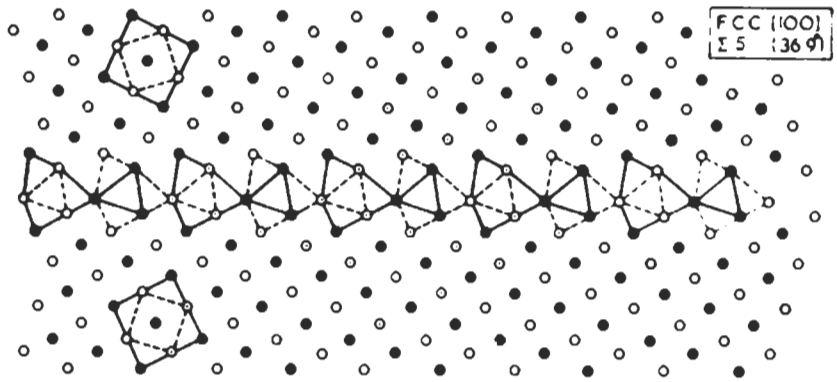

Fig. 10. Structure of a 36.9° < 100 > tilt boundary between fcc crystals, in terms of polyhedral units. The boundary is composed of stacks of capped trigonal prisms.

be the dominant part of the boundary energy (SEEGER and SCHOTTKY [1959]).

A first *ab initio* solution of the electronic and atomic structures of a $\Sigma = 5(001)$ twist grain boundary in Ge was performed recently by PAYNE *et al.* [1985] by means of the Car–Parrinello (CAR and PARINELLO [1985]) method. In this method one solves for both the electronic wave functions and the ion positions. The only approximations made in these computations were the use of a local pseudopotential for Ge, the local density approximation for the exchange–correlation potential, and a large but finite number of plane wave basis functions. By modern standards this is a first principles calculation. One of the interesting features reported was that a contraction could occur at the boundary and was associated with a relatively low energy. This is contrary to the common experience with grain boundaries in metals. As the boundary region becomes denser, five-fold coordinated atoms may arise, and this was indeed reported. With only 4 valence electrons per atom, the system cannot form the same type of bond to a fifth neighbor as it has already established to four neighbors. Instead, rehybridization must take place. We might expect a five-fold coordinated atom to cost less energy than a three-fold coordinated atom since the former represents a smaller perturbation to the tetrahedral bond order. These ideas have been developed further by SUTTON [1988], who proposed a bond-angle distribution function to characterize the boundary structure.

A further shortcoming of existing boundary models is their limited ability to account for temperature effects. The significance of temperature for the structure and properties of interfaces was demonstrated experimentally several years ago (e.g., ERB *et al.* [1982]). The *influence of temperature* on the stability and structures of interfaces has been modelled by a number of groups and was recently reviewed critically by PONTIKIS [1988]. Molecular dynamics and Monte Carlo techniques have been employed and attention has focussed on disordering of the boundary region through roughening or premelting. Such disordering processes are nucleated by thermal fluctuations. However, many thermal properties of a grain boundary like those of a perfect crystal do not depend on thermal fluctuations but on thermal vibrations averaged over a long period of time,

e.g., such as the thermal expansion coefficient, specific heat and elastic constants. As little is known about these boundary properties, it is difficult at present to evaluate the relevance of the above computations.

A great deal of information about the atomic structure of grain boundaries has been deduced by means of *computer simulations*. All simulations ultimately rest on the assumptions they make about *interatomic forces*. The majority of simulations assume some form of potential to describe atomic interactions. For simple s–p bonded metals, e.g., Li, Na, K, Mg, Al, such interatomic potentials can be derived rigorously from the electrostatics of interacting spherical screening clouds of electrons called pseudopotentials. The presence of d-electrons at or near the Fermi level spoils this simple linear screening picture. For substances of this kind pairwise potentials have been generated by fitting more or less arbitrary functions to bulk properties such as cohesive energy, lattice parameter, elastic constants and vacancy formation energy. A more realistic class of potentials for transition and noble metals goes beyond the purely pairwise description of the interaction. They are referred to as isotropic N-body potentials. They are derived from a simplified tight-binding description of electronic densities of states. The next step up the ladder of realism in metallic solids takes us to *3- and 4-body potentials* and to *tight-binding models* beyond the second-moment approximation. For insulators, simulations have used the Born model in which the cohesive part of the total energy is the pairwise summation of the Coulomb interaction of the ions. This is counterbalanced by a short-ranged repulsive energy which is either fitted to the lattice parameter and bulk modulus of the perfect crystal or determined by the *electron gas method*. In semiconductors, a number of empirical angular-dependent interatomic potentials have been developed, motivated by the stability of the fourfold coordination which results from sp^3-hybrid bonds. None can be regarded as completely reliable for structural predictions since they are fitted to bulk properties, and the energy associated with dangling bonds or rehybridization remains poorly represented. In semiconductors, ab initio pseudopotential methods have made rapid progress since 1985, when CAR and PARRINELLO [1985] showed how the Schrödinger equation could be solved for the wave functions with a simultaneous adjustment of the positions of the ions — either to solve their equation of motion or to minimize the total energy. (For further details see ch. 2).

On the experimental side, the most important sources of structural information about interfaces are *high-resolution electron microscopy* (HREM) and *X-ray diffraction* studies. A major experimental problem with X-ray diffraction studies is the fact that boundary scattering is relatively weak. For example, for a $\Sigma 5[001]$ twist boundary in Au the intensity of the weaker diffracted beams of the boundary region corresponds to about 4% of a monolayer of Au. In addition to the resulting poor signal-to-noise ratio, the presence of forbidden lattice reflections, double diffraction from the crystals adjoining the boundary, and scattering from free surfaces enhances the difficulties of obtaining reliable structural information (SASS [1980], SASS and BRISTOWE [1980], FITZSIMMONS and SASS [1988].

A promising new technique for studying interfaces by X-rays recently became important. This scattering of X-rays at grazing angles is called *grazing incidence X-ray scattering*, GIXS (MARRA *et al.* [1979] and EISENBERGER and MARRA [1981]). In this

technique, a grazing-incidence X-ray beam of high intensity is reflected not only by the bulk material, but also by the reflectivity of interfaces buried slightly underneath the surfaces. By fitting the computed and measured X-ray reflectivity curves, information about the density profile across an interface may be obtained. GIXS studies require relatively large sample areas (typically 0.2 cm × 1 cm) under which an interface is buried. The GIXS study averages over this area. In other words, films of extreme homogeneity are required. Those films can only be obtained so far for epitaxial layers of semiconductors or metals grown on rigid substrates such as semiconductors or ceramics.

Modern *high-resolution electron microscopes* have point-to-point resolutions of about 0.16 nm. In order to apply HREM to the problem of imagining the atomic structure of interfaces, only thin-film specimens (typical thicknesses 5 to 10 nm) and crystal orientations that result in close packed rows of atoms being parallel to the electron beam are suitable. In addition to these limitations, one has to keep in mind that the image of the boundary structure is a product of the wave field of the boundary in the objective plane and the contrast transfer function (CTF) of the microscope which depends on the lens errors and the focus conditions. In fact, the image of any object imagined in the electron microscope is severely modified by the CTF if electron scattering to large angle occurs since the influence of the spherical increases rapidly with the scattering angle. This effect is crucial for imagining the atomic structure of boundaries. Good imagining conditions are fulfilled for lattices with large lattice parameters. If, however, deviations in the periodicity exist, components of the diffraction pattern of such an object appear at large diffraction vectors (v_L). This applies, for example, most likely to the atomic arrangement in grain boundaries. Hence, the structure of grain boundaries can only be imagined reliably if the oscillating part of the CTF is outside of v_L. Naturally, all HREM studies imply that no structural changes occur during specimen preparation.

2.3. Interphase boundaries

2.3.1. Bonding at interphase boundaries

In comparison to the extensive body of work on grain boundaries, relatively few studies have been directed at the understanding of the structure and properties of interphase boundaries. The bonding between chemically different materials across an interface involves interactions with and without charge exchange. The interaction between induced dipoles (London), between neutral atoms polarized by a dipole (Debye) and dipole/dipole interactions (Keesom) constitute the first group and are summarized as *Van der Waals attractions.* Charge exchange results in the formation of ionic, covalent and metallic bonds. Among the numerous conceivable combinations of materials at interphase boundaries, interfaces between ceramics and transition and noble metals are of particular practical importance. Hence, it is of interest to understand the bonding between them. Most ceramics of technological use today are insulating metaoxides. They bind to a *free-electron-like* metal essentially owing to the Coulomb attraction between the ions of the ceramic and their screening charge density in the metal (STONEHAM and TASKER [1988], FINNIS [1992], FINNIS *et al.* [1990]). This image attraction is balanced mainly by the hard-core repulsion between the ceramic and metal ions and it seems

primarily (DUFFY *et al.* [1992]) the hard-core repulsion which determines the relative positions projected onto the plane of the interface of the ceramic and metal ions, i.e., the parallel rigid-body translation. The model of an electrostatic image interaction stems from the classical concept in the continuum electrostatics of point charges near a conducting surface, and makes no reference to discrete atoms. Hence, it usually has no place in simple models of adhesion based on chemical bonding. Nevertheless, its equivalent attractive force close to a real metal surface can be calculated quantum-mechanically for simple geometries. Fortunately, the results of these quantum-mechanical calculations can be simulated by a classical interatomic force model, suggesting a way to incorporate this effect in computations of the atomic structure of interphase boundaries (FINNIS [1992]).

The binding of a ceramic to a *transition* metal is less understood, since here, strong covalent *pd*-bonds may be formed across the interface between oxygen and the transition atoms (JOHNSON and PEPPER [1982]). The formation of such bonds is supported by the observation that the adhesion correlates with the free energy of oxide formation for the transition metal; both increase in the order Ag → Cu → Ni → Fe ... In this situation, it is remarkable that atomically sharp transition-metal/ceramic interfaces exist without inter-diffusion and formation of a transition-metal oxide layer. Whereas the hard-core repulsion favors translation states with the metal cores above the holes in the top layer of the ceramic, *pd*-bonding pulls the transition atoms on top of the oxygens.

Noble metals have filled, but polarizable *d*-shells so that their binding to a ceramic is presumably of intermediate nature. In this case, the question of the translation state is difficult and there could be several metastable states. Experimental results are lacking and, for the system (001) fcc Ag on (001) MgO, which has the rocksalt structure consisting of two interpenetrating fcc sublattices, the semi-empirical image-charge model predicts (DUFFY *et al.* [1992]) silver to be above the hole between two magnesiums and two oxygens, whereas ab initio electronic density-functional calculations (BLÖCHL *et al.* [1990], FREEMAN *et al.* [1990]) favor silver on top of oxygen.

However, no general prediction seems to be possible at this moment. For example, *ab initio* LDA calculations (SCHÖNBERGER *et al.* [1992]) indicate that the exact atomic positions and the type of bonds formed in interphase boundaries depend on the elements involved. Both Ti and Ag were found to bind on top of the O in Ti/MgO and Ag/MgO interfaces. However, the binding between Ti and O is predominantly covalent and weaker than in bulk TiO; it corresponds to a Ti oxidation state less than +1. The bonding between Ag and O is weak and predominantly ionic. The bond length and force constants resemble those in Ag_2O where the oxidation state of Ag is +1. Whether it is the polarization of the Ag *d*-shell which pulls Ag on top of O, or if this could also happen for an *sp*-metal is not yet known.

The understanding of the fundamental physics involved in the bonding between a metal and a ceramic requires quantum-mechanical models to be developed. The simplest approach involves cluster calculations (JOHNSON and PEPPER [1982]). Such calculations have established that the primary interactions at metal/oxide interfaces involve the metal (d) and oxygen (p) orbitals, to create both bonding and antibonding orbitals. For copper and silver in contact with Al_2O_3, both states are about equally occupied, resulting in zero net bonding. However, for nickel and iron, fewer antibonding states are occupied and net

bonding occurs. The calculations also reveal that a transfer of valence charge occurs, resulting in a contribution to the net ionic bonding which increases in strength as the metal becomes more noble. Consequently, in the case of metal-to-alumina bonding, strengths are predicted to increase in the order: Ag–Cu–Ni–Fe. This order is generally consistent with the measured trends in sliding resistance as well as with the energies of adhesion. However, it is emphasized that the calculations approximate the interface by an $(AlO_6)^{9-}$ cluster and one metal atom. The selection of the charge to be assigned to this cluster is non-trivial and the choice influences the predicted magnitudes of the energies (ANDERSON *et al.* [1985]). To further examine this issue, ANDERSON *et al.* [1987] performed calculations for the Al_2O_3/Pt couple that included more atoms: 31 close-packed platinum atoms and the corresponding numbers of aluminum and oxygen ions. Then, by applying a quantum-chemical superposition technique, including an electron delocalization molecular orbital method, bonding energies were calculated for different atomic configurations of the Pt/Al_2O_3 interface. These calculations confirmed that the bond was strongest when oxidized platinum atoms opposed close-packed oxygen ion planes.

Ab initio calculations seem to be essential for a full understanding of the bonding. LOUIE and coworkers (LOUIE and COHEN [1976], LOUIE *et al.* [1977]) have performed such calculations on metal-semiconductor interfaces. In these calculations, the metal was described by a *jellium*, so that insight emerged regarding the bonding mechanisms, but not on the atomistic structure. More recently, supercell calculations have been carried out that include an interface area and adjacent regions large enough to incorporate the distorted (relaxed) volumes of both crystals. With this approach, the electron distribution around all atoms has been calculated and the atomic potentials evaluated. In a next step, interatomic forces may be calculated and strains determined. Such calculations have been performed rather successfully for the interface between Ge–GaAs (KUNC and MARTIN [1981]) and Si–Ge (VAN DE WALLE and MARTIN [1985]). The crystals adjacent to those interfaces are isomorphous and very nearly commensurate, such that the misfit between lattice planes is very small. However, misfits between metals and ceramics are typically rather large so that extremely large supercells are required.

First attempts in this direction have been made. SCHÖNBERGER *et al.* [1992] performed *ab initio* local density-functional calculations of the equilibrium geometries, force constants, interface energies and works of adhesion for lattice-matched interfaces between rocksalt-structured MgO and a f.c.c. transition or noble metal. The interfaces had $(001)_M \| (001)_{MgO}$ and $[100]_M \| [100]_{MgO}$ (M = Ti or Ag). The full-potential LMTO method was used. Both Ti and Ag are found to bind on top of oxygen. The interface force constants are 3–4 times larger for Ti|MgO than for Ag|MgO. These, as well as the M–O distances, indicate that the Ti–O bonding is predominantly covalent and that the Ag-bonding is predominantly ionic. The calculated interface energies are both 0.8 eV/M|MgO and the interface adhesions are, respectively, 1.2 eV/Ti|MgO and 0.9 eV/Ag|MgO.

With the advent of a new calculational scheme (CAR and PARRINELLO [1985]), involving a combination of molecular dynamics (see, e.g., RAHMAN [1977]) and density-functional theory (KOHN and SHAM [1965]), it should be possible to conduct computa-

References: p. 935.

tions of *relaxed* interfaces much more efficiently. The scheme should also allow equilibrium computations of metal/ceramic interfaces at finite temperatures. The conduct of such analysis on model interfaces should greatly facilitate the basic understanding of the bonding phenomenon and allow judicious usage of both cluster calculations and continuum thermodynamic formulations.

For recent reviews of this area we refer to the articles by RÜHLE and EVANS [1989], FINNIS and RÜHLE [1991] and the Proceedings of an International Symposium on this subject edited by RÜHLE *et al.* [1992].

2.3.2. Chemistry of interphase boundaries

In multicomponent two-phase systems, non-planar interfaces or two-phase product regions can evolve from initially planar interfaces (BACKHAUS and SCHMALZRIED [1985]). The formalism previously developed for ternary systems can be adapted to metal/ceramic couples, with the three independent components being the two cations and the anion. In general, the problem is complicated by having several phase fields present, such that intermediate phases form: usually intermetallics with noble metals and spinels (or other oxides) with less noble metals. The actual phases depend on the geometry of the tie lines, as well as on the diffusion paths in the tenary phase field, and cannot be predicted *a priori*. In general, the following two cases can be distinguished:

2.3.2.1. Interfaces without reaction layers. Detailed scanning electron microscopy and TEM studies performed for Nb/Al_2O_3 (BURGER *et al.* [1987], RÜHLE *et al.* [1986], [1987]) have shown that no reaction layer forms. Concentration profiles revealed that, close to the interface, the concentration of aluminum is below the limit of detectability. However, with increasing distance from the interface, the concentration of aluminum, c_{Al}, increases to a saturation value. The corresponding oxygen content is below the limit of detectability. These measurements suggest that at the bonding temperature, c^*_{Al}, the local concentration of Al at the interface possesses a value governed by the solubility limit. Bonding between platinum and Al_2O_3 subject to an inert atmosphere also occurs without chemical reaction. However, for bonds formed subject to a hydrogen atmosphere containing about 100 ppm H_2O, aluminum is detected in the platinum, indicative of Al_2O_3 being dissolved by platinum (RÜHLE and EVANS [1989]).

2.3.2.2. Interfaces with reaction layers. For systems that form interphases, it is important to be able to predict those product phases created. However, even if all the thermodynamic data are known, so that the different phase fields and the connecting tie lines can be calculated, the preferred product phase still cannot be unambiguously determined. Sometimes, small changes in the initial conditions can influence the reaction path dramatically, as exemplified by the Ni–Al–O systems (WASYNCZUK and RÜHLE [1987]). Under high vacuum conditions (activity of oxygen $< 10^{-12}$) the diffusion path in the extended nickel phase field follows that side of the miscibility gap rich in aluminum and low in oxygen, (path I in fig. 11), caused by the more rapid diffusion of oxygen than aluminum in nickel. This interface composition is directly connected by a tie line to the Al_2O_3 phase field, such that no product phase forms. However, whenever nickel contains sufficient oxygen (about 500 ppm solubility), the Ni(O)/Al_2O_3 diffusion couple yields a spinel product layer. It is noted that the interface between spinel and nickel seems to be

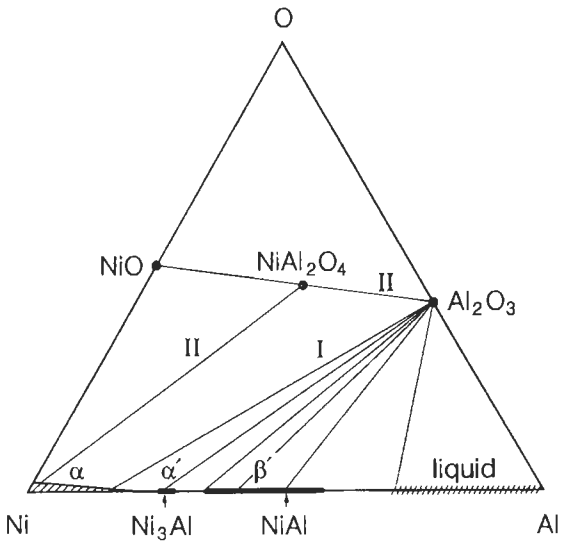

Fig. 11. Ni–Al–O phase diagrams (schematically for T = 1600 K). Two reaction paths are possible when nickel is bonded to Al_2O_3: (I) Low oxygen activity: no reaction product forms, (II) high oxygen activity: spinel forms. (From RUHLE and EVANS [1989].)

unstable, morphological instabilities becoming more apparent with increasing spinel layer thickness. Bonding of copper to Al_2O_3 seems to require a thin layer of oxygen on the surface of copper prior to bonding and $CuAl_2O_3$ or $CuAl_2O_4$ form (WITTMER [1985]). The spinel thickness can be reduced by annealing under extremely low oxygen activities, leading first to a "non-wetting" layer of Cu_2O and then to a direct Cu/Al_2O_3 bond. Bonding of titanium to Al_2O_3 results in the formation of the intermetallic phases TiAl or Ti_3Al, which probably also include oxygen. The thickness of the reactive layer increases with increasing bonding time, and morphologically unstable interfaces develop.

A recent study (JANG *et al.* [1993]) has demonstrated the capability of atom-probe field-ion microscopy to reveal the chemical composition profile across interphase boundaries on an atomic level. By applying this technique to Cu/MgO {111}-type heterophase boundaries along a common <111> direction it was demonstrated that these boundaries are formed by Cu|O|Mg bonds.

Experimental evidence for the formation of reaction layers at interphase boundaries has been obtained by studying nanostructured alloys (cf. § 5 of this chapter). These alloys were synthesized by consolidating nanometer-sized crystals with different chemical compositions, e.g., Ag–Fe, Cu–Bi, Fe–Cu, Cu–Ir, Sn–Ge. Although all systems exhibit little mutual solubility at ambient temperature in the crystalline state, it was found (by X-ray diffraction, EXAFS and spectroscopic methods) that solid solutions are formed at the interphase boundaries. In the case of Ag/Fe this result is particularly remarkable because Ag and Fe are immiscible even in the molten state.

Most structural ceramics are polyphase materials. They are either composites or

different crystalline phases or contain an intergranular vitreous phase in addition to a single crystalline phase. The vitreous intergranular phases can be caused (i) as a result of a liquid-phase sintering process (e.g., in Sialon ceramics, alumina, etc.), (ii) by an incomplete crystallization of a glass (glass ceramic), and (iii) by a condensation of impurities present in the single-phase component at the grain boundaries (e.g., silicates in zirconia).

In the materials noted above, most grain boundaries are covered with a glassy film and, in addition, glass is present at grain junctions. This observation may be explained by considering the energy of the grain boundary as a function of misorientation for crystalline and wetted boundaries. The curve of the interfacial energy vs. misorientation of a crystalline boundary exhibits cusps at the special misorientations. In contrast, the energy curve of the wetted grain boundary should be independent of orientation due to the isotropic nature of the glass. On the basis of such descriptions, low-angle grain boundaries will be free of glass, whereas all large-angle grain boundaries will contain an intergranular glass phase with the exception of "cusp" orientations (the "special" boundaries), as was observed.

2.3.3. Crystallographic structure: "lock-in" model

FECHT and GLEITER [1985] determined relatively low-energy interfaces between noble metal spheres and low-index ionic crystal substrates by the rotating crystallite method. They observed that in the resulting low-energy interfaces, some close-packed directions in the two phases are parallel and some sets of low-index planes are parallel, as well. On the basis of these observations it was concluded that no CSL orientation of low Σ exists in the vicinity of the observed relationships and, therefore, the applicability of the "CSL model" was ruled out for the systems studied. Instead, they proposed the following "lock-in" model: a) relatively low interfacial energy is achieved when a close-packed direction (<110>, <100>, <1100>, <1210>) in the crystal lattice of one phase is parallel to the interface and also parallel to a close-packed direction in the crystal lattice of the adjoining phase and if two sets of relatively low-index lattice planes are parallel to the interface. In this configuration, close-packed rows of atoms in the "surface" of the metal crystal can fit into the "valleys" between close-packed rows of atoms at the "surface" of the ionic crystal in "locked-in" configurations.

Generally, the two phases adjoining the boundary are incommensurate, and unless a small strain is allowed parallel to the interface, locked-in rows of atoms soon begin to ride up the valleys in the interface and cease to lock-in. The lock-in model is not entirely crystallographic in character. Certainly, the conditions for the existence of parallel close-packed directions in the interface and of the interface being parallel to low-index planes are geometrical. But the assumption that, when these conditions are fulfilled, the interface relaxes in such a way that rows of atoms along the close-packed directions form a "locked-in configuration" is equivalent to assuming a particular translation state of the interface is energetically favorable. On the other hand, the planar density of coincidence sites is unaffected by the translation state of the interface. Hence, there is an important distinction between the lock-in criterion and the Γ criterion (cf. paragraph 2.2.2). Discrepancies from the orientation relationships predicted by the "lock-in" model have

been found for interphase boundaries between Nb/Al_2O_3 and Cu/Al_2O_3. Relaxation effects are presumably responsible for these deviations.

3. *Characterization of microstructure*

The basic elements of microstructure are lattice defects and second-phase components. A complete description of the topology and crystallography of the microstructure of a crystalline material requires the following information:

(a) the spacial distribution of the orientation of all crystals;
(b) the characterization of the shape, type, size and spacial distribution of all the elements of the microstructure;
(c) the characterization of the orientation distribution of these elements in space (microstructural anisotropy).

Naturally, all of these parameters can be represented in terms of orientational and spacial correlation functions. Any special feature of a particular microstructure such as a special type of symmetry, self-similarity, order, etc., of all or of some of these elements are enshrined in the correlation functions. In reality, however, the correlation functions are frequently not known because they are difficult to measure. Hence, in most cases, the discussion of microstructural features had to be limited to a few, relatively simple microstructures (HORNBOGEN [1989]). However, in recent years modern on-line data evaluation procedures became available involving, for example, a combination of conventional microscopic methods with an on-line image processing attachment. By means of such systems the spacial orientation distributions of all crystals of a polycrystal can be measured (ADAMS [1993]). This procedure has been termed "orientation imaging microscopy". Similar systems have been developed to characterize the size distribution, shape distribution, etc., of crystallites and other elements of microstructure.

In the straightforward situation of randomly distributed defects and/or second phase particles, the microstructure may be characterized to a first approximation by an average density, ρ, of defects and/or second-phase particles. Depending on the type of microstructural element involved, ρ describes the number of O-dimensional defects (e.g., vacancies) per volume, the total length of one-dimensional defects (e.g., dislocations), the total area of two-dimensional defects (e.g., grain boundaries) per volume, or the total volume fraction of three-dimensional objects (e.g., pores, precipitates). However, even in the simple situation of uniformly distributed microstructural elements, the average defect spacing may not be the appropriate parameter to describe the microstructure. For example, in the case of a polycrystal with equiaxed grains of a narrow size distribution, the use of the average grain size as a length scale implies that all boundaries are the same. As this is mostly not so, a new length scale has to be introduced which accounts for the boundary to boundary variability. This new length scale is given by the clusters of grains linked by grain boundaries sharing misorientations in the same category. In fact, it has been shown that it is this length scale of the microstructure that controls crack propagation and failure of polycrystals (PALUMBO *et al.* [1991a], WATANABE [1984]). The

control of properties of materials by means of controlling the structure of interfaces seems to develop into a separate subdiscipline of materials science termed "interfacial engineering" or "grain boundary design" (WATANABE [1993], HONDROS [1993]). This new discipline is based on the structure-property relationship for individual boundaries and relates the boundary-induced heterogeneity of deformation and fracture of polycrystals to the topological arrangement and the spacial distribution of the character of grain boundaries in polycrystalline materials. It is these parameters that seem to be crucial in controlling the high-temperature plasticity, superplasticity and brittleness. (Ch. 28. § 3.7).

Frequently, the spacial arrangement of the microstructural elements is non-uniform. For example, a non-uniformity in the dislocation density may exist on different length scales; e.g., in heavily cold-worked materials, dislocation cell walls are formed on a nanometer scale whereas in irradiated specimens the formation of helical dislocations introduces roughness on a submicron scale. In some cases an isotropic or anisotropic length scale is required to characterize such microstructures. In other cases this is not so. For example, in some materials fractal microstructures have been reported (e.g., in polycrystalline alloys with localized slip). The significance of fractals in various types of microstructures in metals has been discussed recently by HORNBOGEN [1989].

In multiphase alloys different types of microstructures result depending on the volume fraction, shape and the distribution of the phases (HORNBOGEN [1986], [1989]). For the sake of simplicity let us limit the discussion first to two-phase systems (called α and β phases) with equiaxed grains or particles. In alloys of this type a variety of microstructures can be formed. A convenient parameter to characterize the various microstructures is the density (ρ) of grain and interphase boundaries. In a microstructure called an "ideal *dispersion*" of α particles in a β matrix no α/β interphase boundaries exist (fig. 12a). The other extreme results if the β particles cover all α/α grain boundaries completely. In other words, the α/α boundaries disappear and we are left with α/β interfaces and β/β boundaries the relative density of which depends on the β crystal size (fig. 12c). In both cases, two-phase microstructures (fig. 12b) exist that are characterized by different degrees of percolation of the α and β phases. One way to characterize this type of microstructure (called *duplex structure*) is to determine the relative densities of the α/β, β/β and α/β interfaces. In the ideal duplex structure the ratio between the total number of grain and interphase boundaries is 0.5. In the cases considered so far, the two phases were assumed to have no shape anisotropy. In reality, this is often not so. In order to exemplify the role of anisotropy, a few microstructures with different degrees of anisotropy are displayed in fig. 13 (HORNBOGEN [1984]). Depending on the aspect ratios of the second-phase crystals, a fibrous or lamellar structure may result. Obviously, other anisotropic microstructures are formed if the relative aspect ratios of a duplex or a skeleton-type microstructure are modified.

Microstructural transformations. The well-established scheme of phase transformations in condensed matter systems may be extended in a modified form to the transformation of one type of microstructure to another one. The following three cases have been discussed so far:

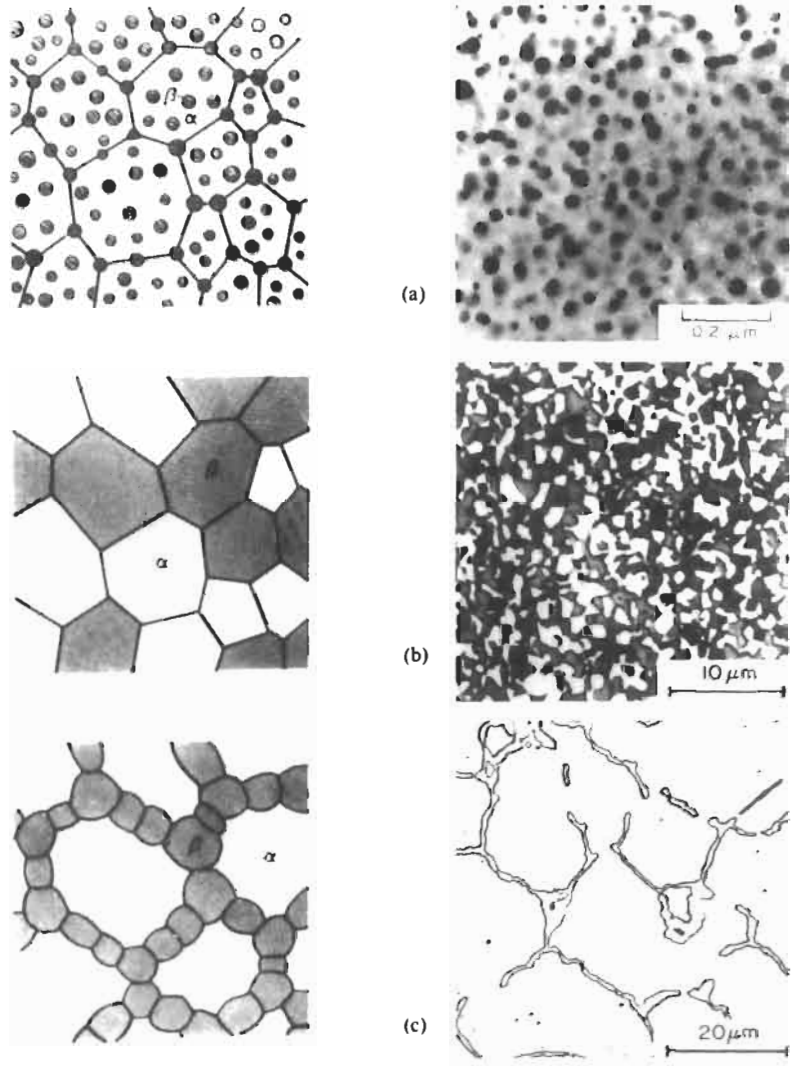

Fig. 12. Principal types of equi-axed two-phase microstructures. (a) Dispersion: Ni+ 18.2Cr+5.7Al, $\gamma+\gamma'$. (b) Duplex: Fe + 9wt%Ni, $\alpha+[\gamma+\alpha_M]$ (austenite transformed to martensite during cooling). (c) Net: Fe+0.6wt%C, $\alpha+Fe_3C$. (From HORNBOGEN [1984].)

a) *Transformation of microstructural elements.* Well known examples for this type of transformation of microstructural elements are as follows. The condensation of single vacancies into dislocation loops, the transformation of small-angle boundaries into high-angle grain boundaries by incorporation of additional dislocations, the incorporation of dislocations into high-angle grain boundaries which transforms them, for example, from a special (low-energy) boundary into a random (high-energy) one (cf.

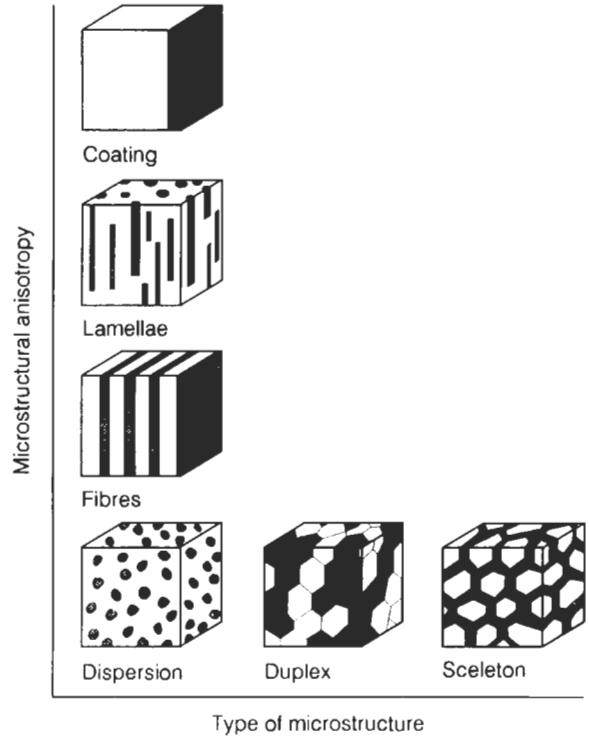

Fig. 13. Different two-phase microstructures depending on the topology of the two phases. (From HORNBOGEN [1984].)

§ 2 of this chapter), the change from coherent to incoherent interphase boundaries during the growth of precipitates are examples of this kind.

b) *Transformation of a crystalline material with a high defect density to a new phase*
Such a transformation may occur if the spacing between microstructural elements (e.g., dislocations, grain boundaries) in a crystal approaches atomic dimensions. If this is so, it may transform into an amorphous phase (OEHRING *et al.* [1992]). The same applies to the shock wave-induced transformation of a crystal into a glass or the dislocation model of melting. In the dislocation model of melting, melting is proposed to occur by the entropy-driven proliferation of dislocations in crystals (KUHLMANN–WILSDORF [1965], COTTERILL [1979], EDWARDS and WARNER [1979], HOLZ [1979]). The phase transition from α to β quartz has been shown to occur by the incorporation of a high density of regularly spaced Dauphiné twins.

c) *Transformations between different types of microstructures*
Transformations of this type are defined by the appearance of new microstructural elements. Two-phase microstructures shall serve as examples for such transformations. A transformation of one type of microstructure to another is associated with

the appearance or disappearance of a particular type of boundary which represents a characteristic topological feature. Transformations can take place as a function of volume fraction of the phases, and of their shape and orientation. For constant shape- and size-distribution, the transformation must take place at a critical volume fraction, f_r. This in turn leads to relations with alloy composition x and annealing temperature T and with the equilibrium phase diagram. Figure 14 shows two-dimensional representations of the following transformations: duplex ⇋ dispersion and net ⇋ dispersion.

Microstructural transformations are found not only under conditions of phase equilibrium, but also if the volume fractions change after nucleation and finally when an equilibrium value is approached. The first stage in formation of a duplex structure is usually the formation of randomly dispersed nuclei. In this case, the transformation, dispersion → duplex, takes place during isothermal annealing. Other examples for the occurrence of microstructural transformations in alloys are bulk concentration gradients as for example for decarburization or carburization of steels. Concentration gradients may cause microstructural gradients.

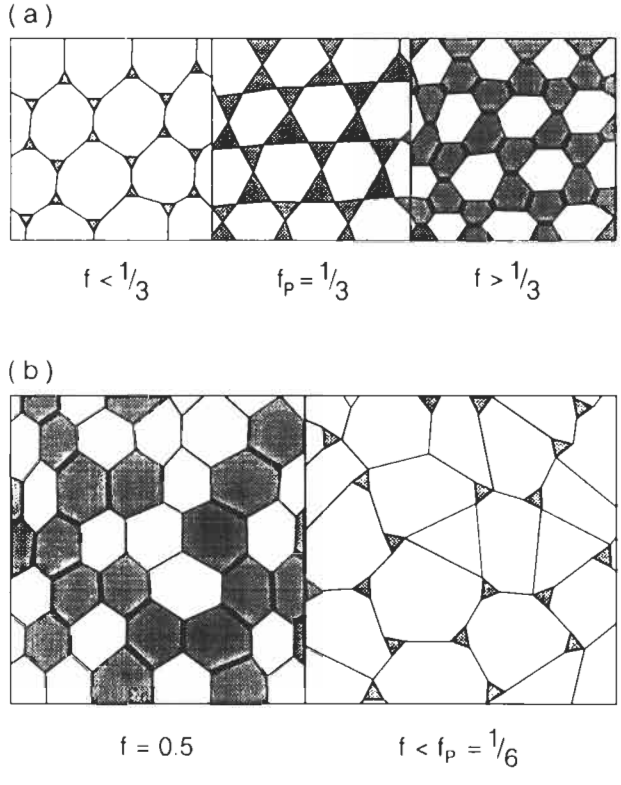

Fig. 14. Transformations of types of microstructure in planar sections (schematic). (a) Dispersion ⇋ net. (b) Duplex ⇋ dispersion. (From HORNBOGEN [1984].)

References: p. 935.

4. *Development of microstructure*

4.1. Basic aspects

The microstructure of a crystalline material may result from structural phase transformations and/or interaction processes between structural defects. In fact, a general and reciprocal relationship exists between microstructures and defect interactions. Any microstructure may be interpreted as the result of the interaction between structural defects and/or phase transformations. On the other hand, it should be possible to synthesize new microstructures (and, hence, materials with new properties) by utilizing this relationship, e.g., by means of more complex defect interactions (possibly combined with phase transformations). The thermomechanical treatment of materials represents an example of this kind. Microstructures generated by structural phase transformations are discussed in chs. 8, 15, 16, and 17. Microstructures resulting from the interaction between some specific types of lattice defects are treated in chs. 21–25 and 27. In this chapter, attention will be focused on those microstructures that are not the result of phase transformations. Despite the complexity of all conceivable processes for the development of microstructures, a guideline for a systematic understanding of the genesis of microstructures may be provided by considering some relatively simple and well studied types of interaction processes involving only one or two types of structural defects. This "model approach" will be used here.

4.2. Microstructural changes stimulated by interfacial-energy reduction

Three classes of microstructural changes driven by interfacial energy may be distinguished:

1. Microstructural changes in single-phase materials (without applied potential fields).
2. Microstructural changes in polyphase materials (without applied potential field) when the materials have: (a) a dispersion-type structure; (b) a duplex (or a network) structure.
3. Microstructural changes due to the effects of applied potential fields (e.g., temperature or electric field gradients).

An excellent review of these classes is the one by MARTIN and DOHERTY [1976].

4.2.1. Microstructural changes in single-phase materials, stimulated by interfacial energy: domain and grain growth

Internal interfaces in solids — such as grain boundaries or domain boundaries in ordered systems (atomic order, spin order, polarization order, etc.) — are associated with a positive excess energy resulting in grain or domain growth. Local atomic arrangements at or near moving interfaces can differ significantly from arrangements at or near stationary interfaces, giving rise, for example, to drag effects (solute or defect drag), structural changes of the interfaces due to defect production, etc. A complete theory of interfacial motion would have to account not only for these effects, but also for the topological changes of the array of interconnected interfaces during domain and grain

growth. For far no such theory is at hand. However, models treating various aspects of the problem separately have been put forward. The problems of the growth of grains or magnetic domains are treated in chs. 28 and 29, respectively. As many growth theories make no distinction between grain and domain growth, we refer to ch. 28 for all theories that apply to both processes.

Two approaches to describe the motion of a domain wall have been proposed. The earlier, widely used phenomenological approach states that the wall mobility is proportional to the thermodynamic driving force, the proportionality constant being a nositive quantity called the mobility. The driving force in this approach is the product of the mean of the local principal curvatures of the interface and the excess free energy per unit area (σ). This approach leads to a growth law of the type $\langle D \rangle^2 \alpha \sigma t$, where <D> is the average diameter of the domains in a polydomain structure and t is the time. This result has been experimentally confirmed for several ordered alloys (e.g., ARDELL *et al.* [1979] and ROGERS *et al.* 1975]) and can account for the broad distribution of domain sizes frequently observed experimentally.

The approach of ALLEN and CAHN [1979] models the motion of an interface by solving a diffusion equation that has been modified to account for the thermodynamics of non-uniform systems (LANGER and SEKERKA [1975]). Domain walls have a width in which there are compositional and order-parameter variations, i.e., a crystal containing a domain wall is a non-uniform system. The order-parameter variation is the basis of a diffusion potential whose gradient results in an atomic flux. This description leads to a time-independent Ginsburg–Landau equation for changes in the order parameter and hence for the wall motion. In the limit of large radii (r) of wall curvature, the propagation velocity (V) of the wall is found to be proportional to r, but independent of the excess energy (σ) of the wall. This does not imply that the energy dissipation during domain growth is independent of σ. In fact, the energy dissipation may be shown to be proportional to σ.

Experimental tests were carried out in which σ was varied by two orders of magnitude. Domain-coarsening kinetics and σ were found to scale differently with temperature as had been predicted theoretically. On the basis of the results discussed so far, we are led to conclude that cases exist where V is proportional to σ, and there are clearly other cases where V is independent or even nonlinearly dependent on σ (e.g., TURNBULL [1951] and LI [1969]). No general criterion seems apparent at present for relating V to σ and boundary curvature for different experimental conditions.

The development of our understanding of continuous ("normal") grain growth started when it was recognized that the driving force for grain growth is the decrease of grain boundary energy (SMITH [1952]). On the basis of this approach several simple and mostly qualitative interpretations of grain growth were given. The first quantitative model (BECK [1954]) predicted an increase of the average grain diameter with time as $t^{1/2}$ which, however, was rarely confirmed experimentally. Mostly, time exponents less than 0.5 were observed and attributed to the drag forces caused by inclusions or solute atoms. More insight into the processes involved in grain growth was obtained when more sophisticated theoretical approaches were used. HILLERT [1965] applied the statistical treatment of Ostwald ripening of precipitates to grain growth. Some of the foundations

References: p. 935.

of Hillert's analysis were reexamined by LOUAT [1974] who pointed out that in grain growth, as opposed to Ostwald ripening, "grain collisions" occur in which faces are gained and/or lost. In order to allow for these events, grain growth was considered as a particular case of random walk.

HUNDERI and RYUM [1979], [1981] applied a deterministic model considering individual boundaries and described the change of size of the individual grains by an extremely large set of differential equations (one for each grain), which they solved numericany. Very recently, ANDERSON *et al.* [1984] used the Monte Carlo method to simulate grain growth and included in this treatment also the case of Zener drag. Finally, ABBRUZZESE [1985] further developed the Hillert model by calculating the critical radius. He used discrete grain size classes which led to a reasonably small set of differential equations (only one for each class) and thus to the possibility to calculate numerically the evolution of the grain size distribution. This approach was extended further by including textural effects (ABBRUZZESE and LÜCKE [1986]) in the form of orientation-dependent grain-boundary energies and mobilities. The most important result of this extension was that, instead of the single critical radius found in the textureless case, now for each orientation a different critical radius is obtained but with a value depending on all orientations. It is shown that (very generally) grain growth leads to pronounced texture changes which are accompanied by characteristic changes of the scattering of the grain size distribution and by peculiarities of the grain growth kinetics, which then does not even approximately follow a $t^{1/2}$-law.

On the experimental side, the effect of particles has repeatedly been taken into account. The amount of work on the texture effects, however, is still small. For a long time, it was limited to measurements of the orientation of secondary grains. It was first shown for α-brass (BRICKENKAMP and LÜCKE [1983]) that also the apparently *continuous* grain growth leads to drastic texture changes and that these are connected with peculiarities in grain growth kinetics and grain size distribution. The authors were able to put forward some qualitative interpretations for these effects.

"Anomalous" grain growth (also termed secondary recrystallization) is characterized by an increase in size of a small fraction of the crystallites whereas the rest does not grow at all. Anomalous grain growth has been suggested to originate either from the fact that a few of the crystallites have higher grain-boundary energies and/or boundaries of higher mobilities than the majority of the grains.

In the experimental literature, anomalous grain growth was demonstrated to exist in pure polycrystals as well as multiphase alloys. MAY and TURNBULL [1958] demonstrated the significance of second phase particles for anomalous grain growth for the first time. In Fe–Si alloys, the occurance of anomalous grain growth was shown to depend on the presence of MnS particles which inhibited normal grain growth. In several high-purity materials (SIMPSON *et al.* [1971], ANTONIONE *et al.* [1980]) strain and texture inhibitation of normal grain growth was demonstrated. Texture inhibition is based on the following idea. If the grain structure is strongly textured, boundaries of low mobility result. The anomalous grains are assumed to have high mobility boundaries because their crystallographic orientations relative to their neighbouring grains deviate strongly from the texture. A firm link between texture and abnormal grain growth has been made by

HARASE *et al.* [1988]. In a $Fe_{50}Ni_{50}$ alloy they found that the largest grains after secondary recrystallization had a high frequency of coincidence boundaries such as $\Sigma 7$ or Σ 19b with the primary matrix grains.

4.2.2. Microstructural changes in polyphase materials with a dispersion structure, stimulated by interfacial energy: Ostwald ripening

If interfacial energy is the only driving force for an instability and if the rate of development of the instability is governed only by mass transport processes, the linear dimension, d, of any microstructural feature can be shown (HERRING [1950]) to scale with time by the expression:

$$d^n = d_0^n + \alpha G t \tag{1}$$

where d_0 is the value of d at time $t=0$, G is the parameter of the appropriate mass transport process and α is a dimensionless parameter which depends on the geometry. The scaling exponent, n, takes the values: $n=1$ for viscous flow, $n=2$ for interfacial control, $n=3$ for volume diffusion in all phases, $n=4$ for interfacial diffusion and $n=5$ for pipe diffusion. The growth laws discussed in the following paragraphs for specific processes extend eq. (1) by giving explicit expressions for α and G. Normally, microstructural changes in multiphase alloys involve changes of shape, size and/or position simultaneously. For convenience, these three aspects are discussed separately.

An array of inclusions or dislocation loops or pores of equilibrium shape, but different sizes, interact because the concentration of solute atoms (or the concentration of vacancies, or the vapor pressure in a gaseous system) in the vicinity of small (large) particles is higher (lower) than the average supersaturation. The solute, therefore, flows from the smaller to the larger particles. Hence, smaller particles shrink and larger particles grow by "devouring" the smaller ones, a process known as *Ostwald ripening*. For reviews of various aspects of the problem, we refer to the articles by JAIN and HUGHES [1978], KAHLWEIT [1975] and HENDERSON *et al.* [1978]. The phenomenon of Ostwald ripening was analyzed first for the solid state by GREENWOOD [1956], and then independently and simultaneously by WAGNER [1961] and by LIFSHITZ and SLYOZOV [1961], assuming the common case of spherical precipitates growing by volume diffusion. Analogous expressions have been developed for other types of coarsening. The corresponding constants (α, G, n) of eq. (1) are summarized in table 1. In the case of coarsening of spheres by volume diffusion, which is the most commonly observed case ($r^3 \propto t$), a steady-state distribution of sizes is predicted to be approached irrespective of the initial size distribution, with a maximum particle size of $1.5r$, where r is the mean particle radius (figs. 15a, b). (See also ch. 15, § 2.4.2)

A critical assumption in the Lifshitz–Slyozov–Wagner (LSW) theory is that the diffusion fields around each particle are spherically symmetrical. This is strictly valid for zero volume fraction of precipitates when the concentration gradients around adjacent particles do not interfere. If the LSW theory is extended (ARDELL [1972]) to account for finite volume fractions, the basic form of eq. (1) is retained but the proportionality constant α is increased and the particle size distribution is broadened. The LSW analysis cannot persist to very large times, because ultimately the system should ripen into one

large particle. In fact, it was shown (KAHLWEIT [1975]) that the coarsening rate of the largest particles initially increases rather rapidly, then passes through a maximum and slowly approaches zero for long periods of time. The value of the coarsening rate predicted by the LSW theory is reached shortly before reaching the maximum rate. The significance of coherency strains for Ostwald ripening effects will be discussed in the next sub-section on stability against coarsening. In the LSW treatment, solute transport is assumed to be the rate-controlling process. Hence, modifications are required if other processes play a role, for example, ternary additions, solvent transport effects or dissociation of solute and/or solvent molecules. The latter case has been discussed by WAGNER [1961]. The effect of solvent transport may be accounted for (ORIANI [1964]) by modifying the diffusion parameter D in the LSW equations, leaving the main result (growth law, size distribution) unaltered. The modification of D becomes important, however, if we use growth-law observations to derive σ, D, etc. The same applies to the effect of ternary additions on the ripening rate. Ternary additions alter the rate constants of coarsening by a factor $1/3(1-K)^{-2}c_0^{-1}$, leaving the scaling law unchanged (BJORKLUND *et al.* [1972]). c_0, is the ternary alloy content and K is the distribution coefficient. Ostwald ripening of semi-coherent plate-shaped precipitates (Widmanstätten plates) represents yet another case for which the LSW treatment cannot be applied without modifications. Ostwald ripening of Widmanstätten plates results in large aspect ratios, as the lengthening of these plates is diffusion-limited whereas the thickening is mobility-controlled by the good-fit (semi-coherent) interface (AARONSON *et al.* [1970] and FERRANTE and DOHERTY [1979]).

The experimental confirmations of the theoretical predictions on Ostwald ripening are still fragmentary (for a review see JAIN and HUGHES [1978]). Although numerous experiments confirming the scaling laws given in table 1 have been reported (for a review of the earlier data we refer to MARTIN and DOHERTY [1976]), the relatively small range of particle sizes that can be obtained experimentally is not sufficiently precise to allow unambiguous identification of the scaling exponent. In most cases, the observed

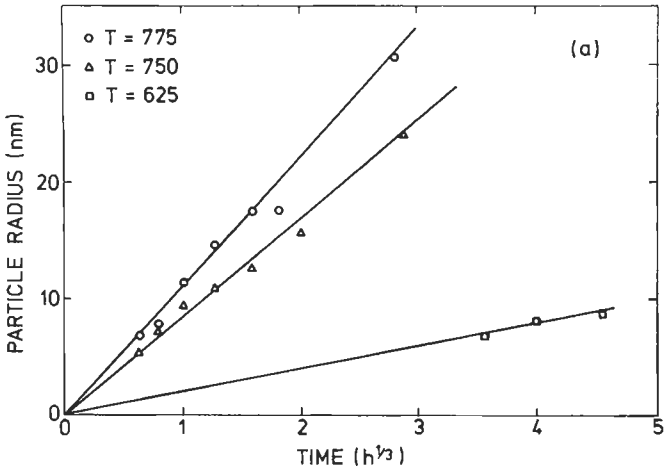

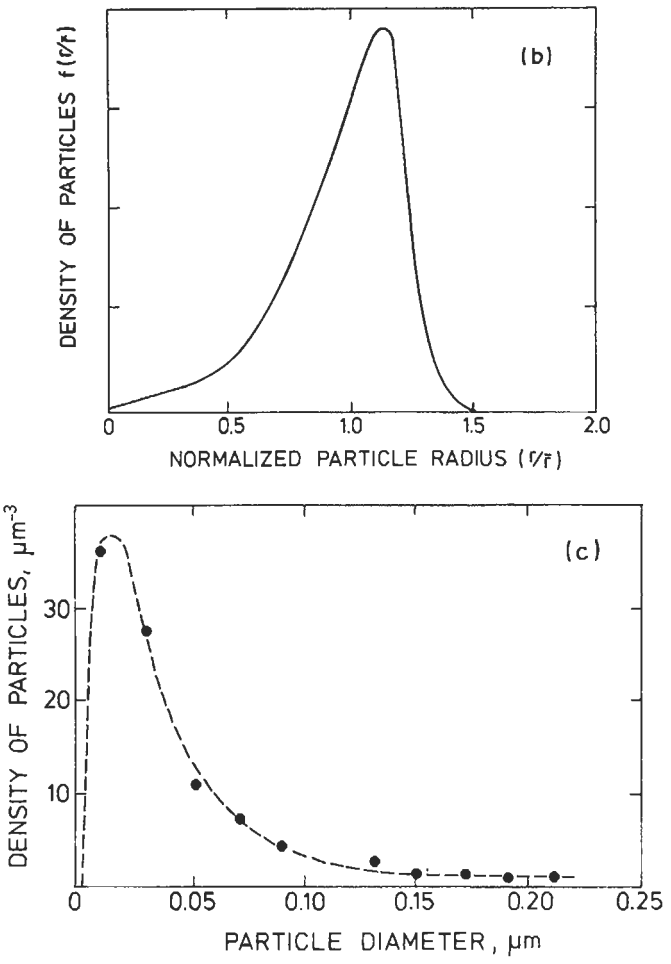

Fig. 15. (a) Plot of the particle radius against (time)$^{1/3}$ for a nickel–aluminium alloy annealed at three different temperatures (from ARDELL *et al.* [1966]). (b, c) Size distribution developed during Ostwald ripening: (b) theoretical prediction according to the Lifshitz–Slyozov–Wagner theory; (c) experimental observation on silica particles in copper annealed at 1173 K for 27 h. (From BHATTACHARYA and RUSSELL [1976].)

size distributions are wider than those predicted by the theory (figs. 15b and 15c). Frequently, also a few large particles are found which are not a part of the main system of particles. Furthermore, a tail on the large-size side of the size distribution is observed, in contradiction to the LSW theory (see also ch. 15, § 2.4.1).

The available experimental evidence on the effect of volume fraction on coarsening is conflicting. Studies on Cu–Co alloys showed clear dependence on volume fraction, whereas other work (Ni_3Al in Ni, NbC in Fe, Cu in α-Fe) failed to detect any effect. Recent experimental work has evidenced the possibility of contact between growing

References: p. 935.

Table 1
Ostwald ripening rates.

Rate-controlling process	Shape of particles	Expressions for constants[a]			Reference
		n	α	G	
Volume diffusion	Spheres	3	8/9	$D\sigma_b C_\alpha V_m/RT$	WAGNER [1961] LIFSHITZ and SLYOZOV [1961]
	Plates	3	$3A'(1+A'/A'_{eq})$	$Df\sigma_b V_m/2pRT$	DOHERTY [1982]
Grain-boundary diffusion	Spheres	4	9/32	$D_b\sigma C_\alpha V_m\delta/ABRT$	ARDELL [1972] KIRCHNER [1971]
Dislocation-pipe diffusion	Spheres	5	$(1.03)^5(3/4)^4 5/6\pi$	$D_d\sigma_b C_\alpha V_m qN\eta/RT$	ARDELL [1972]
Interface-limited growth		2	64/81	$\sigma_b\beta C_\alpha V_m/RT$	DOHERTY [1982]

[a] The symbols used are given below with their meaning or an expression.

A parameter, $A=2/3-\sigma_b/\sigma+(\sigma_b/\sigma)^2/24$.
B parameter, $B=\frac{1}{2}\ln 1/f$.
A', A'_{eq} average and equilibrium aspect ratios of precipitate, respectively.
C_α, C_β precipitate and matrix concentrations, respectively.
D, D_b, D_d general, boundary, and dislocation-pipe diffusion constants, respectively.
f function given by $f=C(1-C_\alpha)/(C_\beta-C_\alpha)^2$.
N number of dislocations intersecting one particle.
p parameter tending to π for large precipitates.
q diffusional cross-section of a dislocation.
R gas constant.
T temperature.
V_m molar volume.
β proportionality constant including the interface mobility.
δ boundary thickness.
η geometrical parameter.
$\sigma(\sigma_b)$ energy of grain boundary or interphase boundary.

precipitates. The theoretical discussion of this effect is based on independent growth of adjacent precipitates, the center-to-center distance between the particles remaining fixed (DAVIS *et al.* [1980a]). It is, however, difficult to see how the solute atoms are led into the narrowing gap between adjacent particles. An alternative hypothesis is that the particles will actually attract each other and move together in order to reduce the elastic strain energy. As similar effects have been seen in alloys with small lattice misfit (Ni–Cr–Al), this hypothesis seems not to provide a convincing explanation. In a number of alloys (e.g., carbides in steels, UAl_2 in α-U, θ in Al–Cu alloys) evidence has been presented suggesting substructure-enhanced diffusion, i.e., power laws during coarsening ($r^n \propto t$) where n is greater than 3. In none of these studies were attempts made to fit the results to one of the theoretically predicted relationships $r^n \propto t$ and no work seems to have been published which attempted to check if the details of the substructure-enhanced diffusion theories are correct. The general conclusion, though, is that the theories described seem successful in accounting qualitatively for the effect of lattice defects on coarsening.

4.2.2.1. Stability against coarsening. The general condition for Ostwald ripening to proceed is a decrease of the free energy. In the case of precipitates surrounded by an elastic strain field, the total energy (E) of an array of precipitates consists of the volume energy, the interfacial energy of the precipitates and the elastic energy of the strain fields. If the precipitate volume is constant, E depends only on the elastic energy and the interfacial energy. In the special case of two precipitates in a solid (volumes V_1 and V_2), the interfacial energy (S) and elastic energy (T) scale as $(V_1^{2/3} + V_2^{2/3})$ and $(V_1 + V_2) + V_1 V_2 f/a^3$, respectively, where a is the separation of the two precipitates and f is a function that is unity for distant precipitates. If $T \gg S$, the total energy (for $V_1 + V_2 = \text{const.}$) has a minimum if $V_1 = V_2$. In other words, the strain energy stabilizes the two particles of the same size against coarsening into one large particle. Basically, the same arguments hold for infinite arrays of particles as was apparently first recognized by KHATCHATURYAN and SHATALOV [1969]. The general conditions for stability of precipitate arrays against coarsening were recently worked out by PERKOVIC *et al.* [1979], LARCHE and CAHN [1973], [1978] and JOHNSON and ALEXANDER [1986]. Stability was found to be promoted by low interfacial energies, large elastic misfits and large volume fractions of precipitates. The phenomenon of elastic stabilization may be significant for the design of high-temperature alloys. In fact, the growth rates observed experimentally for θ' precipitates in Al–Cu alloys (BOYD and NICHOLSON [1971]) seem to support this view. AUBAUER [1972] has attempted to account for certain fine dispersions being stable against coarsening in terms of the diffuseness of the interface between a precipitate and the surrounding matrix, as described by CAHN and HILLIARD [1958]. If one assumes that the diffuse rim surrounding a precipitate is independent of precipitate size, it can readily be seen that the fraction of material that is in the precipitate and not in the rim will increase as the size increases. The bulk of the precipitate has a different structure and therefore a different atomic volume from the matrix while in the interface rim zone it is assumed that the structure changes steadily towards that of the matrix. Consequently, the precipitate and the rim zone are associated with an elastic distortion. The energy associated with this distortion increases as the particle grows, whereas the energy associated with the diffuse interfaces decreases as the total surface area is reduced during coarsening. If the surface energy is sufficiently small and if there is a finite rim thickness and appreciable strain energy, a minimum exists in the total energy, stabilizing the corresponding particle size. This conclusion was questioned because of the treatment of the strain energy used (DE FONTAINE [1973]) and because the precipitates, even if stabilized against growth, should be unstable against a change in shape, for example towards a disk (MORRALL and LOUAT [1974]). On the other hand, the Aubauer model seems to account successfully for several reported cases (GAUDIG and WARLIMONT [1969], WARLIMONT and THOMAS [1970]) where very fine dispersions of coherent ordered particles were seen to resist coarsening. The stability against coarsening ot two misfitting particles subjected to an applied tensile stress was examined by JOHNSON [1984] using a bifurcation approach. The stability of precipitates subjected to an applied stress may be enhanced or diminished depending on the relative orientation of the precipitates and the magnitude of the applied stress. The results obtained for cube-shaped particles are qualitatively different from those for spheres at short distances of separation.

References: p. 935.

The effects of the applied stress are manifested only in elastically inhomogeneous systems and are sensitive to the precipitate morphology. The theory predicts that precipitates may be stable up to a level of applied stress (threshold stress) sufficient to induce morphology changes.

4.2.2.2. Technological applications of coarsening theory. In all types of coarsening, the rate of the process is proportional to the interfacial energy (σ) driving the process and the solubility C_α of the solute atoms. Furthermore for all situations, except the relatively rare interface-controlled one, the coarsening rate also scales with the diffusion coefficient (D). Hence, alloys for high-temperature application, where low coarsening rates are desirable, may be obtained if σ, C_α or D are small. This expectation is borne out by various classes of high-temperature materials.

Nickel-based superalloys containin coherent ordered γ' precipitates (Ni_3Al structure) in a disordered γ-matrix (Ni–Al solid solution) have exceptionally *low interfacial energies* of the order of 10^{-2} J/m^2. In other words, the driving force for the coarsening of the γ' precipitates during creep is minimized. Alloys of this type retain their mircrostructure during creep. If the microstructure of such an alloy is tuned to a maximum creep lifetime, the microstructure changes little during creep loading. This is not so if the lattice misfit between γ and γ' is significant. The lattice misfit enhances the driving force for γ' coarsening, which changes the microstructure of the alloy in the coarse of a creep experiment. Hence, the microstructure tuned to maximimum creep life disappears during creep, and reduces the lifetime relative to an alloy with zero misfit. This difference is borne out by the observations. In fact, owing to the different solubilities of most elements in the γ and γ' phases, the γ/γ' misfit can be tailored to zero by the addition of solute elements to equalize the lattice constants of the two phases (e.g., Cr).

Low solubility can easily be achieved by using precipitate phases with high energies of formation and with a type of chemical bonding that differs from the surrounding matrix. The best-known examples are low-solubility oxide-dispersed phases, e.g., Al_2O_3 in Al. Except for very special cases, such phases cannot be precipitated from a supersaturated solid solution. Therefore, other techniques, such as powder metallurgy, internal oxidation or implantation are commonly applied. If the atomic radius of the solute atoms differs strongly from the atomic size of the matrix material, the two metals normally show negligible solubility in the solid state. Alloys of this type (e.g., W–Na, Al–Fe) have also been used to obtain coarsening-resisting materials.

Low diffusion coefficients have been applied in several ferrous alloys to resist coarsening. For example, the addition of a third component which segregates preferentially to the carbide phase (e.g., Cr, Mo, W) can slow down the coarsening of carbides considerably as it requires diffusion of both carbon and the third element and the latter, being substitutional, diffuses much more slowly than the carbon.

4.2.3. Microstructural changes in polyphase materials with a duplex structure, stimulated by interfacial energy

A *duplex structure* (SMITH [1954]) is an oriented crystallographic unit consisting of two phases with a definite orientation relationship to each other. Technologically and scientifically, the most important group of duplex structures are rod- or plate-shaped

duplex structures, such as directionally solidified eutectics (for a review, see LIVINGSTON [1971]). As the growth of large lamellae at the expense of smaller ones is associated with a decrease in the surface-to-volume ratio, lamellar structures are expected to coarsen. In the absence of substructural effects this process is expected to occur by motion of lamellar terminations.

Two mechanisms have been put forward for this process. CLINE [1971] and GRAHAM and KRAFT [1966] proposed the curvature at the lamellar termination (fault) to be associated with a flux of atoms from the α phase to the β phase (fig. 16). The second mechanism of lamellar coarsening involves the diffusion of solute atoms from the finely spaced (λ_1) lamellae along a migrating boundary to the widely spaced (λ_2) lamellae on the other side of the interface (fig. 17). The theoretical analysis of the process (LIVINGSTON and CAHN [1974]) relates the boundary migration rate (V) to the spacing λ_2 of the widely spaced lamellae. The coarsening rate increases with increasing temperature and decreasing spacing of the lamellae as both effects reduce the diffusion times required. As short-circuit diffusion along grain boundaries becomes dominant at lower temperatures, coarsening by boundary migration is expected to become more prominent than coarsening by fault migration with decreasing temperatures as was observed experimentally. In comparison to coarsening by fault recession (fig. 16), coarsening by boundary migration becomes more important at finer spacings of the lamellae. Rod-shaped microstructures

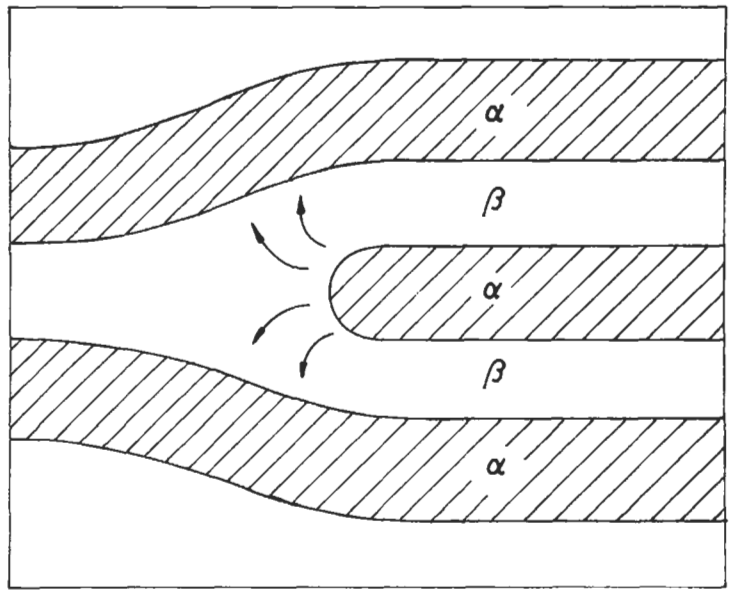

Fig. 16. Schematic of mass flux in the vicinity of a lamellar termination (fault). The curvature at the termination is proposed to induce mass flow of A atoms (from the α-phase) to the β matrix, leading to a recession of the termination with a corresponding increase in the thickness of the adjacent lamellae. (From CLINE [1971].)

References: p. 935.

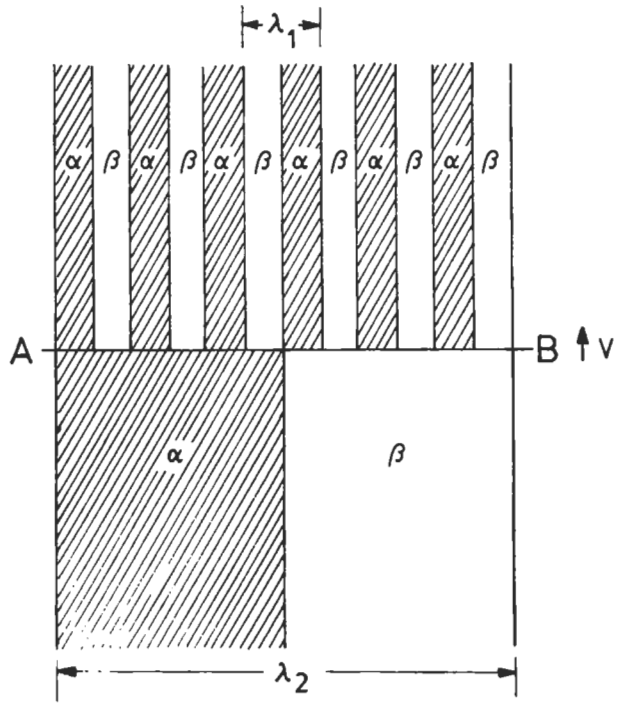

Fig. 17. Idealized model of discontinuous coarsening process. The grain boundary AB moves at a velocity V, consuming fine lamellae with spacing λ_1 and generating coarse lamellae with spacing λ_2. (From LIVINGSTON and CAHN [1974].)

are unstable with respect to shape and dimensional changes as they may decrease the surface-to-volume ratio by these processes. As was pointed out by CLINE [1971] and ARDELL [1972], the processes involved in dimensional changes are identical to Ostwald ripening (§ 4.2.2). In alloys produced by eutectic growth, the microstructure may be initially stabilized by the very uniform rod diameter. The time required for the steady state distribution of rod diameters to be built up during coarsening may be longer than for normal precipitate coarsening where a whole spectrum of particle sizes is present at the very beginning. In the present paragraph, attention will be focused on shape changes due to the coarsening of rod-shaped microstructures. The growth of a shape perturbation on a cylinder was already analyzed a century ago by RAYLEIGH [1878]. However, it is only relatively recently that quantitative models for the spheroidization of cylindrical precipitates have been put forward (CLINE [1971], HO and WEATHERLY [1975], NICHOLS [1976]). The theoretical treatments indicate (fig. 18) that a long fibre (length l) of radius d (with $l/d > 7.2$) is eventually replaced by a string of spheres (*Rayleigh instability*) where the sphere radii and spacing, λ, depend on the active kinetic processes. When the aspect ratio (l/d) is less than 7.2, shape relaxation to a single sphere is predicted. For infinite fibres, Rayleigh instabilities are predicted to dominate, whereas in the case of

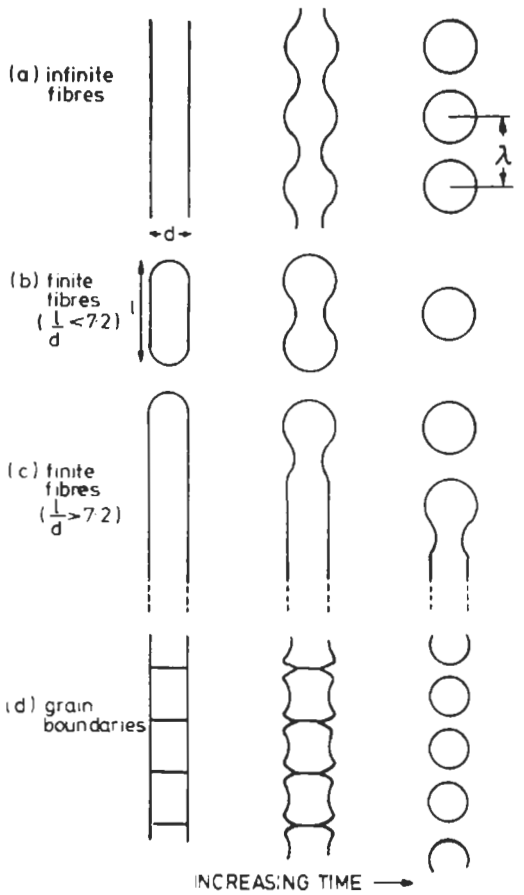

Fig. 18. Schematic representation of different modes of spheroidization of cylindrical inclusions. (From McLean [1978].)

fibres with finite length, drop detachment at the end of the fibres (fig. 18c) should be the faster process. Experimental observation for metallic (W–Na, Al–Pb, fig. 19) and nonmetallic systems ($NaNO_3$–H_2O, Ni–Al_2O_3) seem to support the view that progressive spheroidization from the ends of the fibres dominates. Yet another mechanism of spheroidization, which applies to both fibrous and lamellar inclusions, exists when grain boundaries in either phase intersect phase boundaries between the fibres and the matrix. At the points of intersection, grooves develop and progressively deepen with time to establish a local equilibrium configuration. Eventually, the grooves cause a division of one phase and result in spheroidization (fig. 18d). This process seems to be a serious limitation to many directionally solidified eutectic materials for high temperature operation. In addition to the instabilities mentioned so far, rod phases may also coarsen by *fault migration*. Faults are points of a rod at which additional rods form by branching

References: p. 935.

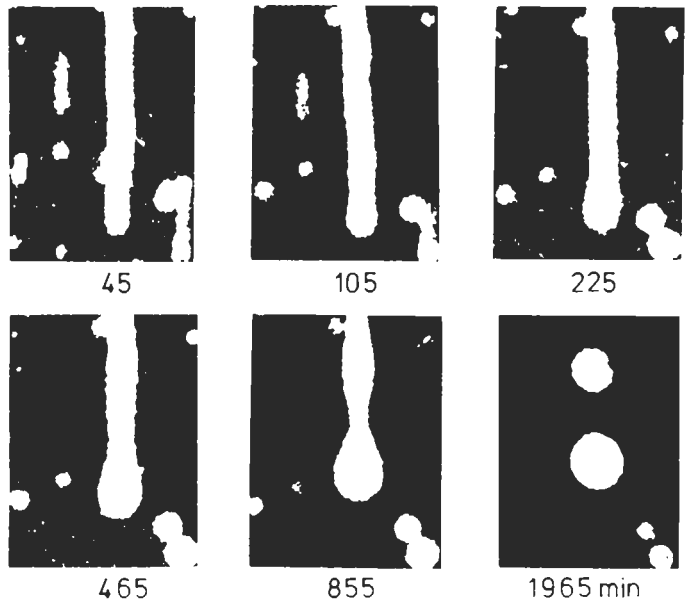

Fig. 19. Series of microradiographs showing the change in shape of Pb inclusions in Al as a function of annealing time at 620°C. (From McLean [1973].)

or at which a rod terminates. The termination of a rod is expected to shrink backward for the same reasons as apply to the shrinkage of a terminating lamella (cf. fig. 16). Because of the negative radius of curvature at the rod-matrix interface at a branching point, the branches are expected to fill in, i.e., to migrate in the growth direction, as was observed. Theories of the kinetics of fault migration have been presented by Cline [1971] and by Weatherly and Nakagawa [1971].

Instabilities were reported at the periphery of spherical cavities growing under stress along interfaces. If the stress was sufficiently large (Wingrove and Taplin [1969]), finger-shaped instabilities were seen to develop. The critical parameter for the development of these instabilities instead of spherical growth seems to be the ratio of the diffusion coefficients at the cavity surface and a boundary supplying the vacancies (Beeré [1978]). Instabilities cannot develop if this ratio is large (typically > 100). For materials with slower surface diffusion, cavities above a critical size become unstable. The critical size depends on the applied stress and the cavity spacing.

4.2.4. Coarsening by Brownian motion

The spontaneous random motion of gas-filled cavities, leading to a coarsening process by cavity coalescence when two cavities meet, has been deduced both by direct observation, and indirectly. The first observations were apparently made on UO_2 plates irradiated with neutrons to produce fission fraqments (krypton, xenon) which precipitated in the form of gas-filled cavities (Gulden [1969]). These cavities were seen in the

electron microscope to show Brownian motion, the rate of which was controlled by volume diffusion in the host crystal for cavities above 3.7 nm diameter. Similar observations were made for helium-filled cavities in gold and copper, krypton in platinum and xenon in aluminum (cf. GEGUZIN and KRIVOGLAZ [1973]) and helium bubbles in vanadium (TYLER and GOODHEW [1980]).

4.2.5. Microstructural changes stimulated by interfacial energy in the presence of external potential fields

The presence of a field of varying potential (e.g., due to a stress- or a temperature gradient, or due to electric or gravitational fields) modifies the driving forces for diffusion and, thus, may result in microstructural changes.

4.2.5.1. Temperature gradients. The theory of diffusional migration was first developed for volume diffusion in a temperature gradient. In the subsequent decade this work was extended by several authors to surface-diffusion controlled processes and other fields, such as electric, magnetic, stress or gravitational field gradients. For a review of this development, we refer to the book by GEGUZIN and KRIVOGLAZ [1973].

The dominant physical reason for an inclusion to migrate in a temperature gradient is the temperature-dependence of the solubility. For example, let us consider a liquid inclusion in a solid. We assume that at the "front" side of the inclusion (where the temperature is highest), the liquid in contact with the solid has a lower solute content than at the (colder) "rear" surface. The different solute content results in a concentration gradient and, hence, in a flux of solute atoms from the rear to the "front" surface, which causes the "front" surface to melt or dissolve and the "rear" surface to freeze or migrate by crystal growth from solution. In addition to the atom flux resulting from this process, causing the inclusion to migrate up the temperature gradient, there is also a drag exerted on the atoms by a directional flux of phonons (phonon wind) which results from the temperature gradient. Similarly, in metals with aspherical Fermi surfaces, the diffusing atoms are dragged by an electron wind which appears under these circumstances in a temperature gradient. In the simplest case of a spherical inclusion in a temperature gradient, the velocity (v) of the inclusion of size R is found to depend linearly on the temperature gradient (grad T). The velocity v is proportional to (grad T)$\cdot R^n$, with $n=0$, 1, -1 if the rate-controlling process is diffusion through the matrix, the particle-matrix boundary or the particle, respectively. As all parts of the inclusion move with the same velocity, there is no shape change during migration.

All of these results assume the matrix-particle interface to act as ideal sink and source for vacancies. If this is not so, the velocity is smaller or the inclusion is not mobile at all. The first experimental investigations on the motion of inclusions in a temperature gradient were apparently carried on the motion of aqueous solution droplets in sodium nitrate (LEMMLEIN [1952]), although the motion of brine inclusions in a temperature gradient was already invoked by WHITMAN [1926] to explain the fact that polar ice becomes purer at its cold upper surface. The motion of gaseous and liquid droplets in a solid in a temperature gradient has been studied in a variety of metallic and nonmetallic systems (e.g., He in Cu, Kr in UO_2, W in Cu, water in $NaNO_2$, water in KCL, water in NaCl, Li in LiF, NH_4Cl bubbles in NH_4Cl, gas-filled bubbles in KBr, NaCl, KCl, Pb in

References: p. 935.

Al; for a review we refer to the book by GEGUZIN and KRIVOGLAZ [1973]). The observed migration velocities as well as the correlation between the velocity and the inclusion size was in all cases well accounted for by the theoretical prediction.

Above a certain temperature gradient, the migrating droplets (e.g., voids or gas bubbles in nuclear fuel elements, metal droplets in semiconductors or water droplets in ionic crystals) start to break down by the growth of protrusions from the rear corner, releasing a thin trailing liquid veil. The physical reason for the breakdown is the difference between the thermal gradient at the edges and in the center of the droplets, resulting in different migration rates of the two regions. An additional factor comes in when the inclusion contains two phases, such as liquid and vapor. The additional factor is the change of the interfacial free energy with temperature, and it may cause the inclusion to migrate down the temperature gradient (ANTHONY and CLINE [1973]). Consider a spherical gas-filled inclusion in potassium chloride subjected to a temperature gradient. The wall of this gas-filled inclusion is assumed to be covered by a liquid film or brine. In addition to the normal diffusive flux from the hot to the cold surface, there is a flow of liquid in the liquid film caused by the fall in the liquid-vapor interfacial energy as the temperature falls. The interfacial-energy-induced flow in the liquid film is the essential step in the movement of the inclusion, as it carries potassium chloride that will be deposited at the hot side of the inclusion so that the inclusion moves to the cold end of the crystal. An analysis based on this model successfully predicted the observed velocities of two-phase inclusions in potassium chloride.

Probably the technologically most important observations are those of thermal migration of nuclear fuels through protective coatings in the temperature gradients associated with nuclear reactors (MCLEAN [1982]). In recent years, thermal migration effects led to some concern over the microstructural stability of high-temperature alloys; in particular, in-situ composite materials, exposed to high-temperature gradients, in turbine blades. Investigations on the thermal stability of eutectic composites (Ni-, Al-, Pb-base alloys) provide evidence for thermal instabilities under the conditions used in modern aircraft engines (HOUGHTON and JONES [1978]). The other problem of considerable practical relevance is the effect of temperature gradients on Ostwald ripening. The available evidence is controversial, indicating — often for the same system — that thermal gradients may increase, not affect or decrease the rate of Ostwald ripening (e.g., DAVIS *et al.* [1980b], and JONES and MAY [1975]). This controversy may be due to different rate-controlling processes in the various experiments. Ostwald ripening is enhanced if adjacent migrating particles collide and join up (JONES and MAY [1975]) or because the back and front of an inclusion migrate with different velocities owing to the different temperatures at those sites (MCLEAN [1978]). However, temperature gradients can also decrease Ostwald ripening owing to the generation of a shape instability, as was discussed previously (veil formation). (See als 'thermomigration', ch. 7, § 6).

4.2.5.2. Temperature cycling. This may affect the microstructure of alloys by three effects (MCLEAN [1982]):

(i) a variation of the solubility of the phases;
(ii) a differential thermal expansion leading to local strain gradients;
(iii) capillary terms arising from the Gibbs–Thompson effect.

In most alloys, the first effect seems to dominate and may result in accelerated Ostwald ripening or morphological changes, as was observed in composites that were remarkably stable under isothermal conditions (COOPER and BILLINGHAM [1980]).

4.2.5.3. Magnetic fields. The energy of a magnetic phase is altered by the presence of a magnetic field, and hence the microstructure of alloys that are magnetic will be changed by the application of a magnetic field. This subject has been extensively reviewed by CULLITY [1972]. Magnetic fields may affect both the atomic order in stable solid solutions and the precipitation from supersaturated solid solutions. In stable solid solutions, magnetic fields generate *directional order* by altering the proportion of like pairs that are aligned in the field direction. Such an alignment causes no change from the random situation in terms of the total fractions of like and unlike nearest-neighbor pairs.

During precipitation from solid solutions, magnetic fields favor the formation of those precipitates that are aligned with respect to the external field. The best known example is the preferred formation of magnetic rods aligned parallel to the magnetic field in Alnico alloys. A preferred orientation of precipitates may also be achieved during coarsening in the presence of a magnetic field. For example, if Fe_8N precipitates coarsened in a magnetic field, a complete orientation of the disc-shaped particles normal to the field direction was achieved (NEUHAUSER and PITSCH [1971]). Owing to the smaller demagnetization factor, the spins of the precipitates parallel to the magnetic field (H) become aligned so that a single-domain structure is formed. This domain structure increases the energy of the Fe_8N/Fe interphase boundary. Hence, precipitates oriented normal to H have the lowest free energy and, thus, grow at the expense of the other precipitates.

In materials of anisotropic magnetic susceptibility, external magnetic fields induce phase or grain-boundary migration. The first observation on this effect, was reported in the classical paper by MULLINS [1956] on boundary migration in diamagnetic bismuth. Magnetic annealing has recently been applied to ceramic superconductors (DE RANGO *et al.* [1991]). The objective was to align the crystallites in polycrystalline YBa_2Cu_3O8. Alignment of the crystallites (by other methods) has been shown previously to increase the maximum critical current density of these materials. In fact, magnetic annealing may prove to be applicable to all paramagnetic, diamagnetic or ferromagnetic materials provided the driving force due to the aligning field is large compared to the thermal fluctuation at the annealing temperature. Naturally, the same should apply to electrically polarizable materials (e.g., ferroelectrics) when annealed in an electric field.

4.2.5.4. Stress field. By analogy with magnetic fields, external stresses can modify the atomic order in stable solid solutions and the precipitate morphology in two-phase alloys. Directional atomic order has been induced in Fe–Al alloys by stress-annealing (BIRKENBEIL and CAHN [1962]).

In two-phase materials, external stresses may result in the alignment of precipitates and/or in shape changes. Several examples for the first effect have been reported: Fe_8N in FeN, Au in Fe–Mo–Au, θ and θ' in Al–Cu, $ZrH_{1.5}$ in Zr–H, Ti-hydride in Ti-H, γ' in Ni–Al alloys (MIGAZAKI *et al.* [1979]). Apparently, only a few observations of stress-induced shape changes have been published (MIGAZAKI *et al.* [1979], TIEN and COPLEY [1971]). Owing to the elastic anisotropy of the matrix and the precipitate, the free energy

References: p. 935.

of a precipitate depends on the precipitate orientation and shape. The theoretical treatment of both effects (GEGUZIN and KRIVOGLAZ [1973], SAUTHOFF [1976] and WERT [1976]) seem to be consistent with the experimental observations. Similar effects have been observed in alloys undergoing an order-disorder or a martensitic transformation. When a CuAu single crystal is ordered, it becomes subdivided into many domains, the tetragonal (c) axes of which are parallel to any of the three original cubic axes. In the bulk material and without an external stress field, the three possible cdirections are randomly distributed among the domains. The application of a compressive stress during ordering imposes a bias on the distribution of the c-axes such that the cube axis nearest to the compression axis becomes the preferred direction for the c-axes of ordered domains (HIRABAYASHI [1959] and ARUNACHALAM and CAHN [1970]).

The microstructure of materials undergoing martensitic transformations (cf. ch. 16) depends on external stress fields. The following two factors contributing to this effect are most important (DELAEY and WARLIMONT [1975]): (i) The orientation variant on whose macroscopic shear system the maximal resolved applied shear stress is acting will grow preferentially, (ii) near certain symmetric orientations, individual plates and self-accommodating groups will compete. Essentially, the same arguments apply to the microstructure of materials undergoing mechanical twinning. Effects of this type play an important role in shape-memory effects.

Gas bubbles situated at interfaces represent a special case of microstructural changes caused by stress fields. Owing to the compressibility of gas bubbles, the binding energy between a bubble and the interface depends on external stresses. Compression stresses lead to a decrease of the binding energy and, hence, may result in microstructural changes resulting from break-away effects of the boundaries from the bubbles (GREENWOOD *et al.* [1975]).

4.2.5.5. Electric fields. In bulk metals, strong electric fields may induce complex interactions between thermomigration and electromigration due to Joule heating (ch. 7). In thin films, efficient heat removal ensures reasonable isothermal conditions. Under these conditions, two effects resulting from the presence of electric fields were observed: (i) enhanced grain-boundary migration (LORMAND *et al.* [1974] and HAESSNER *et al.* [1974] and (ii) the growth of grain-boundary grooves which can eventually penetrate the film so that nucleation and growth of voids by grain-boundary diffusion occurs (HO and KIRKWOOD [1974]). The theoretical understanding of the processes involved is still poorly developed. In fact, the driving force exerted by a dc current on grain boundaries in gold was found to be several orders of magnitude larger than the theoretically estimated value (HAESSNER *et al.* [1974]). A similar result was also found from the motion of rod-shaped tungsten inclusions in Cu and from the displacement of deep scratches on the surface of Ag owing to the passage of a current along wire-shaped samples. (See also 'electromigration, ch. 7, § 6).

4.3. Deformation

All forms of plastic deformation may result in irnportant changes of the microstructure of materials with respect to the distribution and density of defects as well

as with regard to the morphology, volume fraction and sometimes also structure of second phases. They are discussed in chs. 19–26.

4.4. Multiphase microstructures generated by migrating lattice defects

4.4.1. Moving grain boundaries

If grain boundaries are forced (e.g., during recrystallization or grain growth) to sweep through a precipitate dispersion or a duplex structure, the following microstructures may result (DOHERTY [1982], HORNBOGEN and KÖSTER [1982]):

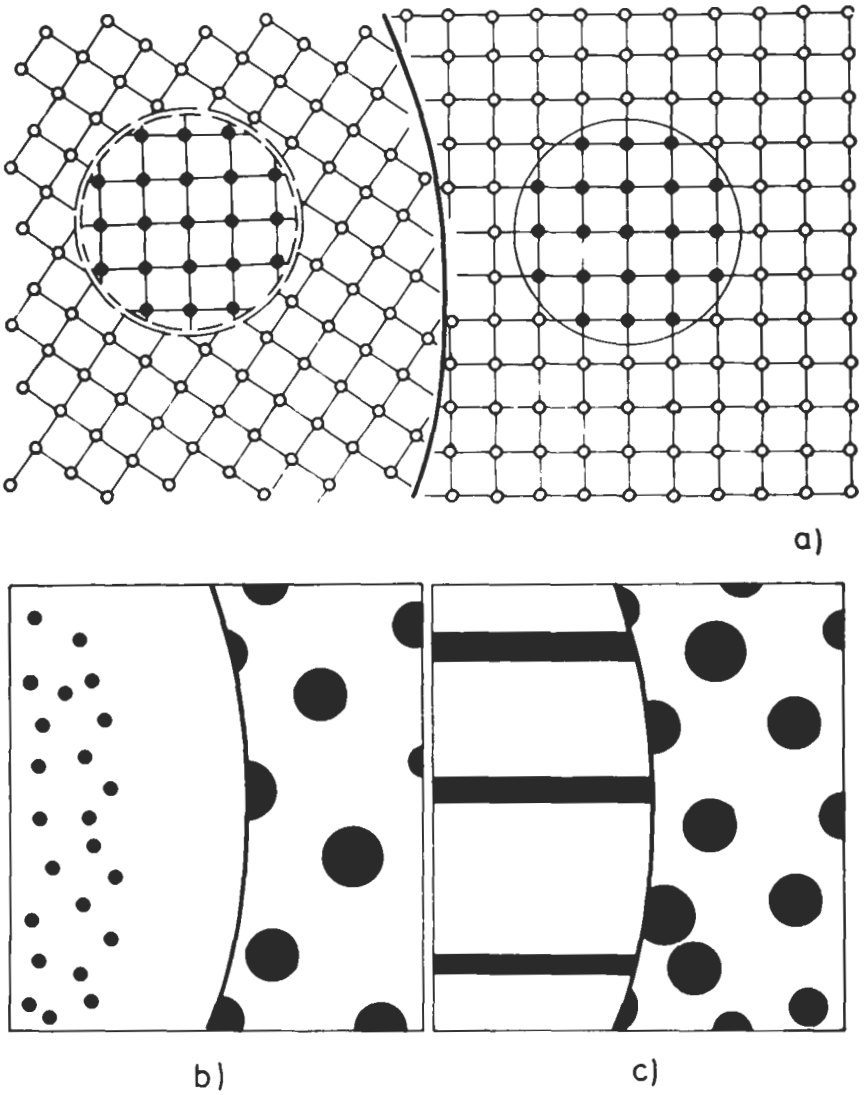

References: p. 935.

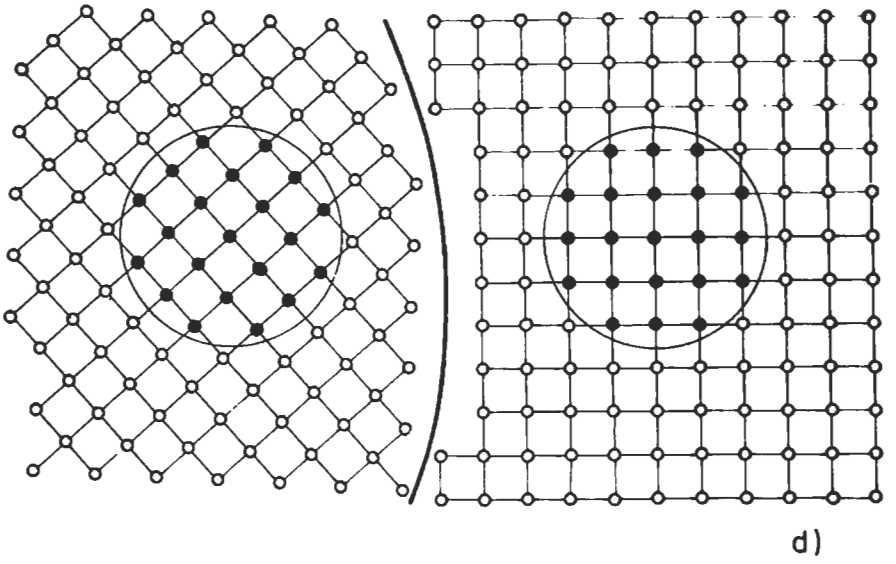

Fig. 20. Microstructural changes induced by a grain boundary migrating through a two-phase alloy containing dispersed precipitates: (a) transformation of coherent precipitates into incoherent ones as the boundary bypasses the precipitates; (b, c) dissolution of the precipitates, resulting a supersaturated solid solution, followed by continuous (b) and discontinuous (c) precipitation; (d) grain boundary passing through the precipitates without affecting the shape and size. The solid (open) circles in figs. 22a and 22d indicate solute (solvent) atoms.

(i) The boundary bypasses the precipitates which, therefore, retain their initial orientation and become incoherent (fig. 20a). Owing to the Gibbs–Thompson effect, the solubility of the precipitates rises so tfiat the smaller precipitates may dissolve, as was observed, for example, in the case of NbC in γ-Fe.

(ii) The coherent precipitates or the components of a duplex structure dissolve after contact with the moving grain boundary, so that a supersaturated solid solution is obtained. From this supersaturated solid solution, the solvent may reprecipitate either continuously (fig. 20b) or discontinuously (fig. 20c). Both cases have been observed experimentally. The dissolution as well as the precipitation processes seem to occur far more rapidly than anticipated, suggesting strongly enhanced diffusion in the migrating interfaces an in the lattice behind due to vacancy supersaturation (SMIDODA *et al.* [1978], GOTTSCHALK *et al.* [1980]).

(iii) The grain boundaries can pass through the coherent precipitates and, thereby, preserve the preexisting microstructure (fig. 20d). This precess seems rare as it requires the formation of new precipitates to match the rate of boundary migration.

(iv) The grain boundary is held by the coherent precipitates which then coarsen. This process occurs if the driving force for boundary migration is not sufficient to initiate one of the above processes.

(v) The moving grain boundary drags the precipitates (SMITH [1948]), as was reported for a variety of alloy systems containing gaseous particles as well as solid inclusions, for

example, for He in Cu, He in U, air in camphor, carbides in various metal transition alloys, GeO_2 in Cu, B_2O_3 in Cu, SiO_2 in Cu, Ag in W, Ag in Sn, Al_2O_3 in Ni, Al_2O_3 in Ag. The experimental results have been reviewed by GEGUZIN and KRIVOGLAZ [1973] and GLEITER and CHALMERS [1972]. *Particle drag* results from the directional movement of atoms from one ("front") side of the inclusion to the other ("rear") side. Hence, diffusional migration may occur by diffusion of atoms around or through the inclusion and diffusion of atoms along the particle-matrix interface. The kinetics of the particle drag may be controlled by the rate of one of these diffusion processes or by interfacial reaction at the boundary between the inclusion and the matrix. Examples of all cases mentioned have been reported and may be found in one of the reviews mentioned. Once particle drag starts, the boundary collects practically all particles in the volume which is swept. Particles collected in the boundary usually coarsen rapidly. Therefore, particle drag may result in the following changes of the properties of the boundary: (i) boundary brittleness and/or corrosivity due to a high density of undeformable particles, the electrochemical properties of which differ from the surrounding matrix; (ii) different mechanical and chemical properties in the particle-free zone and in the rest of the material. At high driving forces (e.g., during recrystallization) particle drag seems negligible as it is possible for the mobile boundary to migrate past the inclusions. (See also ch. 28, § 3.8).

4.4.2. Moving dislocations

The formation of colonies of precipitates in the vicinity of dislocations has been observed in a number of alloy systems, e.g., in iron, nickel, copper, aluminum and semiconductor materials.

In the initial model of this process (SILCOCK and TUNSTALL [1964]) and in the subsequent modification by NES [1974], a dislocation was proposed to climb so that precipitates can nucleate repeatedly in the moving stress field of the dislocation. During climb the dislocation emits vacancies. The incorporation of these emitted vacancies in the lattice of the precipitates is believed to reduce the precipitate-matrix mismatch energy if the precipitating phase has a larger atomic volume than the surrounding matrix. In the opposite case, a vacancy flux from the precipitate to the dislocation was also invoked (GUYOT and WINTENBERGER [1974]).

More recently, the experimentally observed coupling between dislocation climb and precipitate formation was re-interpreted by two other models. Dislocations were proposed to climb owing to the annihilation of quenched-in vacancies, while the precipitates form simultaneously by heterogeneous nucleation in the stress field of the moving dislocation. A study by transmission electron microscopy (WIRTH and GLEITER [1981a,b]) led to the conclusion that coherency strain relaxation by incorporation of vacancies in the precipitates may be only one of the processes involved. In fact, colony formation was found to occur (fig. 21a) by the climb of a prismatic dislocation loop which emits vacancies and, thus, generates a region of enhanced diffusivity. The excess solute atoms of this region of enhanced diffusivity migrate rapidly to the climbing dislocation and precipitate in the form of a chain of small particles (fig. 21b). Owing to their large surface-to-volume ratio, these fine particles rapidly coarsen by Ostwald ripening to form rows (colonies) of coarse precipitates behind the climbing dislocation loop. The spacing of the rows of coarse precipitates is

References: p. 935.

controlled by the balance between the interfacial energy and the diffusion path. Under steady-state conditions, such systems are known to approach a constant precipitate spacing. Hence, if the dislocation loop expands during growth, a constant precipitate spacing can only be maintained by increasing the number of precipitates as the loop radius increases. This condition results in a spoke-like precipitate arrangement, as was observed (fig. 21).

4.5. Periodic microstructures in open, dissipative systems ("self-organization")

Dissipative processes in open systems are frequently associated with pattern formation (NICOLIS and PRIGOGINE [1977], HAKEN [1978], MARTIN and KUBIN [1988]). The following microstructures seem to be the result of pattern formation in dissipative systems ("self-organization"):

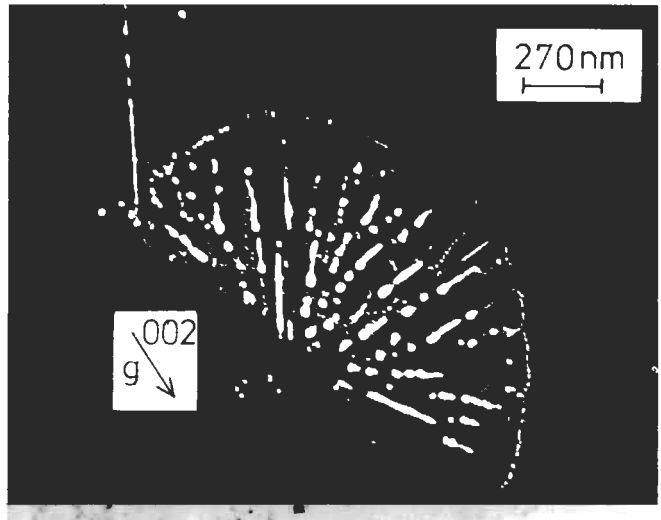

(a)

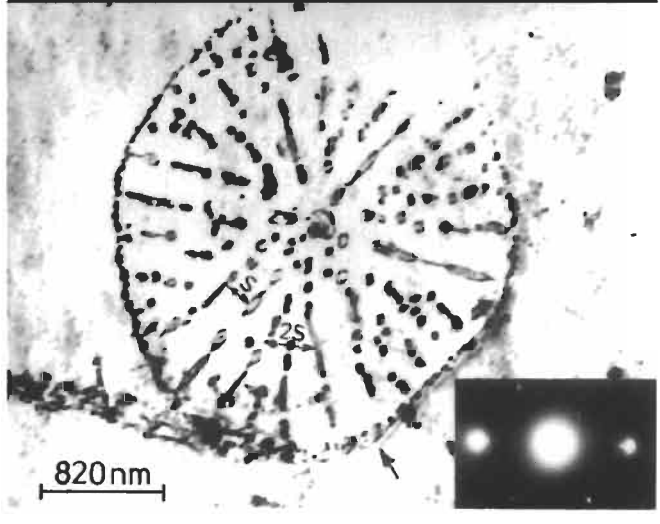

(b)

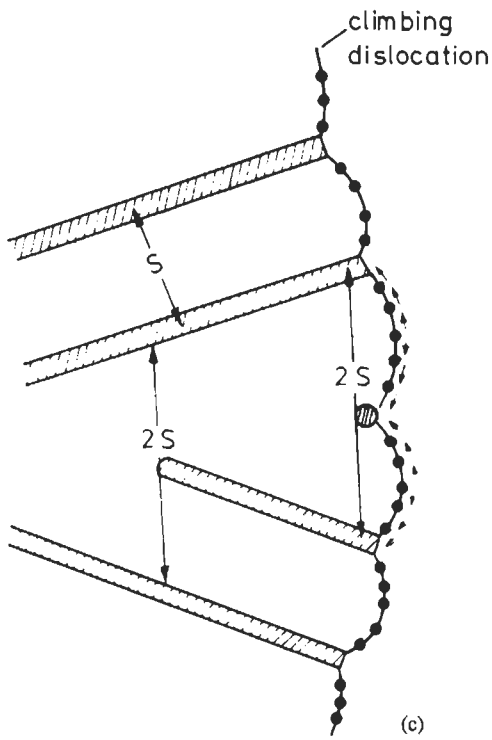

Fig. 21. (a) Bright-field and dark-field electron micrographs of colonies of silver precipitates in a Cu-5 wt% Ag alloy. The colonies formed behind the dislocation loops surrounding them. The loops expandes during colony growth. Two types of precipitates may be noticed. A chain of small precipitates along the dislocation loop, and large precipitates arranged radially in a spoke-like fashion. (b) Schematic model for colony formation by a two-step process involving the nucleation of a chain of small precipitates along the climbing dislocation followed by coarsening into large precipitates with a spacing S. (After WIRTH and GLEITER [1981a, b].)

a) precipitate lattices;
b) void lattices;
c) dislocation-loop lattices;
d) dislocation lattices*;
e) point-defect lattices, flux-line and magnetic-bubble lattices;
f) long-period antiphase boundary structures;
g) domain boundaries in ferromagnetic and ferroelectric materials**.

* For sub-boundaries see § 2.2.5, for periodic structures during fatigue see ch. 27.
** The arrangement of domain boundaries in ferromagnetic materials is discussed in ch. 29.

4.5.1. Periodic structures due to long-range interaction forces

4.5.1.1. Precipitate lattices. Several studies by means of X-ray diffraction and electron microscopy have revealed the existence of periodically arranged precipitates (fig. 22a) in alloys of Cu–Ni–Co, Cu–Ni–Fe, nickel-base alloys containing γ' (Ni_3X) precipitates, Cu–Ti, Au–Pt, Au–Ni, Co–Fe, Co–Nb, Co–Ti, Al–Zn, Fe–Bi, Fe–Be, as well as in Alnico-Ticonel alloys. The models first proposed (ARDELL *et al.* [1966] and KHACHATURYAN [1969]) to account for the formation of periodic precipitate arrays were based on (long-range) elastic interaction forces between the precipitates, due to coherency strain between the precipitates and the surrounding matrix. Both the precipitates and the matrix were assumed to be elastically isotropic. JOHNSON and LEE [1979] refined these approaches by including the strain fields induced by neighboring inclusions and by considering second-order terms. Elastically strained particles of arbitrary shape but identical moduli in an anisotropic medium were also shown (KHACHATURYAN [1969], JOHNSON and LEE [1979] and MORI *et al.* [1978]) to form periodic arrays. The arrays correspond to one of the 14 Bravais lattices.

In the particular case of spherical inclusions in a cubic matrix with a negative anisotropy parameter, a simple cubic lattice of precipitates was found to form the minimum-energy arrangement which is stable with respect to externally induced fluctuations. Precipitates positioned along <100> directions of the matrix turned out to exhibit attractive interaction forces with a maximum value at 2–3 precipitate radii. This result may provide an explanation for the frequently observed alignment of precipitates along <100> directions. For <110> and <111> alignments, the interaction forces depend on the anisotropy factor of the matrix. <111> alignment in Mo is found to result in attractive forces, whereas the precipitates in the same arrangement in Cu and Ni repel. By applying these results to inclusions associated with a dipole-type strain field embedded in an iron lattice, a precipitate lattice with bcc structure was found to be stable. This arrangement corresponds approximately to the arrangement of N atoms in $Fe_{16}N_2$. So far, the discussion of precipitate lattices has been limited to systems in which the precipitation process occurs by nucleation and growth. In systems decomposing by a spinodal process, periodic arrangements of precipitates result from the time-dependent growth of concentration fluctuations. The processes involved and the factors governing the periodicity are discussed in ch. 15.

4.5.1.2. Void lattices. EVANS' [1971] report on the creation of a stable bcc array (superlattice) of voids in irradiated Mo stimulated numerous studies on void lattices in other systems. Void lattices have been seen, for example, in Ni, Al, stainless steel, Mg, Mo, Mo–Ti, Nb, V, W and NbO, BaF_2, SrF_2, CaF_2 (fig. 22b). Two kinds of models have been advanced to explain the formation of void lattices.

The observed symmetry of the void lattices has originally initiated an interpretation in terms of equilibrium thermodynamics assuming elastic interaction forces between the voids (STONEHAM [1971], TEWARY [1973], WILLIS [1975]). As these theories do not include the radiation damage explicitly, they cannot explain the observed influence of temperature and damage type. Moreover, this approach would not predict void lattice formation in isotropic crystals such as tungsten in contrast to the experimental observation.

The second type of theoretical approach to explain void lattices, dislocation pattern-

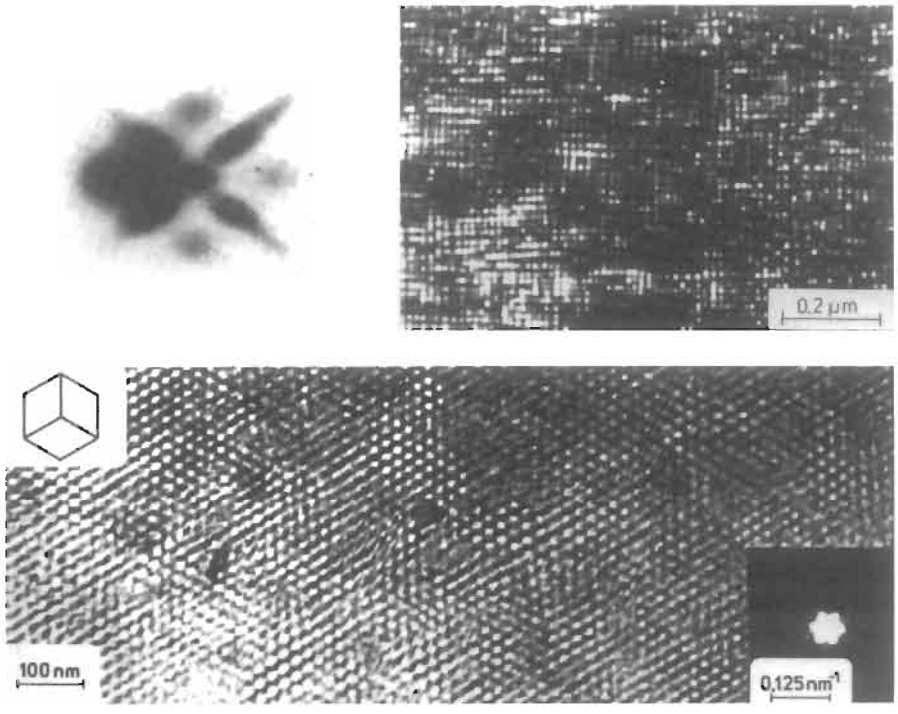

Fig. 22. (a) Dark-field electron microqraph and small-angle X-ray diffraction pattern of the precipitate lattice formed in an Fe–Be alloy (19.5 at% Be) after a 2 h anneal at 400°C. The specimen orientation is (100). (From TIAPKIN *et al.* [1976].) (b) Void lattice in < 111 > fluorite. The diffraction pattern shows superlattice reflections around the transmitted beam. The structure of the void lattice is indicated in the diagram. (From CHADDERTON *et al.* [1976].)

ing, etc., are based on the concept of synergetics. These models differ significantly concerning the basic processes involved. Some models consider only one type of point defects, e.g., vacancies (RYAZANOV and MAXIMOV [1981]). The experimental fact that the patterning saturates with increasing irradiation dose suggests, however, an additional destructive process to operate which removes point defects from the system. The most obvious destruction process is the point defect annihilation. For instance, self-interstitials may annihilate with vacancies in the materials forming vacancy type dislocation loops and voids. In the latter case, vacancy condensation and capture of vacancies and interstitials represent the constructive and destructive processes, respectively. The competition between such processes have been shown to induce pattern formation in irradiated systems (ABROMEIT [1989], TRINKHAUS *et al.* [1989], ABROMEIT and WOLLENBERGER [1988]). The void lattices are proposed to be the pattern formed in crystals during irradiation resulting in point-defect generation (cf. detailed account in ch. 18, § 4.6).

4.5.1.3. Dislocation-loop lattices. The first observation on the formation of dislocation loop lattices has apparently been made in neutron-irradiated copper. In

subsequent years, periodic arrays of dislocation loops have been detected in Al, Ni, U, BeO, Ti, Mg and Zr. In the case of Ni and Al, ordered clusters of loops were observed. Stereomicroscopy revealed that the clusters consisted of about six loops forming a fcc superlattice (STIEGLER and FARRELL [1974]). As the lattice regions between the clusters were found to be elastically strained, elastic interaction forces were proposed to be the dominant factor for the formation of the loop lattice.

Recent theoretical approaches to explain the formation of loop lattices are based on self organization principles. In fact, the dynamic models discussed in § 4.5.1.2 seem to apply to dislocation loop and void lattices as well.

4.5.1.4. Point-defect lattices. By analogy with the formation of void lattices, point defects may be expected to form ordered arrangements. This idea is indeed confirmed by recent studies on vacancy and interstitial lattices in certain alloys (cf. HIRAGA [1973] and JUNG and TRENZINGER [1974]). In alloy forming vacancy lattices, e.g., vanadium carbides of the V_6C_5 type, a variation in the alloy concentration between V_6C_5 and V_8C_7 did not result in an expansion (or contraction) of the spacing of the carbon vacancies, but rather caused the formation of a one-dimensional long-period superlattice structure consisting of enantiomorphic domains of the superstructure V_6C_5. For obvious reasons, the linear dimension of the enantiomorphic domains depends on the vacancy (carbon) content and increases with the increase in carbon vacancies. In vacancy lattices elastic interaction forces are believed to be the most important parameter. In pure metals, vacancy or interstitial lattices have not yet been revealed experimentally. However, calculations based on the vacancy–vacancy interaction potential showed that vacancy lattices may exist with a simple cubic structure aligned parallel to the identical axis of the host lattice (CHANG [1976]). The vacancy lattice constant was found to be about three times the lattice constant of the atomic lattice in the case of K and Na.

4.5.1.5. Long-period antiphase boundary structures. Ordered alloys, mostly of fcc structure in the disordered state, exhibit in the ordered state a regular three-dimensional array of antiphase boundary (APB) structures. Ordered structures of this type, which are called "long-period antiphase boundary structures", are treated in ch. 3, § 11.2. An excellent review dealing with various aspects of order/disorder phenomena in materials has been published recently (CAHN [1994]).

4.6. Microstructure in the vicinity of point defect sources and/or sinks

4.6.1. Enhanced precipitation and precipitate-free zones

The significance of point-defect sources/sinks for the precipitation of solute atoms from supersaturated solid solutions was first demonstrated by BARNES *et al.* [1958] for the *enhanced precipitation* of helium atoms in the vicinity of point-defect sources. Helium atoms were injected into metals (spectroscopically pure Cu and Be) by bombardment with alpha particles. On subsequent heating, the He atoms have a tendency to precipitate within the metal in the form of gas bubbles and, to acquire the extra space necessary for this, they capture vacancies. Thus a blanket of bubbles forms in the vicinity of a vacancy source. For low He contents and large grain sizes, grain boundaries as well as dislocations are the most important vacancy sources. For small grains, grain bound-

aries are the dominant suppliers. These results were confirmed later for a variety of other metals. *Precipitate-free zones* denuded of second-phase particles adjacent to grain boundaries in age-hardened alloys were originally attributed to the localized depletion of solute arising from preferential precipitation at the grain boundaries. However, it was soon recognized that local depletion of vacancies might be the more important factor, as a critical concentration of vacancies may be required for precipitate nucleation. In fact, this idea was discussed in terms of the thermodynamics of solute clustering (LORIMER and NICHOLSON [1969]) and in terms of the precipitation kinetics (PASHLEY *et al.* [1967]). Evidence for the local depletion of vacancies by annihilation at the boundaries was obtained from electron microprobe measurements and energy-analyzing electron microscopy for Al–Ag and Al–Zn–Mg alloys. The results of both investigations showed no solute depletion in the vicinity of the boundaries. In this simplified picture no coupling between vacancy flow and solid distribution is assumed. However, if a binding energy exists between solute atoms and vacancies, the vacancy flow from or to vacancy sources/sinks is necessarily coupled with a solute flow and thus produces a solute gradient in the vicinity of vacancy sources/sinks, such as grain boundaries, dislocations, pores, or free surfaces (JOHNSON and LAM [1976] and ANTHONY [1970]).

The solute segregation generated by vacancy flow involves two processes: the dragging of solute atoms by the moving vacancies and the reverse atom flow which is a consequence of vacancy flow. The first process dominates if the binding energy (E) between a vacancy and a solute atom is much greater than the thermal energy (kT). Under these circumstances, a solute atom is dragged to (from) the vacancy sink (source) so that solute enrichment (depletion) of the sink (source) regions will result. As a consequence, an enhanced density of precipitates forms in the vicinity of the sink. The opposite type of solute distribution may result in the second case ($E \ll kT$). For $E \ll kT$, solute atoms may be pumped in or out of the sink region depending on the relative diffusivity of solute and solvent atoms. When a vacancy flows into an enclosed sink region, an atom as a consequence must simultaneously flow out of this region. If the solute and solvent atoms in this region have identical mobilities, the ratio of solute to solvent atoms will remain the same as the original ratio. However, if the mobility of the solute atoms is greater than of the solvent atoms, proportionately more solute than solvent atoms will be moved out of the enclosed reqion by intruding vacancies, producing a solute-depleted sink zone. The solute depletion of the sink region will not continue indefinitely but will stop when the solute flow generated by the vacancy flux is balanced by the opposing solute flow produced by the solute gradient.

Two special *solute pumping* processes were proposed for *hydrogen* in stress gradients. The first mechanism (the Gorsky effect, for a review see VÖLKL [1972]) arises because hydrogen dissolved in a metal expands the crystal lattice for the host material. Hence, if a crystal contains a gradient in dilatation, the hydrogen concentration is enhanced in the dilatated region, e.g., in the vicinity of crack tips. The second effect (TILLER and SCHRIEFFER [1974]) is due to the redistribution of the free electrons in strain fields. Owing to this redistribution, dilatational centers (into which electrons flow) become cathodic. Hence, H^+ ions will migrate into the cathodic (dilatational) regions. Estimates for conditions typical for crack tips led to H^+ enhancements of up to ten orders of magnitude.

References: p. 935.

4.6.2. Irradiation-induced precipitation

In irradiated materials, a high supersaturation of vacancies and/or interstitials may be present. It follows from the previous section that the condensation of these point defects at suitable sinks (e.g., grain boundaries) may induce solute segregation in the vicinity of the sink. If this segregation is sufficiently strong, a local transgression of a phase boundary and, hence, irradiation-induced precipitation processes may be obtained, as has been reported for many alloy systems. For comprehensive reviews on this subject, we refer to conference proceedings (BLEIBERG and BENNET [1977] and POIRIER and DUPOUY [1979]), chs. 7 and 18.

4.6.3. Point-defect condensation

The significance of point-defect sources/sinks for the development of microstructures resulting from point-defect condensation was discovered by etch-pit studies. Etch pits were observed to form on electropolished surfaces of Al crystals during cooling from elevated temperatures. The formation of the pits was attributed to the condensation of vacancies at the surface. In polycrystalline specimens, pits were not observed in the vicinity of high-angle grain boundaries, suggesting that the vacancies in the pit-free region had been drained by the boundaries. In regions far away from the free surface, supersaturated point defects may condense in the form of dislocation loops, stacking-fault tetrahedra and/or voids which may be observed by transmission electron microscopy. The condensation process leads to a non-uniform microstructure in polycrystalline specimens in the sense that denuded zones exist near grain boundaries. As the condensation occurs by a nucleation and growth process, a certain supersaturation of point defects is required. Hence, the observation of *denuded zones* suggests a lower point-defect supersaturation in the vicinity of grain boundaries than in the perfect lattice, owing to the annihilation of point defects at the boundaries. With the exception of coherent twins and small-angle boundaries, the results suggest that high-angle grain boundaries are ideal vacancy sinks so that the width of the denuded zones is diffusion-controlled (for a review see GLEITER [1981a]).

4.7. Microstructure due to lattice defects formed by migrating grain boundaries

In recent years, it has become apparent that the microstructure of crystals growing by solid-state processes depends on the mode of crystal growth. The defect structures resulting from solid-state phase transformations and solid–liquid (glass) transformations, are discussed in chs. 15–19. In the present section, attention will be focussed on the microstructures developed due to the generation of vacancies, dislocations and twins by migrating grain boundaries. For a recent review of this field, we refer to the article by GLEITER [1981a].

Creation of vacancies. The creation of vacancies by migrating boundaries has been studied by means of the diffusion coefficient, the density, the electric resistivity and the morphology of the precipitates formed in the crystal region behind migrating boundaries (GORLIK *et al.* [1972] and GOTTSCHALK *et al.* [1980]). The observations reported suggest that behind a migrating grain boundary a high supersaturation of vacancies may exist. The high vacancy supersaturation observed was explained in terms of "growth accidents"

occurring during grain-boundary migration (GLEITER [1979]). A growth accident involves a jump of an atom of the growing crystal into the migrating boundary so that a vacant site is left behind in the lattice of the growing crystal. The excess vacancies retained in the lattice alter the properties of this crystal and exert a drag force on the migrating boundary ("vacancy drag", GLEITER [1979]) which may dominate impurity drag under certain conditions (ESTRIN and LÜCKE [1982]) (cf. also ch. 28, § 3.4.1).

Creation of dislocations. Indirect observations of dislocations created by migrating boundaries come from recrystallized materials. However, because of the high dislocation density ahead of the recrystallization front, the interpretation of these results is not unambiguous. A distinction between dislocations generated by the migrating interface and dislocations due to other processes is possible if the boundary migrates into a dislocation-free crystal or a crystal with low dislocation density. Studies of this type have been carried out in Cu, InP, InAs and Si (GLEITER *et al.* [1980]). The results obtained support the idea of dislocation generation by migrating boundaries. The generation process may be envisaged by growth accidents as well as the stress-induced dislocation emission (GASTALDI and JOURDAN [1979], GLEITER *et al.* [1980]).

Creation of two-dimensional lattice defects. The most prominent lattice defects generated during boundary migration (e.g., during grain growth) are *coherent twin boundaries* (cf. ch. 28, § 4.2). In order to explain the formation of twin boundaries during boundary migration, several models have been proposed. According to the *dissociation models* twins are formed by dissociating a grain boundary (A) into a twin boundary (T) and a new grain boundary (B). The *stimulation model* proposes that a twin boundary is created if a growing recrystallized grain meets a dislocation-bearing fragment which lies accurately in a twinned orientation to it. Since the fragment has discharged its dislocations, it is now stress-free and able to grow at the expense of the surrounding deformed matrix. The *coalescence model* proposes twin boundaries to be formed if the orientation relationship between the impinging grains corresponds exactly to a twin orientation. The *growth-accident hypothesis* of twin-boundary formations follows the concept that twins are formed and terminated by errors of the stacking of the <111> planes which happen in a random way. Studies by optical microscopy, thermo-ionic and photoemission microscopy, transmission electron microscopy, X-ray topography, grain-boundary migration experiments in bicrystals and polycrystals have been reported (for a review see GLEITER [1981a]). The results of these studies are inconsistent with the dissociation, the stimulation and the coalescence hypotheses. The observations so far available seem consistent only with the growth-accident hypothesis. In fact, in situ observations of twin formation in Al by X-ray topography agree with the evolution, shape and growth direction predicted by the growth-accident theory (GASTALDI and JOURDAN [1979]).

4.8. Microstructure of glasses

Historically, the observation and interpretation of microstructures have only dealt with crystalline materials. Indeed, until the late 1950s noncrystalline materials, e.g., oxide glasses, were regarded as free of all microstructure. This viewpoint was fostered in part by earlier triumphs of the random network theory of glass structure (ZACHARIASEN

[1932], WARREN [1937]) and was strengthened by the implicit glass engineering goal of this era: produce a homogeneous, single-phases product through fusion. As will be discussed below, this concept of a microstructure-free vitreous state has been seriously questioned in the last decade (ROY [1972]). This challenge has progressed sufficiently to occasion a rethinking of nearly all aspects of the fabrication and characterization of noncrystalline materials.

To a large extent this more modern concept of glass materials evolved from the discovery of the ability to induce, by appropriate thermal treatment, a clearly discernible and well-controlled microstructure in glasses. This microstructure is now recognized to be either crystalline or noncrystalline. Moreover, the occurrence of the noncrystalline variety is so ubiquitous that it has been suggested that its occurrence may be an intrinsic characteristic of all glass-forming melts (ROY [1972]).

4.8.1. Microstructure of amorphously phase-separated glasses

There are two ways of producing amorphously phase-separated glasses. First, one may simply prepare a glass-forming melt, quench it to room temperature and assess the extent to which the process has taken place.

A second and more controllable method involves the isothermal annealing of glass above its transformation temperature (ch. 7, § 9.1). One thus extends the amount of time available for the process to proceed. By intermittent examination of samples for telltale opalescence at various times and temperatures, it is possible to construct a time–temperature-transformation diagram. The microstructure developed in this process depends on the curvature of the free-energy vs. concentration curve. The loci of equilibrium compositions trace out the immiscibility gap. The loci of the inflection points delineate the region of spinodal decomposition. Between the equilibrium compositions and the inflection points, single, phase glasses transform into two-phase glasses by nucleation and growth. In this case, the microstructure is characterized by spherical glassy regions dispersed through a continuous glassy matrix of different chemical composition. If the decomposition is spinodal a microstructure characterized by a high interconnectivity of both glassy phases and irregularly shaped diffuse boundaries results.

Glass–glass phase transformations are, however, not limited to immiscibility effects. For example, it is known that the viscosity of liquid sulfur changes by a factor of two thousand when heated over the narrow temperature range 158–166°C (BACON and FANELLI [1943]). The low-temperature low-viscosity melt is thought to be constructed of 8-member rings, whereas the high-temperature high-viscosity melt is regarded as made up of long sulfur chains. Both liquids are in thermodynamic equilibrium (POWELL and EYRING [1943]). Evidence for a second-order phase transformation between the two liquid fields has been presented, leading to a microstructure of finely dispersed clusters with different molecular structure.

In addition to these considerations there is evidence for clustering effects in silicate glasses. Clusters have been defined as cooperative compositional fluctuations surrounded by melt of less organized structure (UBBELOHDE [1965]). These clusters are not necessarily equivalent to the crystalline nuclei. It has been suggested that such clusters could be "frozen in" during quenching of a glass-forming melt (MAURER [1956]).

4.8.2. Microstructure of partially crystallized glasses

Figure 23 summarizes the major reaction paths for crystallization of glasses and the resulting microstructures. Path (1) represents the direct transformation of a pure single-phase glass into a more stable crystalline phase. This transformation involves both the creation of stable nuclei and the subsequent growth of the crystalline phase.

In contrast to path (1), the development of an intermediate amorphous phase as in path (2, 3) and also for path (2, 4, 5) is well documented for a number of glassforming systems. A good representative of the former is the crystallization of Al_2O_3-SiO_2 glasses (MACDOWELL and BEALL [1969]). The latter path has been observed in classical glass ceramic compositions, e.g., Li_2O-SiO_2-Al_2O_3-TiO_2 (DOHERTY *et al.* [1967]). On cooling, glasses in this system show amorphous phase separation on a scale of about 5 nm. On reheating, this microstructure promotes formation of a nucleant phase, $Al_2Ti_2O_7$, which in turn crystallizes a major crystalline phase of this system, β-eucryptite.

Path (6, 5) represents the case where small amounts of metals such as Ag, Au, Pt, Cu, Rh, Pd, etc. are incorporated into a glassy matrix and by suitable control of initial concentration, melting conditions, thermal history, and in some cases (Au, Ag) exposure to actinic radiation, nanometer-sized particles of these metals are precipitated in the glass. Since the process involves both a reduction to a metallic state and diffusiPon of the reduced species to form a particle, their mean size may vary over a wide range depending on the interplay of the above factors. MAURER [1959] has shown that the minimum size of a gold particle capable of catalyzing lithium metasilicate is about 8 nm (10,000 atoms). This is in contrast to the smallest, stable gold particle which may contain only three or four atoms. Thus, the need for microstructure control to achieve catalyzed crystallization is apparent. It has been recognized for some time that the presence of these metal particles induces a characteristic color in the bulk glass. Thus, gold and copper particles give rise to a magneta color, silver to a yellow cast, and platinum to a somewhat dull grey appearance. Similarly, selenium gives a characteristic pink color in soda-lime silica glasses (average particle size 5–20 nm). Since this pink color is complementary to the bluish green arising from ionic iron in these same glasses, this element is used extensively in the glass container industry as a decolorizer. It is here that the control of microstructure in glass is crucial because the precise shade of pink required to achieve decolorization depends on composition, furnace atmosphere, and thermal history (PAUL [1975]). The need to understand the origin and significance of microstructure in glass to render a product commercially acceptable is evident.

Still another group of technologically important glasses which are partially crystalline is the photochromic glasses (ARANJO and STOOKEY [1967]). Their photochromic behavior arises from minute silver halide crystals which may be regarded as being suspended in an inert glass. Satisfactory photochromic properties are obtained when the average particle size is about 5–10 nm at a concentration of $\sim 10^{15}$ particles/cm^3. This corresponds to an average particle separation distance of about 60 nm. This separation distance is crucial since the inert glass host prevents diffusion of the halogens freed by absorption of light by the halide crystal. Thus, recombination with free silver within the halide crystal is enhanced. It is this alternate decomposition and recombination that gives rise to the variable optical transmission of these glasses.

References: p. 935.

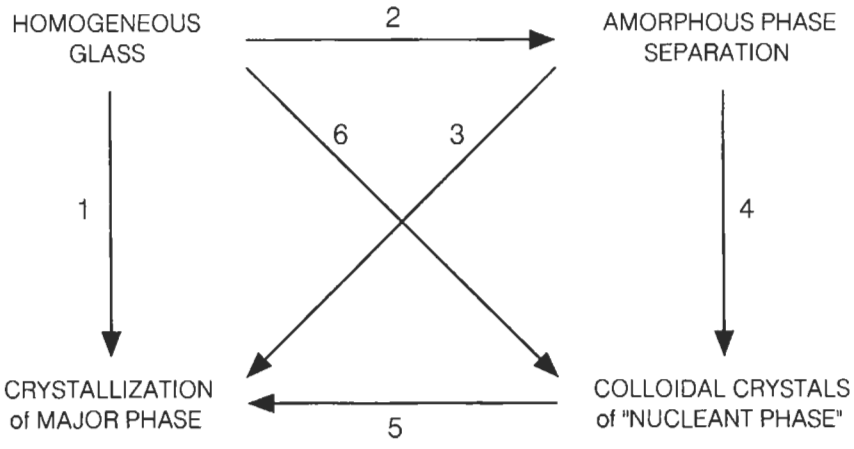

Fig. 23. Various paths associated with potential crystallization of glass forming melts. (From STEWART [1972].)

5. *Nanostructured materials*

5.1. Materials with reduced dimensionality, reduced dimensions and/or high densities of defect cores

The perfect single crystal of infinite size has been the model system of solid state physics for several decades. Remarkable progress was achieved in the physical understanding of solids by means of this idealized approach. However, about 40 years ago, scientists started to realize that the disorder present in most real materials cannot be treated as a weak perturbation of the corresponding ideally ordered crystals. In fact, a variety of new physical effects (e.g., new types of phase transitions, quantum size effects, new transport phenomena, etc.) were discovered which existed only in imperfectly ordered solids. In fact, if the characteristic dimensions (e.g., the diameters of small spheres or the thickness of a thin film) of the crystalline regions of a polycrystal approach certain characteristic lengths such as an electron wavelength, a mean free path, a coherency length, a screening length, a correlation length, etc. one obtains materials the properties of which are controlled by their reduced dimensionality or their reduced dimensions and/or their high density of defect cores (e.g., grain boundary cores). As a kind of introduction, let us consider two specific examples. The first example is shown in fig. 24 in the form of a compositional superlattice characterized by a length scale, d, which characterizes the thickness of the layers. If d is equal or less than the mean free path of the conduction electrons, the electronic band structure and, hence the electric properties of this materials differ significantly from the ones of a superlattice with the same chemical composition but with a modulation length, d, that is much larger than the electronic mean free path (cf. section 5.2). The second example to be considered here is a crystalline solid with a high density of grain boundary (i.e., defect) cores (fig. 36, below). About 50% of the atoms are located in the cores of these grain boundaries. In

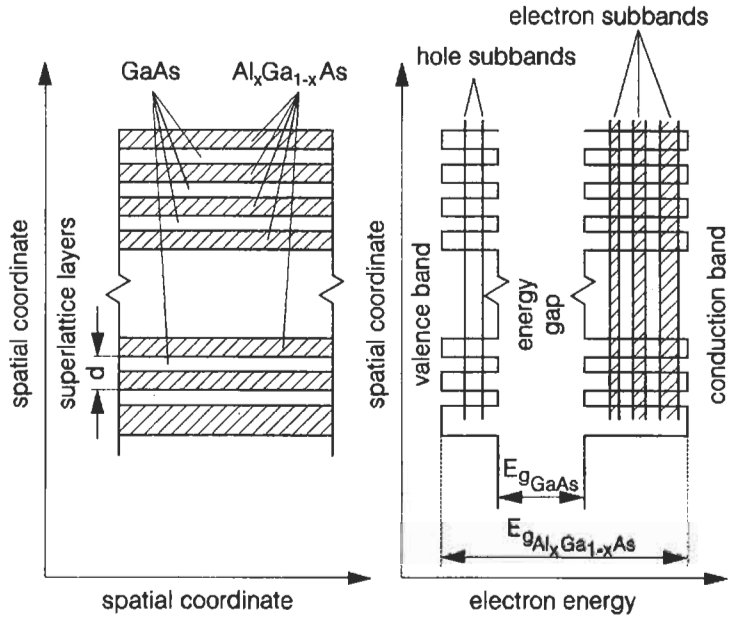

Fig. 24. Schematic illustration of the layer sequence (left side) and of real-space energy-band profile (right side) of a GaAs/Al_xGa_{1-x} as superlattice. Both, the GaAs and the Al_xGa_{1-x} as layers are assumed to be equally thick. E_g is the energy of the band gap edge.

grain-boundary cores, the atomic structure (e.g., the density and the nearest neighbor coordination) differs from that of a perfect crystal with the same chemical composition. Hence the atomic structure and the properties of a material with a structure as shown in fig. 36 may deviate (in some cases by many orders of magnitude) from those of the corresponding single crystal (cf. sections 5.4, 5.5 and 5.6). Materials exhibiting reduced dimensionalities, reduced dimensions and/or high densities of defect cores are termed nanostructured materials, because the typical size of the crystalline regions or of another characteristic length scale in such materials are in the order of a few nanometers. In recent years, the following five types of nanostructured materials have attracted widespread scientific attention:

1) Thin metallic, semiconducting or polymeric films with clean or coated surfaces.
2) Man-made superlattices and quantum well structures.
3) Semicrystalline polymers and polymer blends.
4) Nanocrystalline and nanoglassy materials.
5) Nanocomposites made up of metallic, covalent, ionic and/or molecular components.

This paragraph will be limited to the materials mentioned in 2, 3, 4 and 5. Concerning thin films and free surfaces we refer to chapters 28 and the numerous reviews in the literature and textbooks on surface science as well as thin solid films.

References: p. 935.

5.2. Man-made superlattices and quantum-well structures

In 1969 research on man-made superlattices was initiated by the proposal of Esaki and Tsu to engineer the electronic structure and properties of semiconductors by generating superlattices with a periodicity shorter than the electronic mean free path either by alternating the chemical composition (compositional superlattice) or the doping (doping superlattice) of consecutive layers in a multilayer structure.

The first *compositional superlattice* was grown from the material system $GaAs/Al_xGa_{1-x}As$. The layer sequence (chemical composition) and the real-space energy band structure of the electrons in such a superlattice are illustrated in fig. 24. The different energy levels of the bands of the two components at the heterointerfaces determine the potential barriers for the electrons and holes in the vertical direction (fig. 24), and thus define the periodic superlattice potential in the conduction and in the valence bands. The characteristic feature of this superlattice is that layers of a narrow-gap semiconductor are sandwiched between layers of a wide-gap semiconductor. This structure results in two square quantum wells: one for the electrons and one for the holes. Figure 25 displays the corresponding density of states in such a two-dimensional system in comparison to the parabolic curve of the classical (three-dimensional) free electron gas. If the electron mean free path exceeds the superlattice periodicity, resonant tunneling between adjacent subbands occurs. Technological applications of such superlattice structures lie primarily in the optoelectronic regime, comprising injection lasers, light emitting diodes, avalanche photo diodes and photoconducting detectors.

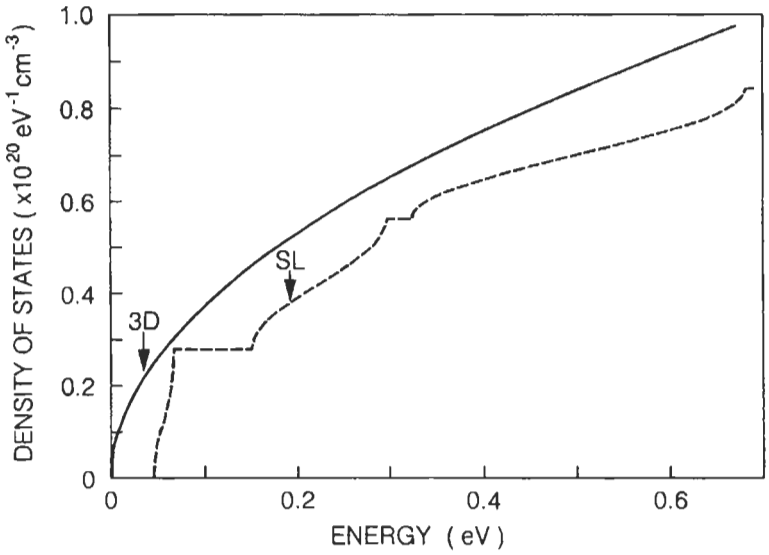

Fig. 25. Comparison of density of states in the three-dimensional (3D) electron system with those of a superlattice (SL) assuming a quantum well and barrier width of 10 nm, and an effective electron mass 0.067 m_0 in the SL. The first three subbands are indicated (MENDEZ and VON KLITZING [1989]. m_0 is the mass of the free electron).

The term *doping superlattices* refers to periodic arrays consisting of layers of the same semiconductor doped in two different ways e.g., n- and p-doped layers. The unusual electronic properties of doping superlattices derive from the specific nature of the superlattice potential which, in this case, is the space charge potential of ionized impurities in the doping layers. This is in contrast to the compositional superlattices (fig. 24), in which the superlattice potential originates from the different band gaps of the constituents. The space charge potential in the doping superlattices modulates the band edges of the host material in such a way that electrons and holes become spatially separated (fig. 26). This separation can be made nearly perfect by the appropriate choice of the doping concentrations and the layer thicknesses. One of the attractive features of doping superlattices is that any semiconductor that can be doped in both n- and p-type in well controlled ways can be used as the host material. Another advantage of doping superlattices originates from their structural perfection. The relatively small concentrations of impurities used in doping superlattices (typically 10^{17}–$10^{19}/cm^{-3}$), induce only minor distortions of the lattice of the host material. Thus, doping superlattices do not contain interphase boundaries as does compositional superlattice. The absence of any significant disorder or misfit strains leads to unprecedented electron and hole mobilities. Doping supperlattices have had profound impact on not only the progress made in recent years in the physics of two-dimensional electronic systems (quantum Hall effect, Shubnikov–de Haas oscillations) but also on device applications such as high-speed MODFETS. For further details we refer to some of the excellent reviews in this rapidly growing area of research (MENDEZ and VON KLITZING [1989], FERRY *et al.* [1990], KIRK and REED [1992]).

5.3. Semicrystalline polymers

Semicrystalline polymers constitute a separate class of nanostructured materials. The remarkable feature of this class of polymers is that the nanostructured morphology is always formed if the polymers are crystallized from the melt or from solution unless crystallization occurs at high pressure or if high pressure annealing is applied subsequent to crystallization. If a polymer is crystallized from a dilute solution, isolated single polymer crystals or multilayer structures consisting of stacks of polymer single crystals result (fig. 27). Inside the crystals, the atoms forming the polymer chains arrange in a periodic three-dimensional fashion. The interfaces between neighboring crystals consist of both macromolecules folding back into the same crystal and tie molecules that meander between neighboring crystals. The typical thicknesses of the crystal lamellae are in the order of 10 to 20 nm. These relatively small crystals thicknesses have been interpreted in terms of one of the following models. The first model hypothesizes the formation of the thin crystallites to result from nucleation kinetics. If the height of the energy barrier for the formation of a critical nucleus of a chain-folded polymer crystal formed in a supersaturated solution is computed by means of homogeneous nucleation theory, it is found that the energy barrier of a critical nucleus consisting of extended chain molecules is larger than the barrier height for a nucleus of folded chains. The physical reason for this energy difference is as follows. Extended chain crystallization

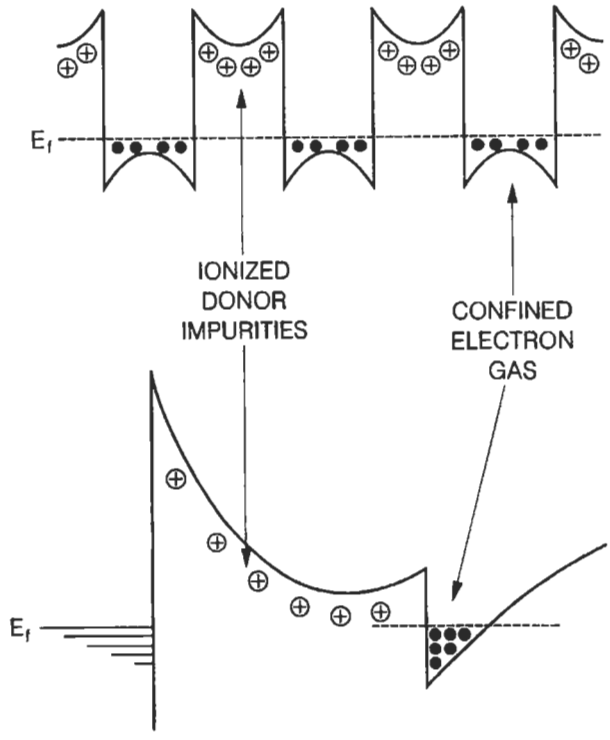

Fig. 26. Modulation doping for a superlattice and a heterojunction with a Schottky junction. E_f indicates the position of the Fermi energy (MENDEZ and VON KLITZING [1989]).

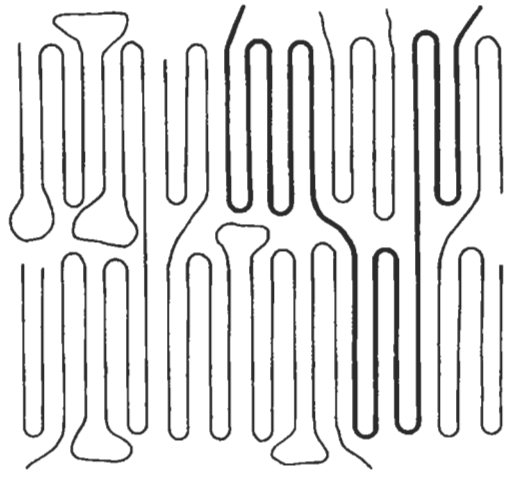

Fig. 27. Schematic representation of the conformation of chain-folded polymer molecules in a semicrystalline polymer. One molecule belonging to adjacent crystals is indicated as a heavy line.

results in a needle-shaped critical nucleus, the length of which is equal to the length of the molecular chains. Hence the system is left with only one degree of freedom to reduce the energy barrier for the critical nucleus. This reduction occurs by adjusting the diameter of the needle. However, if chain folding occurs, the energy barrier associated with the critical nucleus can be minimized by adjusting the size of the nucleus in all three dimension. Detailed computations reveal that the energy barrier for chain folded nuclei is in general significantly lower than for extended chain crystallization. The second group of models for chain-folding is based on the excess entropy associated with the folds relative to an extended-chain crystals. If the Gibbs free energies of an extended chain crystal and of a chain-folded crystal are compared, the chain folds are found to increase the internal energy of the system. However, the chain folds also contribute to the entropy of the system. Hence, at finite temperatures, a structure of lowest Gibbs free energy is obtained, if a certain concentration of chain folds is present in the crystal. In other words, chain-folded crystals have a lower Gibbs free energy at finite temperatures than extended chain crystals (cf. also ch. 32, § 2.2–2.6).

Polymers crystallizing from the molten state form more complex morphologies. However, the basic building blocks of these morphologies remain thin lamellar crystals. Figure 28 shows spherulitic crystallization of thin molten polymer film. The spherulites consist of twisted lamellae which exhibit radiating growth. If the molten thin film is strained during solidification, different morphologies may result, depending on the strain rate. However, all of these morphologies have in common that the macromolecules are

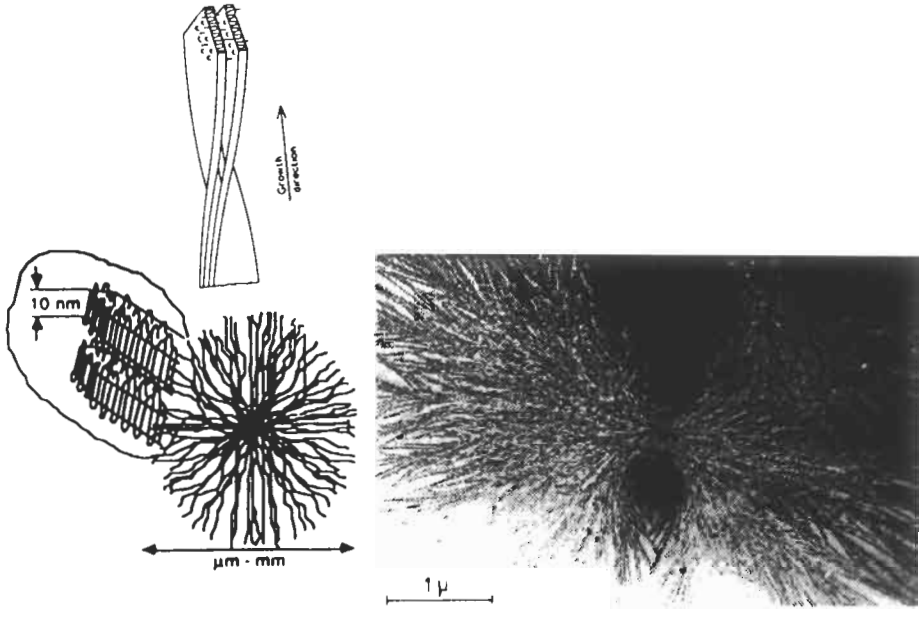

Fig. 28. Bright field transmission electron micrograph (defocus contrast) of a two-dimensional spherulite in isotactic polystyrene. The spatial arrangement of the lamellae formed by the folded macromolecules is indicated on the left side (PETERMANN [1991]).

References: p. 935.

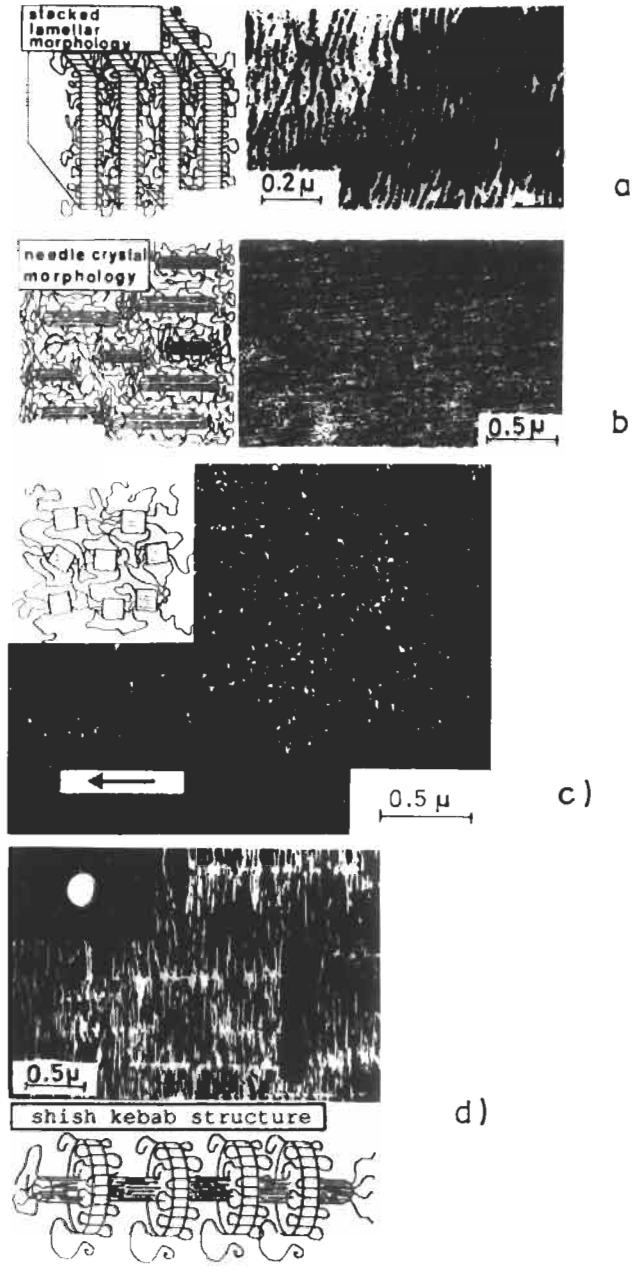

Fig. 29. (a) Stacked lamellar morphology in polyethylene (TEM bright field). (b) Needle-like morphology in polybutene-1 (TEM bright field). (c) Oriented micellar morphology in polyethylene terephthalate (TEM dark field micrograph). (d) Shish-kebab morphology in isotactic polystyrene (TEM dark field micrograph) (PETERMANN [1991]).

more or less aligned in the straining direction. High temperatures and small strain rates favour a stacked lamellar morphology (fig. 29a), high temperatures combined with high strain rates result in needle-like arrangements (fig. 29b). Low temperatures and high strain rates lead to oriented micellar structures (fig. 29c). The transition between these morphologies is continuous and mixtures of them may also be obtained under suitable conditions (fig. 29d). The way to an additional variety of nanostructured morphologies was opened when multicomponent polymer systems, so-called polymer blends, were prepared. For thermodynamic reasons, polymer blends usually do not form homogeneous mixtures but separate on length scales ranging from a few nanometers to many microns depending on the thermomechanical conditions of crystallization and the molecular structure of the costituents involved. So far the following types of nanostructured morphologies of polymer blends have been reported for blends made up by one crystallizable and one amorphous (non-crystallizable) component: Type I morphology: The spherulites of the crystallizable component grow in a matrix mainly consisting of the noncrystallizable polymer. Type II morphology: The non-crystallizable component may be incorporated into the interlamellar regions of the spherulites of the crystallizable polymer. The spherulites are spacefilling. Type III morphology: The non-crystallizable component may be included within the spherulites of the crystallizable polymer forming domains having dimensions larger than the interlamellar spacing. For blends of two crystallizable components, the four most frequently reported morphologies are: Type I morphology: Crystals of the two components are dispersed in an amorphous matrix. Type II morphology: One component crystallizes in a spherulitic morphology while the other crystallizes in a simpler mode e.g., in the form of stacked crystals. Type III morphology: Both components exhibit a separate spherulitic structure. Type IV morphology: The two components crystallize simultaneously resulting in so-called mixed spherulites, which contain lamellae of both polymers.

Morphologies of lower complexity than spherulites, such as sheaves or hydrides may also be encountered. In these cases, the amorphous phase, may be arranged homogeneously or heterogeneously depending on the compatibility of the two components. The morphology of blends with one crystallizable component has been studied for a variety of macromolecular substances e.g., poly(ε-caprolactrone)/poly(vinylchloride), poly(2,6dimethyl-phenylene oxide)/isotactic polystyrene, atactic polystyrene/isotactic polystyrene blends.

Block copolymers constitute a third class of nanostructured polymers. All macromolecules of a block copolymers consist of two or more, chemically different sections which may be periodically or randomly arranged along the central backbone of the macromolecules and/or in the form of side branches. An example of a block copolymer are atactic polytyrene blocks alternating with blocks of polybutadiene or polyisoprene. The blocks are usually non-compatible and aggregate in separate phases on a nanometer scale. As an example for the various nanostructured morphologies possible in such systems, fig. 30 displays the morphologies formed in the system polystyrene/polybutadiene as a function of the relative polystyrene fraction. The large variety of nanostructured morphologies that may be obtained in polymers depending on the crystallization conditions and the chemical structure of the macromolecules causes the

References: p. 935.

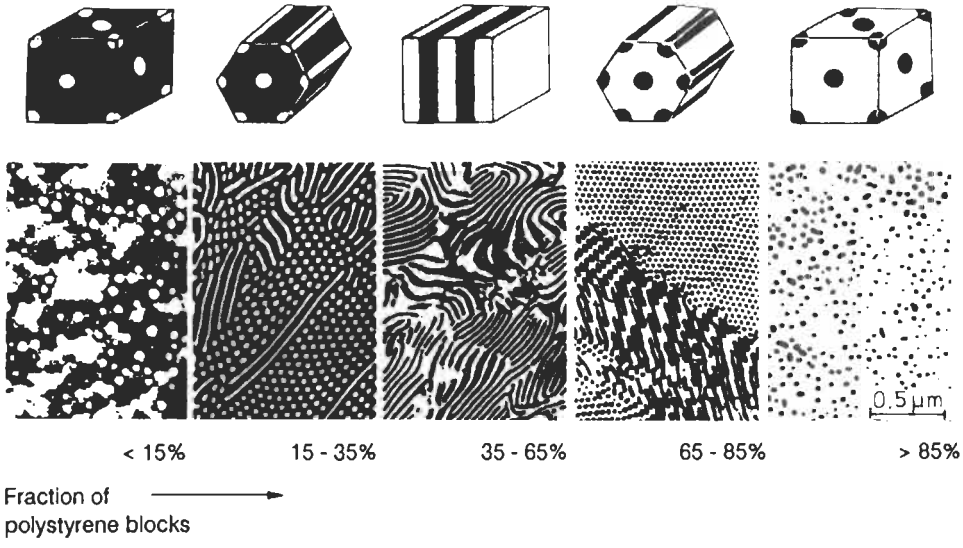

Fig. 30. Electron micrographs of the morphologies of a co-polymer consisting of polystyrene and polybutadiene blocks, as a function of the fraction of polystyrene blocks. The spacial arrangements of the polystyrene and polybutadiene in the solidified polymer are indicated in the drawings above the micrographs (PETERMANN [1991]).

properties of polymers to vary dramatically depending on the processing conditions. An example of a polymeric material with novel properties originating from a special nanoscale microstructure is shown in figs. 31 and 32. Polyethylene with a nanostructured morphology consisting of stacked crystalline lamellae (fig. 31a) exhibits remarkable elastic properties (fig. 32) if strained in tension in the direction perpendicular to the plane of the lamellae. The strain causes the lamellae to separate so that fibres of extended tie molecules form between them (fig. 31b). Upon unloading, the surface-energy of these molecular fibres causes them to shrink and thus pull the lamellar crystals together again. In other words, one obtains a material that can be strained reversibly by more than 100%. The restoring force (contraction) of the material is driven by surface energy and hence the material may be termed surface-energy pseudoelastic. If the stacked morphology is replaced by, e.g., a spherulitic microstructure, no such effects are noticed. In recent years, the large variety of nanostructured morphologies that may be generated for example in polymer blends or block copolymers has caused a rapidly expanding research activity in this type of materials (MARTUSCELLI *et al.* [1980], PETERMANN [1991]). For further details, see ch. 32.

5.4. Nanocrystalline and nanoglassy materials

5.4.1. Basic concepts

The difference between the atomic structure of nanocrystalline materials and other states of condensed matter (e.g., single crystals, glasses, quasicrystals) may be understood by considering the following two facts:

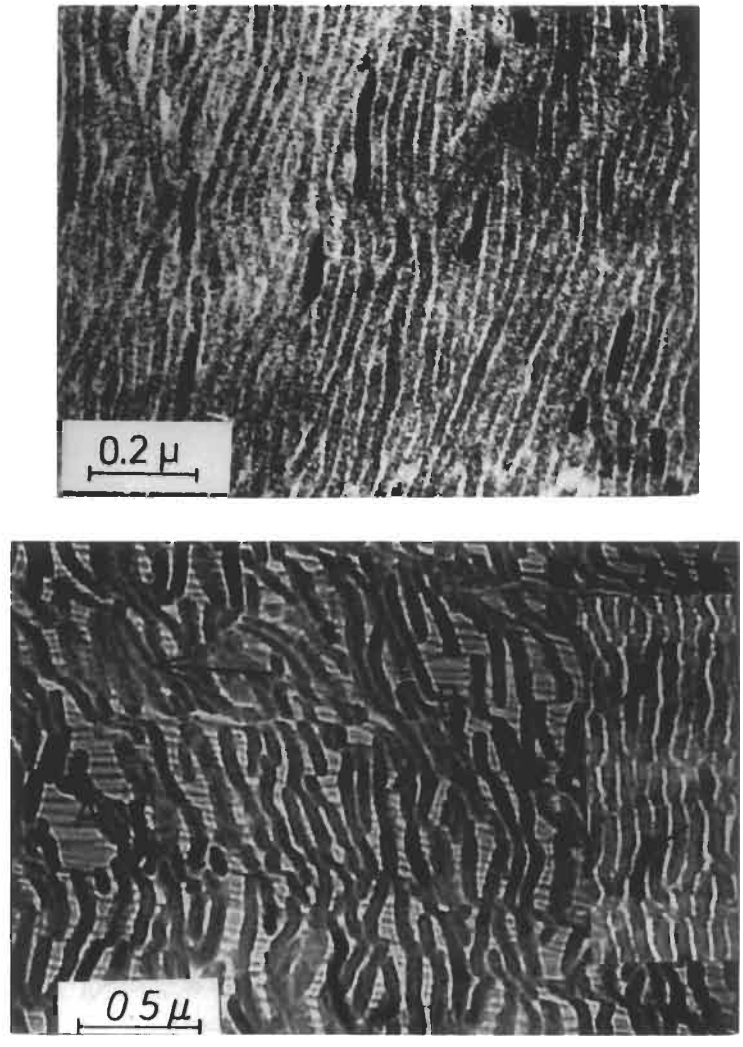

Fig. 31. (a) Defocus electron micrograph showing the stacked-lamellae structure of a polyethylene fiber. The dark regions are the crystallites. The pattern of bright lines indicates the positions of the chain folds between the lamellae (cf. fig. 27). (b) Electron micrograph of a strained polyethylene fiber (cf. fig. 31a) showing complete separation of the lamellae interconnected by fibrils. The horizontal arrow indicates the straining direction (the strain is approximately 100%).

(i) The properties of a solid depend (in addition to its dimensions and its dimensionality) primarily on its density and the coordination of nearest neighbors. The physical reason is that interatomic forces are of short-range character and hence the interaction between nearest neighbors is the most dominant factor. The total interaction energy between nearest neighbors depends on the number (coordination) of nearest neighbors and their

References: p. 935.

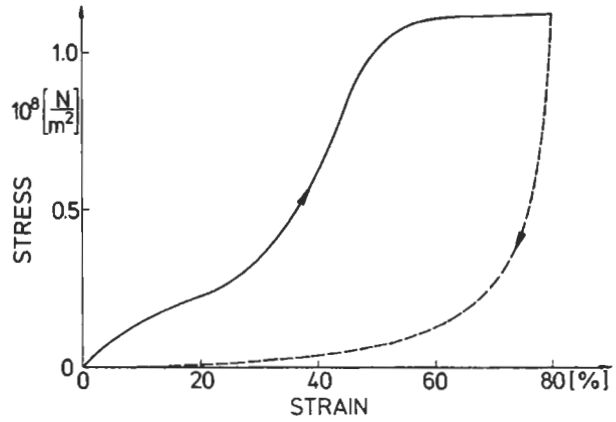

Fig. 32. Stress-strain curve for straining and destraining (in air) of a stacked-lamellae structure of polyethylene (cf. fig. 31) at 22° C at a strain rate of 0.0005/s. In the plateau region, the deformation occurs primarily by the separation of the lamellae and the formation of the fibrils between them (cf. fig. 31b).

interatomic spacing (i.e., the density). Perhaps, the best-known example demonstrating the significance of the density and the coordination of nearest neighbors is the phase transformation between diamond and graphite (fig. 33). During this phase transformation, the density and coordination number change by about 30 to 40%. The resulting variation of the properties is well known: A hard, brittle, insulating material (diamond) transforms into a soft, ductile and electrically conducting substance (graphite).

(ii) In the cores of incoherent interfaces (grain boundaries, interphase boundaries) and other lattices defects, the density and nearest-neighbor coordination deviates significantly from the surrounding perfect crystal lattice. For example, fig. 34 displays the computed

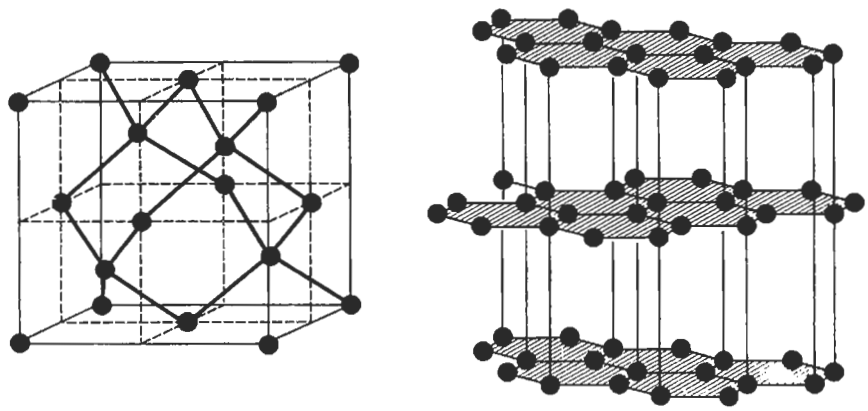

Fig. 33. Atomic structure of diamond (left side) and graphite. The carbon atoms are represented as closed circles.

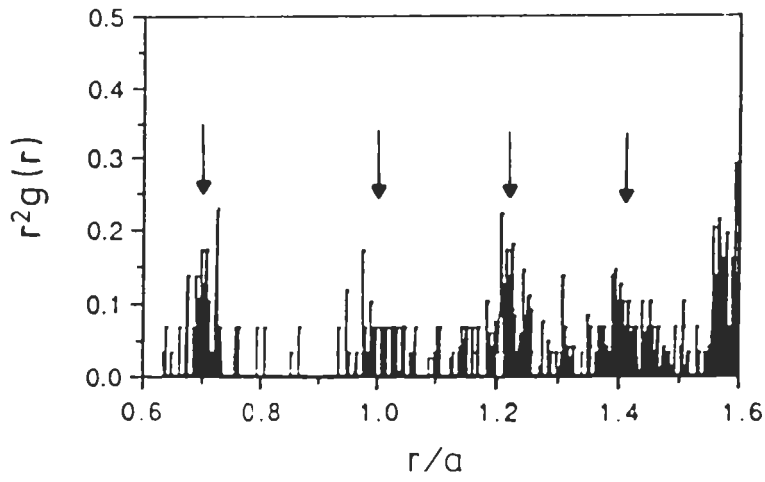

Fig. 34. Computed radial distribution function, $r^2g(r)$, for the atoms in the core of a 43.60° [100] (Σ29) grain boundary in Au (cf. fig. 35). Arrows indicate the corresponding perfect crystal peak positions. The interatomic spacings between the atoms in the boundary core are strongly affected by the presence of the interface. In the computations, the interatomic forces were represented by an embedded atom potential corresponding to Au (PHILLPOT *et al.* [1990]).

radial distribution function in a Σ29 (100) grain boundary in Au. The positions of the delta-function-like distribution peaks of the Au crystal lattice are indicated by arrows. Obviously, the boundary core structure is characterized by a broad distribution of interatomic spacings. In fact, the width of this distribution is also much larger than the one in glassy solids. Concerning the density reduction in the boundary core regions, the situation appears similar. For instance, in the case of the grain boundary shown in fig. 35 (deduced from a high resolution electron micrograph of this boundary between two misoriented NiO crystals) the density is about 80% of the cubic crystal far away from the boundary.

With these facts in mind, it was proposed (MARQUARDT and GLEITER [1980], GLEITER [1981b]) that if one generates a material that consists primarily of incoherent interfaces (i.e., a material that consists for example of 50 vol% incoherent grain boundaries and 50 vol% crystals), the structure (and properties) of such a material will deviate significantly from those of a crystal and/or glass with the same chemical composition. Materials with such a high density of interfaces were called *nanocrystalline materials**. In order to specify this idea further, let us consider a hard-sphere model of a nanostructured material which may be generated in the following way: We start off with isolated nanometer-sized

* Other terms used in the literature in the subsequent years were nanophase materials, nanometer-sized materials, nanostructured materials or materials with ultra-fine microstructures.

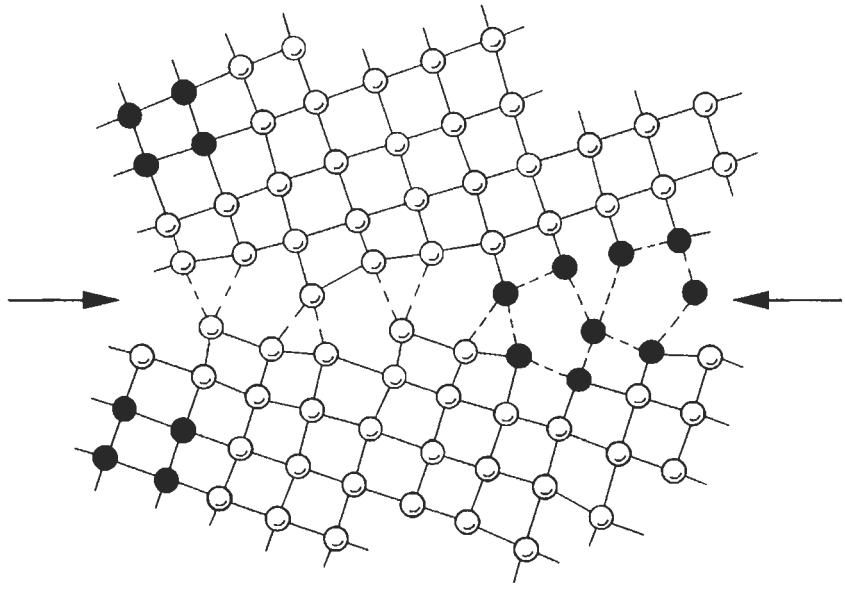

Fig. 35. Atomic structure of the core of a grain boundary between two NiO crystals that are tilted relative to one another by 36,9° about a common [100] direction normal to the plane of the figure. The structure was deduced from the high resolution electron micrograph of 36,9° [100] tilt boundary in NiO (MERKLE *et al.* [1987]). The boundary core structure may be described as a two-dimensional periodic array comprising two different pentagonal polyhedra (indicated on the right side of the boundary by broken lines). The two NiO crystals forming the boundary have cubic structure.

crystals with uncontaminated surfaces and consolidate them at high pressure. If this is done, one obtains a structure that is represented (for the sake of simplicity) in the form of a two-dimensional hard-sphere model in fig. 36. The open and full circles represent atoms all of which are assumed to be chemically identical. Different symbols (open/full circles) are used to emphasize the heterogeneity of the structure of nanostructured materials. Obviously, the structure consists of the following two components: (i) The crystallites which have all the same atomic arrangement. The only difference between the crystallites is their crystallographic orientation. The atoms in the interior of the crystallites are represented in fig. 36 as full circles. (ii) The second component of the nanocrystalline structure is formed by the interfaces (grain boundaries) between the crystallites. At the interfaces, two crystallites are joined together. Due to the different crystallographic orientations between adjacent crystallites, a region of misfit (called a grain boundary) results. In these grain boundaries, the atoms (indicated as open circles) are packed less densly than in the interior of the crystallites and the arrangement of nearest neighbors is changed relative to the crystal interior. The fraction of atoms situated in interfaces increases if the crystallites are made smaller. In fact, a straightforward estimate shows that (in the three-dimensional case) about 50% of the atoms are located in interfaces (open circles) if the crystal size is in the order of 5 to 10 nm. A crystal size

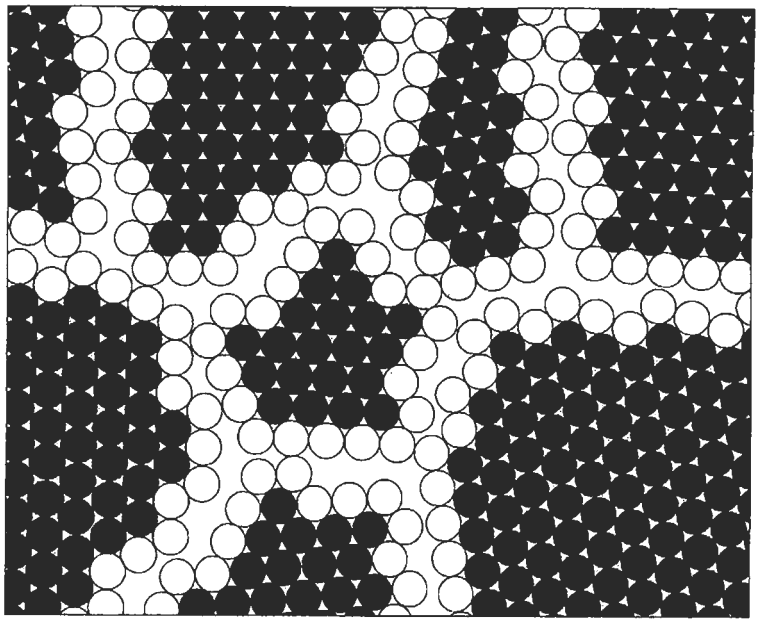

Fig. 36. Two-dimensional hard sphere model of the atomic structure of a nanocrystalline material. For the sake of clarity the atoms in the centers of the "crystals" are indicated in black. The ones in the boundary core regions are represented by open circles. Both types of atoms are assumed to be chemically identical.

in the order of a few nanometers has been the reason for calling materials that consist primarily of interfaces "nanocrystalline materials". Obviously, the structure and properties of nanocrystalline materials depend on the large fraction of interfaces with densities and nearest neighbor coordination numbers that deviate from the ones of crystalline and the glassy state and on the reduced size of the crystallites.

In order to achieve a high density of interfaces, the size of the crystals forming a nanocrystalline material has to be reduced to a few nanometers. If the size of the crystalline regions approaches a few nanometers, size effects as well as reduced dimensionality effects may become important as well. In other words, in addition to the *effects* resulting from the *variation of the density* and the *nearest neighbor coordination* in the *interfacial region*, nanocrystalline materials are also expected to exhibit *size* and *reduced dimensionality* effects.

The structural difference between a nanocrystalline and a glassy material (with the same chemical composition) may be seen by considering the physical origin of both structures. In a glass generated by quenching the molten state, the spacial density and coordination variations are controlled by the frozen-in thermal fluctuations. This is not so in nanocrystalline materials. The density and coordination numbers in the boundaries are controlled by the misfit between adjacent crystallites (fig. 36) with different crystallographic orientations. In other words, the density and the coordination are controlled by geometry (or crystallography) rather than by thermal fluctuations.

References: p. 935.

In the following section an attempt will be made to summarize our present knowledge about nanocrystalline materials. This section will be subdivided into the following five paragraphs: (a) The generation of nanocrystalline materials. (b) The atomic structure of nanocrystalline materials. (c) Nanoglasses. (d) Nanocomposites. (e) Technological applications. For obvious reasons, the summary given in this section is not intended to be encyclopaedic. In discussing the atomic structure and properties of nanocrystalline materials, we draw attention to those aspects of the experimental evidence that must be examined the most critically. The discussion of the properties will be limited to properties that appear relevant to technological application. For further details, the reader is referred to one of the recent review articles (e.g., GLEITER [1989], BIRRINGER [1989], SURYANARAYANA and FROES [1992], SIEGEL [1993], SHULL [1993]), GLEITER [1995].

5.4.2. Generation of nanocrystalline materials

In principle the following three routes have been used so far to generate nanocrystalline materials. The first one starts from a noncrystalline structure, e.g., a glass. The nanocrystalline materials are obtained by nucleating numerous crystallites in the glass e.g., by annealing. These nuclei subsequently grow together and result in a nanocrystalline material. The various modifications of this approach differ primarily in the starting material used. So far metallic glasses (e.g., produced by melt spinning, LU *et al.* [1991]) and the sol-gel technique (CHAKRAVORTY [1992]) have been successfully applied. The most important advantages of this approach are as follows. Low-cost mass production is possible and the material obtained exhibits little or no porosity. Obviously this approach is limited to chemical compositions which permit the generation of glasses or sols.

The second route is based on increasing the free energy of a (initially coarse-grained) polycrystal. The various modifications differ by the procedures that are applied to increase the free energy. Ball-milling, high-strain-rate deformation, sliding wear, irradiation with high-energy particles, spark erosion and detonation of solid explosives have been used so far. All of these techniques are based on introducing a high density of lattice defects by means of plastic deformations or local atomic displacements. The crystal size of the final product can be varied by controlling the milling, the deformation, the irradiation or the wear conditions (e.g., the milling speed, temperature, type of mill used, etc.). This group of methods have been scaled up successfully. For example, cryomilling has been applied to produce commercial quantities of nanocrystalline Al/Al_2O_3 alloys.

The third route of production processes for nanocrystalline materials involves a two-step procedure. In the first step, isolated nanometer-sized crystallites are generated which are subsequently consolidated into solid materials. PVD, CVD, electrochemical, hydrothermal, thermolytic, pyrolytic decomposition and precipitation from solution have been used so far. The most widely applied PVD method involves inert gas condensation (fig. 37). Here, the material is evaporated in an inert gas atmosphere (most frequently He at a pressure of about 1 kPa). The evaporated atoms transfer their thermal energy to the (cold) He and hence, condense in the form of small crystals in the region above the vapor source. These crystals are transported by thermal convection to the surface of a cold finger. In addition to thermal evaporation, dc or ac sputtering as well as laser

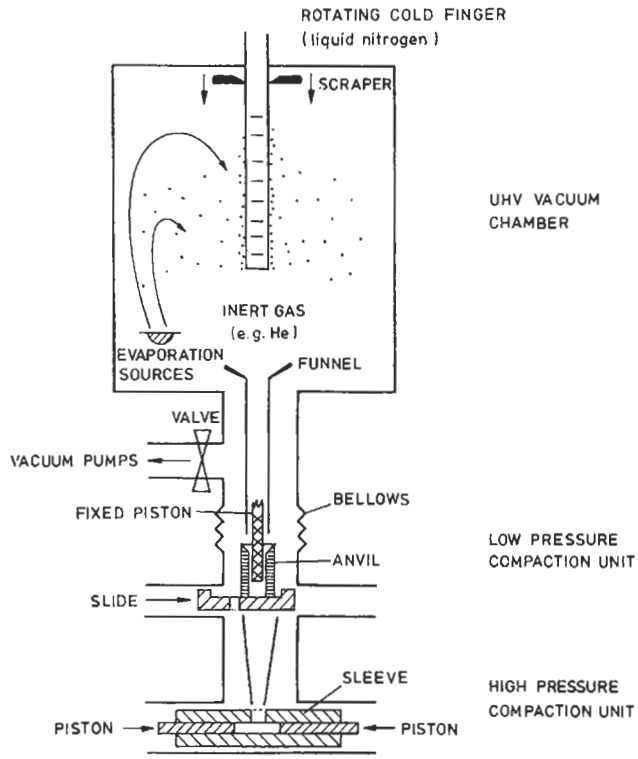

Fig. 37. Schematic drawing of gas-condensation chamber for the synthesis of nano-crystalline materials. The material evaporated condenses in the inert gas in the form of small crystallites which are subsequently transported via convection (arrows) to the liquid-nitroqen-filled cold finger. The powder of crystallites is finally scraped from the cold finger, collected via the funnel and consolidated first in the low-pressure compaction device and then in the high-pressure compaction unit. Both compaction units are kept under UHV conditions (GLEITER [1989]). Instead of an evaporation device, a sputtering source has been utilized as well.

evaporation or laser ablation have been used. Instead of evaporating the material into an inert gas atmosphere, bulk nanocrystalline materials may also be obtained by depositing the material in the form of a nanometer-sized polycrystalline layer onto a suitable substrate. PVD, CVD and electrochemical deposition has been applied successfully (CHATTERJEE and CHAKRAVORTY [1989], OSMOLA *et al.* [1992], VEITH *et al.* [1991, 1992], HASEEB *et al.* [1993]). In the special case of nanocrystalline Si, plasma-enhanced CVD using an rf or dc plasma source turned out to be a versatile method that permits one to generate thin Si films. Depending on the deposition parameters, any microstructure may be obtained between amorphous Si and coarse-grained crystalline Si (VEPREK and SAROTT [1987]). The methods for generating small crystallites by precipitation reactions may be divided into processes involving precipitation in nanoporous host materials and host-free precipitation. In both cases a wide range of solvents (e.g., water, alcohol, etc.) as well as different reactions (e.g., addition of complex forming ions,

photochemical processes, hydrolytic reaction, etc.) have been utilized. A widely applied method for generating nanometer-sized composits is based on the sol-gel process. An interesting subgroup of sol-gel generated nanocomposits are organic-inorganic nanoscale ceramics, so called *ceramers, polycerms* or *ormocers* (SCHMIDT [1992]). Following the ideas of Mark and Wilkes, (GARRIDO *et al.* [1990]), these materials are prepared by dissolving preformed polymers in sol-gel precursor solutions, and then allowing the tetraalkyl orthosilicates to hydrolyze and condense to form glassy SiO_2 phases of different morphological structures. Alternatively, both the organic and inorganic phases can be simultaneously generated through the synchronous polymerization of the organic monomer and the sol-gel precursors. Depending upon such factors as the structures of the organic and inorganic components, the phase morphologies, the degree of interpenetration, and the presence of covalent bonds between the phases, the properties of these composites can vary greatly and range from elastomeric rubbers to high-modulus materials.

Precipitation in nanoporous materials involves a large spectrum of host substances. Hosts providing a three-dimensional framework containing nanometer-sized pores include zeolites, microemulsions, organogels (microemulsions containing gelatin), porous glasses, protein cages, micelles, capped materials. Graphite tubes, urea channels, phosphazene tunnel, lipid bilayer vesicles are examples of one-dimensional tunnel hosts. Layered (two-dimensional) hosts are provided by clays, graphite, halide layers and self-assembled mono- or multilayers. For a recent review of the fascinating developments in these areas we refer to the paper by OZIN [1992]. One of the attractive features of such nanosized *confined precipitates* is that they allow one to produce bulk quantities of unagglomerated nanoparticles.

During the second step of the third production method, the loose powder of nanometer-sized crystals is consolidated into a bulk material. Consolidation of the small crystals has been performed at low as well as elevated temperatures under static (e.g., uniaxial pressure, hydrostatic pressure, laser-sintering, laser reactive sintering) or dynamic conditions (e.g., sinter-forging, shear, explosive consolidation). Laser reactive sintering is applicable preferentially to nanocomposits. The strategy of this method is to select mixtures (e.g., a nanocrystalline ceramic and a metal) so that one component has a significantly lower melting point than the other(s). The objective is to achieve enhanced sintering from the low-melting component during pulse heating by a laser beam that is scanned over the pre-consolidated material (MANTHIRAM *et al.* [1993]). In consolidating/sintering nanocrystalline powders it is noticed that the nanometer-sized powders densify at much lower temperatures (lower pressures) than coarse grained powders with the same chemical composition.

In comparison to the first two methods described at the beginning of section 5.4.2, the main advantages of producing nanocrystalline materials by a two-step procedure (involving the generation of isolated nanometer-sized crystals followed by a consolidation process) are as follows: (i) Crystals with different chemical compositions can be co-generated, leading to "alloying" on a nanometer-scale. (ii) The free surfaces of the small crystals may be coated prior to the compaction process by evaporation, sputtering, chemical reaction (e.g., surface oxidation) or in suspension. (iii) The interior of the crystallites may be modified by ion implantation before consolidation. Due to the small

crystal size, the implantation results in materials that have the same chemical composition throughout the volume. In bulk materials, ion implantation is limited to surface regions.

Due to the high density of interfaces, single-component nanostructured materials frequently exhibit crystal growth during sintering. One approach to minimise crystal growth is to limit the time spent at the consolidation temperature. This may be achieved by sinter-forging or explosive consolidation. Another approach is to use grain growth inhibitors such as pores, second phase particles, etc. (MAYO and HAGUE [1993]). The latter method has been utilized, for instance, to sinter nanostructured WC alloys (cf. § 5.7.1). Grain growth was inhibited by transition metal carbides.

5.4.3. Atomic structure

The hypothesized reduced density in the cores of the grain boundaries in nanocrystalline materials (cf. fig. 36) agrees with the following observations. In comparison to a single crystal of the same chemical composition, nanocrystalline materials exhibit: (i) A reduced bulk density and a reduced Debye temperature; (ii) a positron lifetime spectrum that indicates the presence of interfacial free volume which varies locally in size from a single vacancy to about eight vacancies (WÜRSCHUM *et al.* [1993]); (iii) an enhanced small-angle X-ray and/or neutron diffraction cross-section; (iv) an enhanced specific heat; (v) a modified isomer shift in the Mössbauer spectrum; (vi) a hyperfine field distribution that differs from that of the crystalline state; (vii) an enhanced solute diffusivity and substitutional solute solubility; (viii) an enhanced compressibility of the boundary regions and (ix) the observation of quantum size-effects in nanocrystalline semiconductors (e.g., in nanocrystalline ZnO) which indicates that the boundary regions act as barriers for electron propagation.

In addition to these findings, high-resolution electron microscopy, wide-angle X-ray or neutron diffraction measurements and computer simulations of the structure of individual grain boundaries (in bicrystals) indicate a boundary core density that is in the order of 75% to 90% of the corresponding crystal density (cf. fig. 35). Depending on the method used to study the grain-boundary structure, core widths between about 0.5 and several nanometers were measured. The boundary core densities and widths in bicrystals seem comparable with the boundary-core densities in nanocrystalline materials deduced from the data of the various measurements listed above. However, at this point it should be noted that the structure of the grain boundaries in nanocrystalline materials may be expected to differ from the one in bicrystals if the crystal size is reduced to a few nanometers. If the crystal size approaches a few nanometers, the lengths of the boundary segments between adjacent triple junctions are just a few interatomic spacings. In other words, the boundary lengths are shorter than the boundary periodicity. This is not the case for boundaries in macroscopic bicrystals. Moreover, the elastic interaction between neighboring boundaries (spaced a few nanometers only) may result in significant structural changes of the atomic arrangements in the boundary cores. The significance of both effects has been demonstrated recently by means of computations based on elasticity theory and computer simulations (KING [1993], HAHN [1994]). Computer simulations of the boundary structure indicate that the atomic arrangements in the boundary cores

References: p. 935.

change significantly, if the boundary lengths and spacings between adjacent boundaries approach the periodicity of the atomic structure of the boundaries. In fact, experimental evidence suggesting a different boundary structure in bicrystals and nanocrystalline materials has been reported. For example, the grain-boundary free volume (measured by positron lifetime spectroscopy, fig. 38a) and the specific electric resistivity per unit area of the boundaries of nanocrystalline materials was noticed to vary as a function of the crystal size (TONG *et al.* [1992]). The crystal size dependence suggest that the atomic structure of the grain boundaries depends on the lateral dimensions of the grain boundaries and on the spacings between neighbouring boundaries. This result agrees with recent theoretical studies of grain boundaries of finite extent (GERTSMAN *et al.* [1989]). These studies suggest that boundaries of finite extent differ from infinite boundaries primarily due to the disclinations formed at the triple junction between these boundaries. As the crystal size decreases, these disclinations become more and more important for the boundary structure. Another explanation for the experimentally observed grain size dependence has been proposed by PALUMBO *et al.* [1991b]. They pointed out that the volume fraction of the triple junctions between three boundaries in a nanocrystalline material becomes equal or larger, than the volume fraction of the planar boundary segments, if the crystal size is reduced below about 5 nm. If the atomic structure of the triple junctions differs from that of the boundaries, a grain size dependence will be noticed. Experimental evidence supporting this view by means of hydrogen diffusion in nanocrystalline Ni has been presented (PALUMBO *et al.* [1991b]). A correlation between the atomic structure of the boundaries and the preparation procedure has been evidenced by positron lifetime as well as Mössbauer spectroscopy. Nanocrystalline iron was produced by ball-milling and inert-gas condensation. Although both materials had the same chemical composition and comparable crystal size, they exhibited different hyperfine parameters i.e., different atomic structures. Similar results were obtained by means of positron annihilation measurements for nanocrystalline Cu or Ni in comparison to nanocrystalline metals produced by crystallizing metallic glasses.

The expected modified *number of nearest neighbor atoms* and the *broad distribution of interatomic spacings in the boundary cores* agree with computer simulations of the structure of grain boundaries, with the results of measurements by means of wide angle X-ray diffraction, EXAFS and the enhanced width of the distribution of the quadruple splitting in the Mössbauer spectrum of a nanocrystalline material in comparison to single crystals with the same chemical composition (LOEFFLER *et al.* [1995]). A discussion of the various measurements mentioned in this paragraph and the relevant original publications may be found in recent review articles listed at the end of § 5.4.1.

Ample evidence for *size effects and effects resulting from a reduced dimensionality* has been reported for nanocomposits and will, hence, be discussed in paragraph 5.6. In single component nanocrystalline materials only rather few observations of this kind seems to be available up to now. Figure 38b shows the blue shift of nanocrystalline (consolidated) ZnO resulting from quantum size effects. Apparently the grain boundaries act as potential barriers separating the individual crystals electronically. Size and/or dimensionality effects have been noticed by positron lifetime measurements as a function of the grain size. With decreasing grain size, the free volume in the interfaces becomes larger (fig. 38a) (TONG *et al.* [1992]).

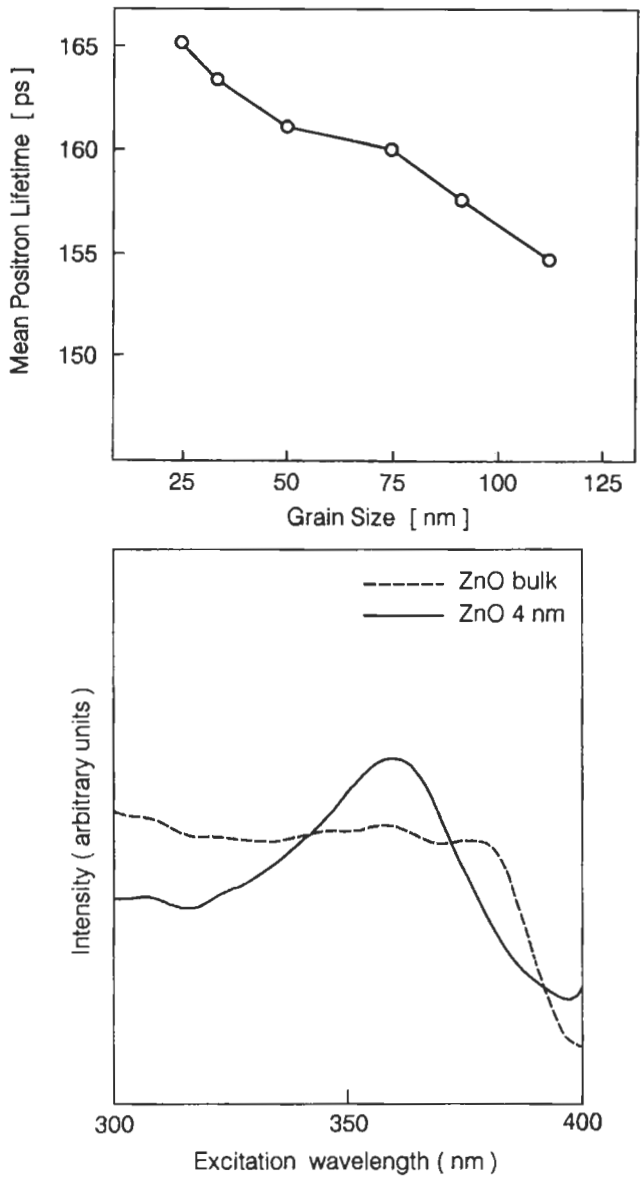

Fig. 38. (a) Variation of the mean positron lifetime as a function of the grain size in nanocrystalline $Fe_{78}B_{13}Si_9$ (TONG *et al.* [1992]). With decreasing grain size (at constanct chemical composition) the lifetime increases, indicating that the size of the sites of enhanced free volume in the grain boundaries changes as a function of grain size. (b) Photoluminescence spectrum of bulk (crystalline) ZnO in comparison to the (blue-shifted) spectrum of nanocrystalline ZnO (crystal size 4 nm). The detection wavelength used was 550 nm. The nanocrystalline ZnO was generated by inert-gas sublimation. The resulting crystallites were consolidated at 0.9 GPa pressure (MCMAHON [1994]).

References: p. 935.

The presently available experimental observations indicate that the structural model outlined so far (cf. fig. 36) is oversimplified in several ways. The atomic structure in the boundary cores (e.g., the average density, coordination number, etc.) depends not only on the crystal size and chemical composition. It also depends on the type of chemical bonding, the presence of impurities, the preparation mode and the time–temperature history of the specimens. For example, Mössbauer spectroscopy reveals that nanocrystalline Fe specimens prepared by ball milling or inert gas condensation exhibit different atomic structures in the boundary regions although the grain sizes and chemical compositions are comparable. The same applies to the structure of the boundary regions with and without impurity atoms. For instance, nanocrystalline Fe containing about 1% oxygen in the boundaries was noticed (by X-ray diffraction) to exhibit a different grain-boundary structure from the same material without or with less oxygen. The effect of the production procedure on the structure and properties of nanocrystalline materials, generated by electroplating and other techniques, has been discussed by ERB *et al.* [1993]. Some of the differences revealed were attributed to the residual porosity. However also pore-free, high-purity nanocrystalline materials (e.g., prepared by rapid shear and electroplating) exhibit properties that differ significantly from those of bulk materials. The deviations were found to depend primarily on the grain size and the preparation procedure (BAKONYI *et al.* [1993]). This result agrees with the basic concepts of nanocrystalline materials discussed in section 5.4.1 and suggests that the details of the atomic arrangement in the boundaries depend (for a given chemical composition) primarily on the grain size, the preparation procedure and the time–temperature history of the material. The significance of the type of chemical bonding for the structure of nanocrystalline materials was recently demonstrated for nanocrystalline diamond. Studies by means of Raman spectroscopy revealed a mixture of sp^2 and sp^3 bonds in nanocrystalline diamond. The sp^2 (graphite like) bonds seem to be associated with the boundary regions. The crystalline regions exhibited pure (diamond-like) sp^3 bonds. A change of the type of chemical bonding does not seem to occur in systems with non-directional bonds such as in metals. In all metallic systems studied so far, the chemical bonding in single-crystalline and nanocrystalline materials seems to remain metallic. Nevertheless, the reduced atomic density, electron density and the modified nearest-neighbor structure in the boundary regions seem to change the interatomic interaction. This is evidenced by the variation of the ferromagnetic properties of the boundary regions in comparisons to the interior of the crystallites (e.g., in Fe, Ni and Gd). Several other measurements (e.g., by X-ray diffraction, positron lifetime spectroscopy, EPR-spectroscopy, Raman spectroscopy, IR-spectroscopy, the diffusivity, the thermal expansion or the the excess energy stored in nanocrystalline materials), support the results discussed so far. In other words, nanocrystalline materials are not fully characterized in terms of their chemical composition and grain size. Depending on the preparation procedure or the time–temperature history, the atomic arrangements in the interfaces, and hence the properties of nanocrystalline materials vary significantly even if the chemical composition and grain size are identical. In certain nanocrystalline ionic materials (e.g., AgCl, AgBr, TlCl, LiI, β-AgI) space charge effects (MAIER *et al.* [1988]) are expected to play an important role in addition to the grain-boundary core effects discussed so far.

If the crystal size becomes comparable to the Debye length of the space charge region at the boundaries, the electric conductance was observed to be dominated by the electric conductivity of space charge region.

5.5. Nanoglasses

The considerations so far were limited to arrays of nanometer-sized crystallites (fig. 36). However, arguments similar to the ones advanced in § 5.4.1, apply to so-called *nanoglasses* as well. Nanoglasses are solids that are generated by consolidating nanometer-sized glassy spheres (JING *et al.* [1989]). A two-dimensional model of the resulting structure is displayed in fig. 39. The similarity between a nanostructured material composed of nanometer-sized crystallites and nanometer-sized glassy spheres may be apparent. In fact, the nanoglass may be considered as consisting of glassy regions (represented by full circles in fig. 39) joined together by a network of "interfaces" that are represented by open circles. The interfaces are created when the originally free surfaces of the glassy spheres are "welded" together during consolidation. Just as in the case when two crystals of different crystallographic orientations are joined together during consolidation, a region of reduced density and modified nearest-neighbor coordination may be expected to result in the regions where the glassy spheres are joined together. If this is so, a close analogy may be expected to exist between the microstructure of nanocrystalline materials and of nanoglasses. As a matter of fact, such an analogy has been suggested on the basis of studies by Mössbauer spectroscopy

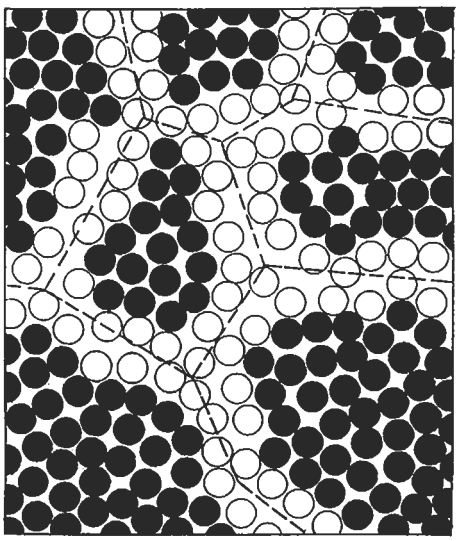

Fig. 39. Schematic (hard-sphere) model of the atomic structure of a nanoglass. The nanoglass is assumed to be generated by consolidating nanometer-sized glassy spheres. The atoms in the interior of the glassy spheres are represented by full circles. The atoms in the interfacial regions between adjacent spheres are drawn as open circles. Both types of atoms are assumed to be chemically identical (GLEITER [1992]).

References: p. 935.

(fig. 40). The quadrupole splitting distribution* of nanocrystalline materials indicates that these materials consist of two components (fig. 40b): The crystalline component and the interfacial one. The crystalline component is characterized by a narrow quadrupole splitting distribution (fig. 40a), whereas the distribution of the interfacial component (fig. 40b) extends over a wide range along the horizontal (QS) axis. By analogy to the

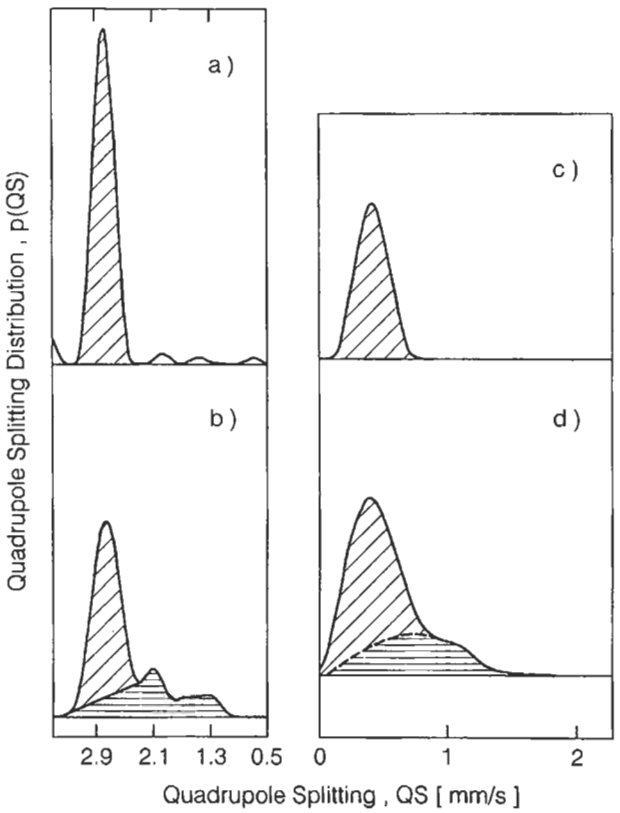

Fig. 40. Comparison of the quadrupole splitting distribution of a single crystal FeF_2 (fig. 40a) and of nanocrystalline FeF_2 (fig. 40b). Right side: Comparison of the quadrupole splitting distribution of a $Pd_{70}Si_{27}Fe_3$ metallic glass produced by melt-spinning (fig. 40c) and in the form of a nanoglass (fig. 40d) produced by consolidating 4 nm-sized glassy spheres. Both glasses had the same chemical composition. The interfacial components in the Mössbauer spectra of the nanocrystalline and nanoglassy materials are the areas hatched horizontally (JING *et al.* [1989]).

* The quadrupole splitting distributions shown in fig. 40 are essentially plots that display the probability, p(QS), that a particular atom is surrounded by nearest neighbors forming arrangements of different degrees of asymmetry. Atoms surrounded by symmetrically arranged nearest neighbors appear on the left side of the QS axis (horizontal axis in fig. 40). The Mössbauer signals of atoms in asymmetric environments appear on the right side of the QS axis.

spectrum of the nanocrystalline material, tbe quadrupole splitting distribution of a nanoglass was found to exhibit the same features (fig. 40d): It consists of a (narrow) glassy (fig. 40c) and an (wide) interfacial component (fig. 40d) as might be expected on the basis of the model suggested (fig. 39).

5.6. Nanocomposites

Nanocomposites are compositionally modulated nanostructured materials. Basically the following three types of microstructures have been revealed experimentally in the case of cluster-assembled materials. (Compositionally modulated layer structures have been treated in section 5.2).

5.6.1. Nanocomposites made up of crystallites with different chemical compositions

Figure 41a displays schematically the expected atomic structure of this kind of a nanocomposite. Examples of real nanocomposites of this type are Fe–Ag nanometer-sized alloys. Although Fe and Ag are immiscible in the crystalline and liquid state, the formation of solid solutions (probably in the interphase boundary regions) was noticed in Fe–Ag nanocomposites. The proposed structure of nanocrystalline Fe–Ag nanocomposites deduced from Mössbauer spectroscopy and X-ray diffraction is shown in fig. 41b. Similar alloying effects were reported for many other nanometer-sized composites produced by one of the methods discussed in section 5.4.2 (cf. SHINGU *et al.* [1989], RADLINSKI and CALKA [1991], OEHRING and BORMANN [1991], MURTY *et al.* [1993]). The formation of metastable nanocrystalline solid solutions and/or amorphous phases during the production process, e.g., by ball-milling seem to depend primarily on the free energy of the phases. A large free energy difference relative to the amorphous phase favors the nanocrystalline structure. Nanocrystalline metastable solid solutions seem to result if these phases have a higher stability than the amorphous phase, as was demonstrated for Nb–Al (OEHRING and BORMANN [1991]). The significance of the interfacial structure between chemically dissimilar and immiscible materials was also emphasized by the results of thermodynamic studies (TURNBULL *et al.* [1990]). A reduction of the melting point and the melting enthalpy of finely dispersed Ge particles in a Sn or Pb matrix was interpreted in terms of a disordered interphase boundary structure between both materials. Remarkable reductions or exchange reactions in the solid state at the interfaces between chemically dissimilar components in nanometer sized materials, e.g., metals and sulfides or oxides have been reported during ball-milling or heavy mechanical deformation (*mechanochemical reactions*). The existing evidence indicates that the newly formed interfaces during milling play a crucial role. The reactivity of newly formed solid/solid interfaces has been demonstrated about two decades ago by co-extruding different materials, e.g., mixtures of metallic and ceramic powders or mixtures of metallic and polymer powders (e.g., Al/Al_2O_3, Al/NaCl or Al/Teflon) (FROMMEYER and WASSERMANN [1976]). In all cases studied, the adhesion between the highly extruded components at the newly formed interphase boundaries was much stronger than the cohesion at interphase boundaries formed during conventional sintering. In order to explain the reactions and/or adhesion, the formation of free radicals,

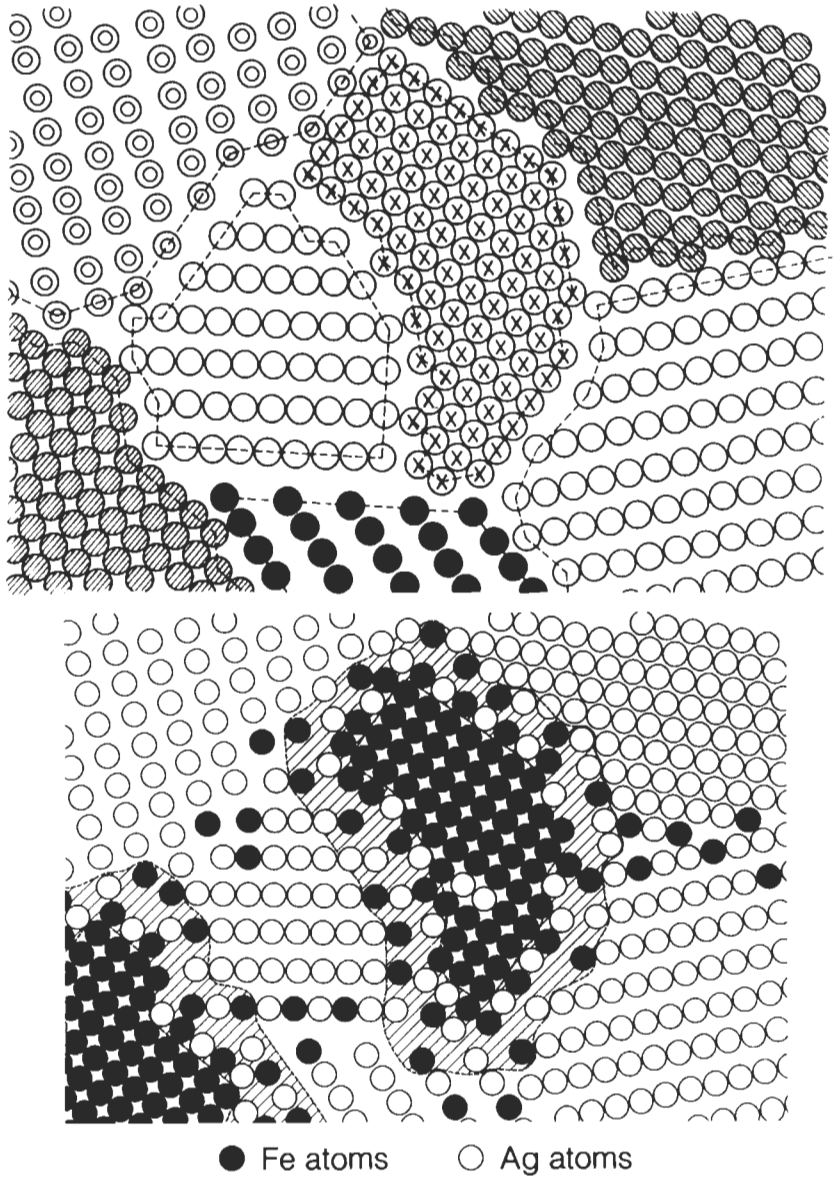

Fig. 41. (a) Schematic (hard sphere) model of a nanocomposite consisting of crystals with different chemical compositions. The chemically different atoms are represented by different symbols (open, closed etc. circles). (b) Schematic model of a nanocrystalline Ag–Fe alloy deduced from Mössbauer spectroscopy. The alloy consisting of a mixture of nanometer-sized Ag and Fe crystals. In the (strained) interfacial regions between Ag and Fe crystals, solid solutions of Fe atoms in Ag, and Ag atoms in Fe are formed although both components are insoluble in the liquid as well as in the solid state. Similar effects may occur in grain boundaries between adjacent Fe and Ag crystals (HERR *et al.* [1990]).

deformed chemical bonds, ions and free electrons at the interfaces has been suggested. Reactions having positive enthalpies or even positive free energies are shown to occur. In fact, mechanochemical reactions seem to open new ways for processing, mining or generating materials avoiding high temperature reactions (CALKA [1993]). Nanocomposites consisting of metallic crystallites embedded in an insulating matrix exhibit interesting electrical properties such as quantum size effects (HENGLEIN [1988], HALPERIN [1986]), large dielectric permittivities as well as ac and dc resistivities. For example, the conductivity of the metallic particles embedded in an insulating matrix has been reported to decrease by several orders of magnitude if the particle size is reduced into the nanometer regime (Size Induced Metal Insulator Transition, MARQUARDT *et al.* [1988]). The physical interpretations of this "SIMIT" effect is still a matter of controversy. Quantum size effects as well as a statistical approach of free electrons in small metallic particles based on a modified Drude model have been proposed.

5.6.2. Nanocomposites made up of crystallites and glassy components with different chemical compositions

An interesting example of this type of nanocomposites are nanometer-sized metallic or semiconductor particles (e.g., Ag, CdS or CdSe) embedded in an amorphous dielectric matrix (e.g., SiO_2) (fig. 42). If the embedded particles are metallic, the plasmon resonance of the particles is broadened (relative to the bulk material) by more than a factor 3. According to Mie's theory, this broadening results from chemical interfacial effects between the metallic clusters and the (dielectric) matrix. Electron mean free path and quantum size effects seem to be of limited significance in the metallic systems studied so far (HÖVEL *et al.* [1993]. This is not so for semiconductor particles. They are found to exhibit quantum size effects (blue-shifted band gap, discrete molecule-like excited electronic states, appearance of interface states in the band gap causing fast non-radiative recombinations, or luminescence with a large Stokes shift). If one encapsulates the embedded nanocrystals in a high-band-gap insulator, then resonances occur at very high energies. The nanocrystalline HOMO and LUMO states remain as confined bulk eigenstates inside the insulator shell. This is the ideal quantum dot case, where surface states are not important in luminescence. For example, CdS has been encapsulated inside a monolayer of $Cd(OH)_2$, CdSe inside ZnS, Si inside SiO_2, etc. More complex structures have recently been made: a three layer "quantum dot quantum well" involving a monolayer of HgS grown on a CdS core and capped with four monolayers of CdS, shows luminescence from the HgS shell monolayer. The conceivable possibilities for generating new optical materials in this way are vast: experimental progress depends critically upon the development of advanced synthetis methods for high-quality materials with closely specified dimensional tolerances.

5.6.3. Nanocomposites with intercalated (doped) grain boundaries

The thickness of the intercalate layers in the cores of the boundaries may vary from less than a monolayer to multilayers. In the case of thin intercalates (less than a monolayer), the atoms of the intercalate seem to enter specific, low energy sites. For example Bi atoms that are incorporated in the boundaries of nanocrystalline Cu, were

References: p. 935.

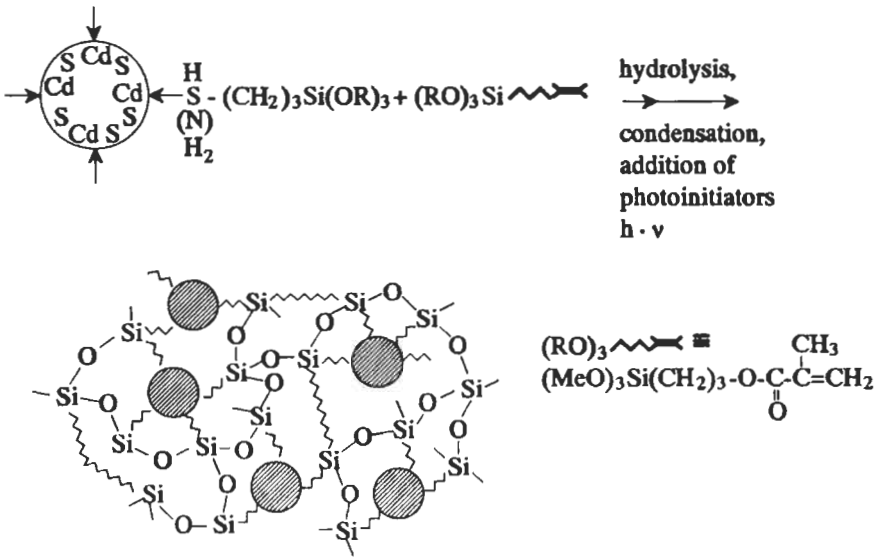

Fig. 42. Reaction and structural model of the incorporation of ligand stabilized CdS quantum dots into ormocer matrices (SCHMIDT [1992]).

found by EXAFS studies (HAUBOLD [1993]) to enter sites that are characterized by three Cu atoms surrounding every Bi atom (fig. 43a). Multilayer intercalate boundary structures (fig. 43b) are apparently less well ordered. For example the structure of Ga in nanocomposites consisting of nanometer-sized W crystals separated by several layers of Ga was found (by PAC measurements) to exhibit a disordered structure. A special case of this type of nanocomposite structures are soft ferromagnetic nanostructured materials generated by partial crystallization of certain metallic glasses (cf. section 5.7.3). Another way in which nanocomposites with doped grain boundaries may be formed has been discussed by TANAKOV *et al.* [1991]. The energy stored in the stress field in the vicinity of grain boundaries may be reduced by a spacial redistribution of the solute atoms. This effect was proposed first by Cottrell for the redistribution of solute atoms in the stress field of a dislocation (Cottrell cloud). Under suitable conditions, the stress-induced solute redistribution in the vicinity of grain boundaries may lead to nanocomposites with solute-enhanced boundary regions. Stress-induced solute segregation to the boundaries may be important for the stability of nanostructured materials against grain growth. Stability against grain growth may be expected if the reduction of the strain energy by removing a solute atom from the lattice of the crystallites is equal or larger than the energy required to bring the solute atom into the boundary core. A potential model system of this kind are nanocrystalline Y-Fe solid solutions. Indeed, little grain growth was noticed in Fe-rich nanocrystalline Y-Fe alloys (WEISMÜLLER *et al.* [1992]). (See also ch. 28, § 4.3).

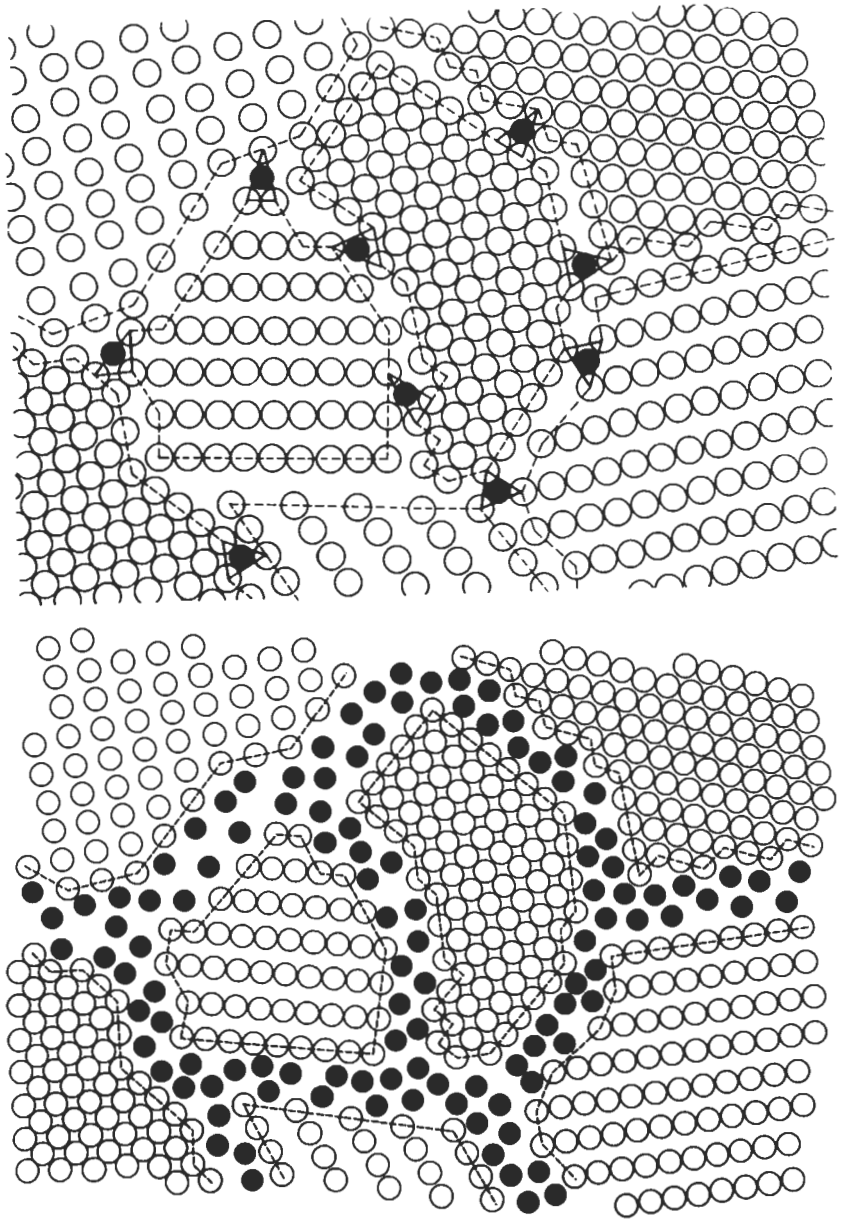

Fig. 43. Two-dimensional model of the atomic structure of a (doped) grain-boundary alloy. The doping atoms (full circles) are confined to the boundary core regions between the nanometer-sized crystals (open circles). In the case of grain boundaries with less than a monolayer of doping atoms (fig. 43a, e.g., Bi in nanocrystalline Cu) the doping atoms occupy specific sites of low energy. If the doping concentration is increased, intercalate structures may result that are more than one monolayer thick, (fig. 43b, e.g., Ga in nanocrystalline W).

References: p. 935.

5.7. Technological applications

Although nanocrystalline materials were proposed just about 15 years ago (MARQUARDT and GLEITER [1980], GLEITER [1981b]), a few technological applications have already emerged.

5.7.1. Hard, wear-resistant nanocrystalline WC–Co materials

Nanostructured WC–Co materials have been commercially generated and are presently applied as protective coatings and cutting tools. Both applications utilize the enhanced hardness, wear resistance and toughness of the nanostructured WC–Co in comparison to the conventional, coarser-grained materials of this kind. As may be seen from figs. 44 and 45, the replacement of coarse-grained WC–Co by nanostructured WC–Co alloys improves the mechanical properties by up to one order of magnitude. This improvement does not seem to be the upper conceivable limit because these new materials are not yet optimized in any way. The nanostructured WC–Co was produced on an industrial scale either by high energy milling (SCHLUMP and WILLBRAND [1992]) or by chemical processing (MCCANDLISH *et al.* [1990]). Chemical processing involves three coordinated steps: preparation and mixing of starting solutions; spray-drying to form chemically homogeneous precursor powders; and, finally, fluid-bed thermochemical conversion of the precursor powders to nanocrystalline WC–Co powders. Both spray-drying and fluid-bed conversion are proven scalable technologies that have been used for producing bulk quantities of cemented carbide powders (KEAR and MCCANDLISH [1993]).

5.7.2. Near net shape forming of nanocrystalline ceramics/intermetallics

The small crystal size of nanocrystalline ceramics suggests that superplastic deformation can occur in these materials at temperatures as low as ambient. This idea (KARCH and BIRRINGER [1990]) has been recently tested for various ceramics as well as metallic nanometer-sized materials. In some of the fine-grained materials, large deformations (100% to > 1000%) were obtained at strain rates in the order of 1/s (e.g., HIGASHI [1993]). Failure occured in ceramic nanocrystalline material preferentially by nucleation, growth and interlinkage of cavities if the specimens were deformed in tension. Superplastic deformation of nanocrystalline materials may be utilized for near net shape forming of brittle materials such as ceramics or intermetallics. Figure 46 reveals the replication of a surface step by low temperature plastic deformation of nanostructured TiO_2. A control experiment was performed with polycrystalline TiO_2 (50 pm grain size) under the same conditions (KARCH and BIRRINGER [1990]). The polycrystalline TiO_2 showed no measurable plastic deformation. The plasticity of nanostructured materials has also been suggested to improve the mechanical properties of non-oxide ceramics such as Si_3N_4 or SiC. These materials exhibit poor high-temperature mechanical properties owing to crack growth and boundary embrittlement which prevent their application in gas-turbines and aerospace technology. Many attempts have been made to solve this problem e.g., by incorporating second-phase particles, platelets or whiskers. The success achieved has been very limited. Hence, it attracted attention when striking improvements were recently reported upon preparing these ceramics in the form of nanocomposites (NIIHARA [1991]).

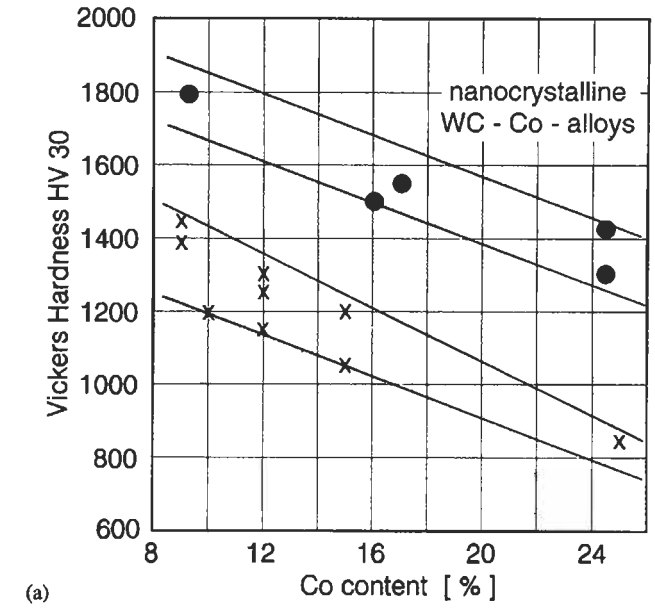

(a)

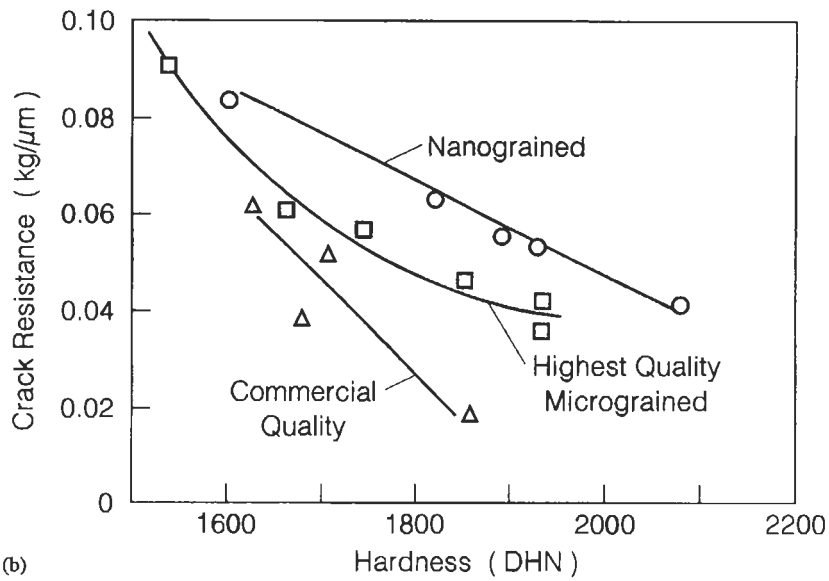

(b)

Fig. 44. (a) Comparison of the Vickers hardness of commercial (crossed lower lines) and nano-crystalline WC–Co alloys (circles, upper lines) as a function of the Co content (SCHLUMP and WILLBRANDT [1992]). (b) Comparison of the crack resistance of nanocrystalline and commercial grades of fully sintered WC–Co materials (KEAR and MCCANDLISH [1993]). In physical terms, the crack resistance measures the mechanical energy required to displace the crack tip by one μm. In other words, the tougher the material the higher is its crack resistance.

References: p. 935.

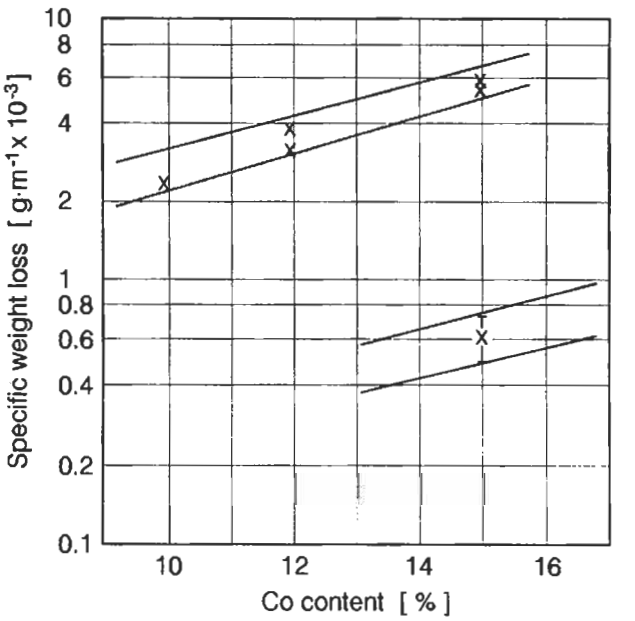

Fig. 45. Comparisons of the measured wear rate (under identical wear conditions) of conventional (upper lines) and nanocrystalline WC–Co alloys as function of the Co content (SCHLUMP and WILLBRAND [1992]). The wear rate was measured by means of the rate of weight loss of the specimens during the wear experiment.

5.7.3. Soft ferromagnetic nanostructured materials ("Finemet")

Partial crystallization of certain metallic glasses with the composition $Fe_{73.5}Si_{13.5}B_9Cu_1Nb_3$ leads to nanometer-sized Fe–Si (B) crystallites (5 to 20 nm diameter) embedded in a residual glassy matrix (YOSHIZAWA *et al.* [1988]). The dopants (Cu, Nb) are found to be accumulated in the non-crystalline regions left between crystallites. The small crystal size is achieved by enhancing the nucleation rate of the crystallites dramatically. In fact, the numerous clusters of Cu atoms formed in the glassy matrix act as nucleation sites. Studies of the magnetic properties of these materials revealed high ($\sim 10^5$) initial permeabilities, low ($\sim 10^{-2}$ A/cm) coercitivities, high saturation induction (up to 1.7 T) combined with a low mean magnetostriction ($\sim 10^{-6}$). These properties are comparable or better than the best values achieved with (the more expensive) permalloys and cobalt-based amorphous magnetic alloys. The attractive magnetic properties of these "Finemet" materials are believed to result from a small mean anisotropy together with a drastically reduced mean magnetostriction and an enhanced saturation magnetization of the crystallites. The small anisotropy is explained in terms of the fact that the magnetic exchange length is larger than the grain size. Therefore, the domain wall width exceeds the size of the grains.

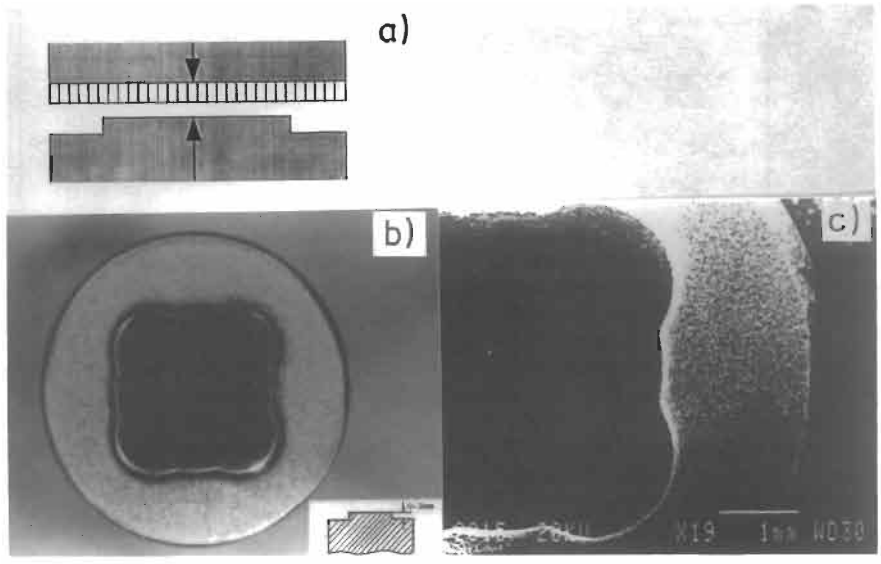

Fig. 46. Replication of a surface step by nanocrystalline TiO2. The experimental arrangement used is drawn in fig. 46a. A nanocrystalline TiO2 pellet is compressed between two WC pistons. The free surface of the lower piston contains a surface step (height 0,3 mm). Fig. 46b shows a top view of the piston with the surface step. Fig. 46c displays the TiO2 pellet which replicated the surface step. The deformation was performed at 800° C over 10 min at a pressure of 1 GPA. (KARCH and BIRRINGER [1990])

5.7.4. Magneto-caloric cooling with nanostructured materials

The magnetic properties of nanostructured materials containing nanometer-sized magnetic particles dispersed in a nonmagnetic matrix differ from those of the corresponding bulk magnetic material. These differences affect the magnetocaloric properties of such materials. Upon the application of an external magnetic field, the magnetic spins in a nanostructured material of this kind tend to align with the field, thereby reducing the entropy of the spin system. If this process is performed adiabatically, the specimen's temperature will rise. This effect is called *magneto-caloric heating.* The incremental temperature rise during magneto-caloric heating, dT, is related to the degree of spin alignment and the magnitude of the magnetic spin moment of the individual particles. Creation of a nanostructured material with many small ferromagnetic regions provides an effectively enhanced magnetic moment which can result (in certain temperature and magnetic field ranges) in an increased dT over that provided by either paramagnetic or ferromagnetic materials, with potential application to magnetic refrigeration. It was shown that efficient magnetic refrigerators may then be operated at hiqher temperatures (above 20 K) and require relatively low magnetic fields (< 5 T) in comparison to magneto-caloric cooling with paramagnetic materials. Figure 47 shows an example for the temperature variation (magneto-caloric cooling and heating) of a nanostructured material due to a varying external magnetic field. The details of how the altered magneto-caloric effect is governed by composition and processing has recently been studied in detail by MCMICHAEL *et al.* [1993].

References: p. 935.

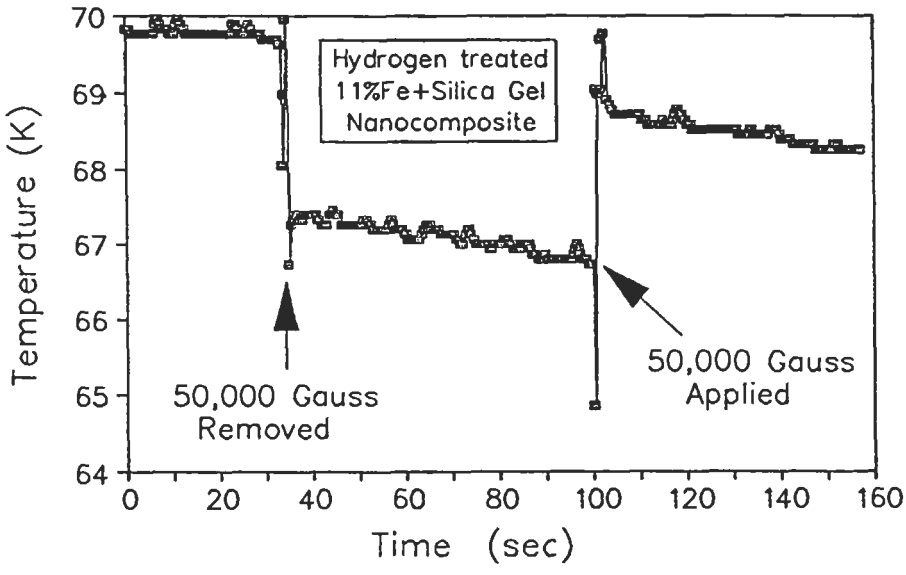

Fig. 47. Temperature vs. time data for a superparamagnetic H_2-treated 11% Fe+silica gel nanocomposite in a 5 Tesla magnetic field. The magnetic field was first removed and then applied to the sample (McMichael *et al.* [1993]).

5.7.5. Nanocrystalline magnetic recording materials

In most video recorders used today, the magnetic material of the record/playback head is usually a crystalline ferrite. These materials are, however, not suitable, when substantially finer details on the magnetic tape are required, e.g., for high-definition television (HDTV) recording. The search for an alternative has resulted in a new type of nanometer-sized magnetic materials: multilayers in which crystalline iron layers of about 10 nm thickness are alternated with even thinner amorphous iron-alloy layers. The chemical composition of the layers used are Fe/FeCrB, NiFe/FeC, FeAl/SiN and FeNbSiB/FeNbSiBN. These nanocrystalline materials combine high saturation magnetization with a high permeability in the MHz frequency range, allowing video recording at much increased information densities (De Wit *et al.* [1991]).

5.7.6. Giant magnetoresistance in nanostructured materials

The recent reports of *giant magnetoresistance* (GMR) in a number of antiferromagnetically coupled multnayer systems have stimulated widespread research activity because the effect is of interest for basic research as well as for technological applications in the area of recording and data storage. Modeling of the GMR has emphasized spin-dependent scattering both within the ferromagnetic layers and at the interfacial regions between the ferromagnetic and non-ferromagnetic layers. The GMR phenomenon is different from the conventional magnetoresistance which is due to the effect of magnetic fields acting directly on the conduction electrons or on the scattering impurities. The GMR in multilayered structures comes from the reorientation of the single-domain

magnetic layers. This is the reason why GMR is not usually seen in conventional bulk magnetic materials. GMR was observed first in both antiferromagnetically coupled and uncoupled layer structures, as a consequence of the fact that the relative orientation of the magnetization of successive ferromagnetic layers changes from antiparallel to parallel in an applied external magnetic field. The change in the magnetization of the layers by the external field reduces the scattering of the conduction electrons travelling through these layers and hence leads to a remarkable change of the dc resistivity of the material. This resistivity change is called GMR (BAIBICH *et al.* [1988]). For systems with uncoupled magnetic layers, the orientation of the magnetization is random at the coercive magnetic field (H_c) and there are many magnetic layers which are statistically arranged antiparallel. If these uncoupled layers are replaced by nanometer-sized particles in a non-magnetic matrix, one may also expect GMR as well. This is indeed the case (fig. 48). The data indicate that a GMR effect in annealed Cu–Co samples is associated with the presence of appropriately sized and spaced Co precipitates in the Cu matrix (BERKOWITZ *et al.* [1992].

5.7.7. Luminescence from porous Si

The recent discovery of visible photoluminescence from porous Si has captured considerable attention (CANHAM [1990], LEHMANN and GÖSELE [1991]). Prepared by electrochemical and chemical etching of single-crystal Si wafers in hydrofluoric acid solutions, porous Si consists of a network of pores that can range in size from micrometers down to a few nanometers. The origin of visible luminescence in porous Si is still controversial. Bulk Si, with a bandgap at 1.12 eV, is weakly luminescent in the near-infrared region of the optical spectrum. For porous Si, the luminescence peak energy can range from 1.12 (infrared) to about 2.3 eV (green light), depending on parameters such as dopant concentration and type, current density during etch, duration of etch, and

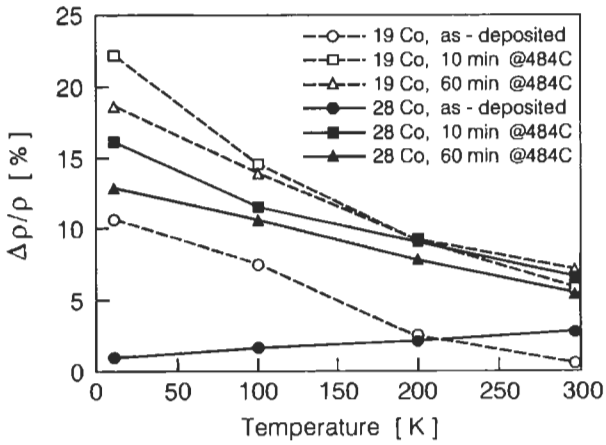

Fig. 48. Temperature dependence of the magnetoresistance ($\Delta\rho/\rho$) for Cu-19 at% and Cu-28 at% Co samples, treated as indicated (BERKOWITZ *et al.* [1992]).

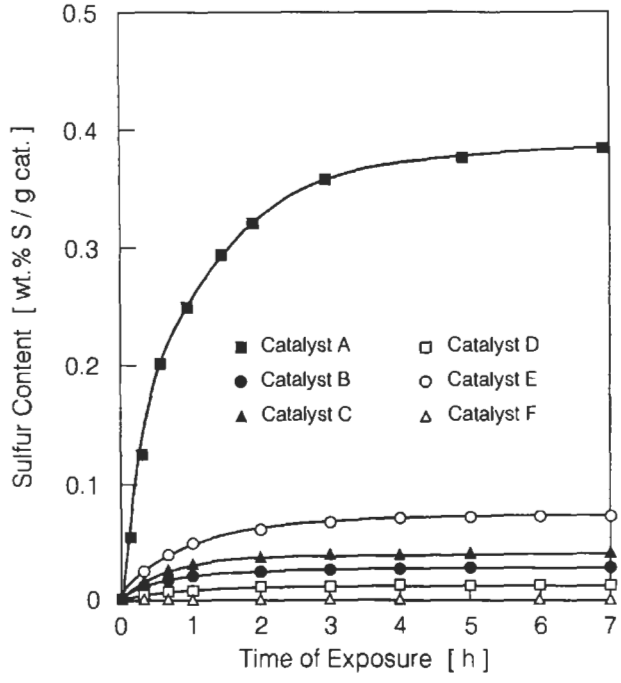

Fig. 49. Activity of nanocrystalline TiO_2 (curve A) for H_2S decomposition as a function of exposure time at 500°C compared with that from several commercial TiO_2 materials and a reference (A: 76 m^2/g nanocrystalline rutile; B: 61 m^2/g anatase; C: 2,4 m^2/g rutile; D: 30 m^2/g anatase; E: 20 m^2/g rutile: F: reference alumina) (BECK and SIEGEL [1992]).

subsequent chemical treatments. These results have been qualitatively explained by invoking size-dependent quantum confinement effects. In fact, transmission electron microscopy (TEM) data support the existence of crystalline Si domains with dimensions small enough (~5 nm) to expect such phenomena. Indeed, recent studies on size-selected, surface-oxidized Si nanocrystals agree well with this idea (WILSON *et al.* [1993]). Another proposed explanation for the luminescence of porous Si is that the electrochemical etch generates surface or bulk chemical species: for example, polysilanes or polysilylenes. Polymers containing only Si and hydrogen are well known as chemicals that can photoluminesce at visible wavelengths. Moreover, siloxene, a chemical which contains Si, oxygen and hydrogen, has emissive properties that are very similar to those of the luminescence of porous Si. Although the current emphasis for utilization of the unique properties of luminescent porous Si is in electroluminescence, other potential applications are beginning to emerge. The high sensitivity of the luminescence to chemical adsorbates, mentioned above, has been found to be readily reversible for a variety of molecules (BAWENDI *et al.* [1992]). This observation may lead to chemical microsensors that are easily incorporated into hybrid Si chips. In addition, photoelectrochemical and ion-irradiation techniques have been developed to allow the resistless

patterning of luminescent porous Si directly onto Si substrates, which may lead to a range of optical display or storage applications (DOAN and SAILOR [1992]).

5.7.8. Catalytic materials

Nanocrystalline cerium oxide, iron carbides and titaniumdioxide have been studied for catalytic applications. The cerium oxide catalysts were generated by inert gas condensation (cf. section 5.4.2), the iron carbides by high-energy milling. Selective catalytic reduction of sulfur dioxide by carbon monoxide on nanocrystalline cerium oxide was investigated in a microreactor, and compared to that of conventional cerium dioxide synthesized by the decomposition of cerium acetate. The nanocrystalline cerium oxide catalyst enabled 100% conversion at 500°C, about 100°C lower than the temperature needed in conventional cerium dioxide catalysts (TSCHOEPE and YING [1994]). The higher activity seems to be related to the oxygen deficiency of the nanocrystalline cerium oxide due to imcomplete oxidation. The nonstoichiometry of the nanocrystalline cerium oxide was confirmed by thermogravimetric analysis and X-ray photoelectron spectroscopy. The iron carbides are found to be active and stable catalysts for CO_2 hydrogenation. The catalytic properties for this reaction appear to be comparable or superior to those of more expensive catalytic materials, such as noble metals dispersed on porous supports. Figure 49 shows the enhanced catalytic activity of nanocrystallite TiO_2 for S removal from H_2S via decomposition compared with commercial (coarser-grained) TiO_2. Obviously, the nanocrystalline sample with a rutile structure was far more reactive than the other ones. Similarly to the enhanced reactivity of nanocrystalline cerium oxide, it was found that the activity of the nanocrystalline TiO_2 results from a combination of features: the high surface area combined with its oxygen deficiency and its rutile structure (BECK and SIEGEL [1992]).

References

AARONSON, H.I., C. LAIRD and K.R. KINSMAN, 1970, Phase Transformations (ASM, Metals Park, Ohio) p. 313.

ABBRUZZESE, G., 1985, Acta Metall. Mater. **33,** 1329.

ABBRUZZESE, G. and K. LÜCKE, 1986, Acta Metall. Mater. **34,** 905.

ABROMEIT, C. and H. WOLLENBERGER, 1988, J. Mat. Res. **3,** 640.

ABROMEIT, C., 1989, J. Modern Phys. **B3,** 1301.

ADAMS, B.L., 1993, Mat. Sci. and Eng. **A166,** 59.

ALLEN, S.M. and J.W. CAHN, 1979, Acta Metall. **27,** 1085.

ANDERSON, A.B., S.P. MEHANDRU and J.L. SMIALEK, 1985, J. Electrochem. Soc. **132,** 1695.

ANDERSON, A.B., C. RAVIMOHAN and S.P. MEHANDRU, 1987, J. Electrochem. Soc. **134,** 1789.

ANDERSON, M.P., D.J. SROLOVITZ, G.S. GREST and P.S. SAHNIG, 1984, Acta Metall. Mater. **32,** 783.

ANTHONY, T.R., 1970, Acta Metall. **18,** 307.

ANTHONY, T.R. and H.E. CLINE, 1973, Acta Metall. **21,** 117.

ANTONIONE, L. BATTEZZATI, A. LUCCI, G. RIONTI and M.C. TABASSO, 1980, J. Mat. Sci. **15,** 1730.

ARANJO, R.D. and S.D. STOOKEY, 1967, Glass Ind. **48,** 687.

ARDELL, A., 1972, Acta Metall. **20,** 601.

ARDELL, A., R.B. NICHOLSON and J.D. ESHELBY, 1966, Acta Metall. **14,** 1295.

ARDELL, A., N. MARDESICH and C. WAGNER, 1979, Acta Metall. **27,** 1261.

ARUNACHALAM, V. S. and R. W. CAHN, 1970, In: Proc. 3rd Bolton Landing Conf., eds. B. Kear, C. Sims and N. S. Stoloff (Claitor's Publ. Div., Baton Rouge, LA) p. 215.
ASHBY, M. F., F. SPAEPEN and S. WILLIAMS, 1978, Acta Metall. **26,** 1647.
AUBAUER, H. P., 1972, Acta Metall. **20,** 165.
AUST, K. T., 1981, Structure and Properties of Grain Boundaries, in: Chalmers Anniversary Volume, Prog. Mater. Sci., eds. J. W. Christian, P. Haasen and T. B. Massalski (Pergamon Press, Oxford) p. 27.
BACKHAUS-RICOULT, M. and H. SCHMALZRIED, 1985, Ber. Bunsengesellsch. Phys. Chem. **89,** 1323.
BACON, R. and FANELLI, 1943, J. Am. Chem. Soc. **65,** 639.
BAIBICH, M. N, J. M. BROTO, A. FERT, F. NGUYEN VAN DAU, F. PETROFF, P. ETIENNE, G. CREUZET, A. FRIEDRICH and J. CHAZELAS, 1988, Phys. Rev. Lett. **61,** 2472.
BAKONYI, I., E. TOTH-KADAR, T. TARNOCI, L. K. VARGA, A. CZIRAKI, I. GEROECS and B. FOGARASSY, 1993, Nanostructured Materials **3,** 155.
BALLUFFI, R. W., 1980, Grain Boundary Structure and Kinetics (ASM, Metals Park, OH).
BARNES, R. S., G. B. REDDINS and A. H. COTTRELL, 1958, Phil. Mag. **3,** 97.
BAWENDI, M. G., P. J. CAROLL, W. L. WILSON and L. E. BRUS, 1992, J. Chem. Phys. **96,** 946.
BECK, D. D. and R. W. SIEGEL, 1992, J. Mat. Res. **7,** 2840.
BECK, P. A., 1954, Phil. Mag. **3,** 245.
BEERÉ, W., 1978, Phil. Mag. **A38,** 691.
BERKOWITZ, A. E., J. R. MITCHELL, M. J. CAREY, A. P. YOUNG, S. ZHANG, F. E. SPADA, F. T, . PARKER, A. HUTTEN and G. THOMAS, 1992, Phys. Rev. Letters **68,** 3745.
BHATTACHARYA, S. K. and K. C. RUSSELL, 1976, Metallurg. Trans **7A,** 453.
BIRKENBEIL, H. J. and R. W. CAHN, 1962, Proc. Phys. Soc. **79,** 831.
BIRRINGER, R., 1989, Mater. Sci and Eng. **A117,** 33.
BISHOP, G. H. and B. CHALMERS, 1968, Scripta Metall. **2,** 133.
BJORKLUND, S., L. DONASHEY and M. HILLERT, 1972, Acta Metall. **20,** 867.
BLEIBERG, M. L. and J. W. BENNET, 1977, in: Radiation Effects in Breeder Reactor Structural Materials (Met. Soc. AIME, Warrendale, PA) p. 211.
BLOECHL, P., G. P. DAS, H. F. FISCHMEISTER and U. SCHOENBERGER, 1990: Metal-Ceramic Interfaces, eds. M. Rühle, A. G. Evans, M. F. Ashby and J. P. Hirth (Pergamon Press, Oxford) p. 2.
BOLLMANN, W., 1970, Crystal Defects and Crystal Interfaces (Springer, Berlin).
BOLLMANN, W., 1974, Phys. Stat. Solidi **21,** 543.
BOYD, A. and R. B. NICHOLSON, 1971, Acta Metall. **19,** 1370.
BRANDON, D. G., B. RALPH, S. RANGANATHAN and M. S. WALD, 1964, Acta Metall. **12,** 813.
BRICKENKAMP, W. and K. LÜCKE, 1983, Ph. D. Thesis RWTH Aachen.
BURGER, M., W. MADER and M. RÜHLE, 1987, Ultramicroscopy **12,** 1.
CAHN, J. W. and J. E. HILLIARD, 1958, J. Chem. Phys. **28,** 258.
CAHN, R. W., 1994, Springer Series in Materials Science **27,** 179, Springer Verlag Berlin.
CALKA, A., 1993, Proceedings of the 122 TMS Annual Meeting and Exhibition, Denver Col., USA, 21-25 February 1993, TMS Commonwealth Drive Warrandale, PA 15086 USA, p. B 63.
CANHAM, L. T., 1990, Appl. Phys. Lett. **57,** 1046.
CAR, R. and M. PARINELLO, 1985, Phys. Rev. Letters **55,** 2471.
CHADDERTON, L. T., E. JOHNSON and T. WOHLENBERG, 1976, Comm. Solid State Phys. **VII, 5,** 105.
CHAKRAVORTY, D., 1992, New Materials, eds. J. K. Joshi, T. Tsuruta, C. N. R. Rao and S. Nagakura, Narosa Publishing House, New Dehli, India, p. 170.
CHALMERS, B. and H. GLEITER, 1971, Phil. Mag. **23,** 1541.
CHATTERJEE, A. and D. CHAKRAVORTY, 1989, J. Phys. D: Appl. Phys. **22,** 1386.
CHANG, R., 1976, Scripta Metall. **10,** 861.
CHEN, H. S. and S. Y. CHANG, 1974, Phys. Stat. Sol. **25,** 581.
CLINE, H., 1971, Acta Metall. **19,** 481.
COOPER, S. P. and J. BILLINGHAM, 1980, Met. Sci. J. **14,** 225.
COTTERILL, R. M. J ., 1979, Phys. Rev. Lett. **42,** 1541.
CULLITY, B. D., 1972, Introduction to Magnetic Materials (Addison-Wesley, London) p. 357 and 565.
DAVIS, C. K., P. NASH and R. STEVENS, 1980a, Acta Metall. **28,** 179.

DAVIS, J.R., T.A. COURTNEY and M.A. PRZYSTUPA, 1980b, Metallurg. Trans. **11A,** 323.
DE FONTAINE, D., 1973, Scripta Metall. **7,** 463.
DELAEY, L. and H. WARLIMONT, 1975, in: Shape Memory Effects in Alloys, ed. J. Perkins, Plenum, New York, p. 89.
DE RANGO, P., M. LEES, P. LEJAY, A. SULPICE, R. TOURNIER, M. INGOLD, P. GERNIE and M. PERNET, 1991, Nature **349,** 770.
DE WIT, H. J, C.H. M WITTMER and F.W.A. DIRNE, 1991, Advanced Materials **3,** 356.
DOAN, V.V. and M.J. SAILOR, 1992, J. Appl. Phys. **60,** 619.
DOHERTY, P.E., D.W. LEE and R.S. DAVIS, 1967, J. Am. Ceram. Soc. **50,** 77.
DOHERTY, R.D., 1982, Met. Sci. J. **16,** 1.
DUFFY, D.M., J.H. HARDING and A.M. STONEHAM, 1992, Acta Metal. Mater. **40,** 11.
EDWARDS, S.F. and M. WARNER, 1979, Phil. Mag. **40,** 257.
EISENBERGER, P. and W.C. MARRA, 1981, Phys. Rev. Lett. **46,** 1081.
ERB, U., W. ABEL and H. GLEITER, 1982, Scripta Metall. **16,** 1317.
ERB, U., A.M. EL-SHERIK, G. PALUMBO and K.T. AUST, 1993, Nanostructured Materials **2,** 383.
ESTRIN, Y. and K. LÜCKE, 1982, Acta Metall. **30,** 983.
EVANS, J.H., 1971, Nature **229,** 403.
FECHT, H.J. and H. GLEITER, 1985, Acta Metall. Mater. **33,** 557.
FERRANTE, M. and R.D. DOHERTY, 1979, Acta Metall. **27,** 1979.
FERRY, D.K., J.R. BAKER and C. JACOBINI, 1990, Granular Nanoelectronics NATO Advanced Study Series, Series B: Physics, Vol. **251.**
FINNIS, M., A.M. STONEHAM and P.W. TASKER, 1990, Metal-Ceramic Interfaces, eds. M. Ruhle, A.G. Evans, M.F. Ashby and J.P. Hirth, Pergamon Press Oxford, p. 35.
FINNIS, M.W. and M. RÜHLE, 1991, Structure of Interfaces in Crystalline Solids, in: Structure of Solids, ed. V. Gerold, Vol. 1 of Materials Science and Technology, eds. R.W. Cahn, P. Haasen and E.J. Kramer (VCH, Weinheim), p. 553.
FINNIS, M., 1992, Acta Metall. Mater. **40,** 25.
FITZSIMMONS, M.R. and S.L. SASS, 1988, Acta Metall. **36,** 3103.
FREEMAN, A.J., C. LI and C.L. FU, 1990, Metal-Ceramic Interfaces, eds. M. Rühle, A.G. Evans, M.F. Ashby and J.P. Hirth, Pergamon Press Oxford, p. 2.
FROMMEYER, G. and G. WASSERMANN, 1976, Zeitschrift für Werkstofftechnik **7,** 129, 136 and 154.
GASTALDI, J. and J. JOURDAN, 1979, Phys. Stat. Sol. (a) **52,** 139.
GAUDIG, W. and H. WARLIMONT, 1969, Z. Metallk. **60,** 488.
GARRIDO, L., J.L. ACKERMANN and J.E. MARK, 1990, Mat. Res. Soc. Sympos. Proceedings **171,** 65.
GEGUZIN, Ya.E. and M.A. KRIVOGLAZ, 1973, Migration of Microscopic Inclusions in Solids (Consultants' Bureau, NewYork) p. 157.
GERTSMAN, V., A.A. NAZAROV, A.E. ROMANOV, R.Z. VALIEV and V.I. VLADIMIROV, 1989, Phil. Mag. **A59,** 1113.
GLEITER, H., 1971, Phys. Stat. Sol. (b) **45,** 9.
GLEITER, H., 1979, Acta Metall. **27,** 1754.
GLEITER, H., 1981a, Chalmers Anniversary Volume, Prog. Mater. Sci., eds. J.W. Christian, P. Haasen and T. B. Massalski (Pergamon Press, Oxford).
GLEITER, H., 1981b, Proceedings Second Risø International Symposium on Metallurgy and Materials Science, eds. N. Hansen, T. Leffers and H. Lilholt, Røskilde, Denmark, p. 15.
GLEITER, H., 1982, Mater. Sci. Eng. **52,** 91.
GLEITER, H., 1989, Progress Materials Science, eds. J.W. Christian, P. Haasen and T.P. Massalski, Vol. **33** (4), 223.
GLEITER, H., 1992, Nanostructured Materials **1,** 1.
GLEITER, H., 1995, Nanostructured Materials **6,** 3.
GLEITER, H. and B. CHALMERS, 1972, Prog. Mater. Sci. **16,** 145.
GLEITER, H., S. MAHAJAN and K.J. BACHMANN, 1980, Acta Metall. **28,** 1603.
GORLIK, S.S., L. KOVALEVA and M. BLAUTER, 1972, Fiz. Met. Metalloved. **33(3),** 658.
GOTTSCHALK, C., K. SMIDODA and H. GLEITER, 1980, Acta Metall. **28,** 1653.

GRAHAM, L. D. and R. W. KRAFT, 1966, Metallurg. Trans. **236,** 94.
GRATIAS, D. and A. THALAL, 1988, Phil. Mag. Letters **57,** 63.
GREENWOOD, G. W., 1956, Acta Metall. **4,** 243.
GREENWOOD, G. W., H. JONES and J. H. WESTBROOK, 1975, Phil. Mag. **31,** 39.
GULDEN, M. E., 1969, J. Nucl. Mater. **30,** 30.
GUYOT, C. and M. WINTENBERGER, 1974, J. Mater. Sci. **9,** 614.
HAESSNER, F., S. HOFFMANN and H. SEKEL, 1974, Scripta Metall. **8,** 299.
HAHN, W., 1994, private communication.
HAKEN, H., 1978, Synergetics, (Springer Verlag), Berlin.
HALPERIN, W. P., 1986, Rev. Mod. Phys. **58,** 566.
HARASE, J., R. SHIMIZU and T. WATANABE, 1988, Eighth Int. Conf. on Textures in Metals, eds.: J. S. Kallend and G. Gottstein, The Metallurgical Society, Warrendale, PA, p. 723.
HASEEB, A., B. BLANPAIN, G. WONTERS, J. P. CELIS and J. R. Roos, 1993, Mater. Sci. and Eng. **A168,** 137.
HAUBOLD, T., 1993, Acta Metall. et Mater. **41,** 1769.
HENDERSON, D., W. JOST and M. MCLEAN, 1978, Met. Sci. J. **12,** 113.
HENGLEIN, A., 1988, Topics in Current Chemistry, (Springer Verlag, Berlin), Vol. **143,** p. 113.
HERR, U., J. JING, U. GONSER and H. GLEITER, 1990, Solid State Comm. **76,** 197.
HERRING, C., 1950, J. Appl. Phys. **21,** 301.
HERRING, C., 1953, Structure and Properties of Solid Surfaces, eds. R. Gomer and C. S. Smith, (University of Chicago Press), Chicago, p. 4.
HERRMANN, G., H. GLEITER and G. BAERO, 1976, Acta Metall. **24,** 353.
HIGASHI, K., 1993, Mater. Sci. and Eng. **A166,** 109.
HILLERT, M., 1965, Acta Metall. **13,** 227.
HIRABAYASHI, M., 1959, J. Phys. Soc. Jap. **14,** 149.
HIRAGA, K., 1973, Phil. Mag. **27,** 1301.
HO, P. and C. G. WEATHERLY, 1975, Acta Metall. **23,** 1451.
HO, P. S. and J. K. KIRKWOOD, 1974, J. Appl. Phys. **45,** 3229.
HOEVEL, H., S. FRITZ, A. HILGER, U. KREIBIG and M. VOLLMER, 1993, Phys. Rev. **B48,** 18178.
HOLZ, A., 1979, Physica 97, **A75.**
HONDROS, E. D., 1993, Mater. Sci. and Eng. **A166,** 1.
HORNBOGEN, E. and U. KÖSTER, 1982, Recrystallization of Metallic Materials, ed. F. Haessner (Riederer Verlag, Stuttgart) p. 159.
HORNBOGEN, E., 1984, Acta metall. mater. **32,** 615.
HORNBOGEN, E., 1986, J. Mater. Sci. **21,** 3737.
HORNBOGEN, E., 1989, Internat. Materials Rev. **34,** 277.
HOUGHTON, D. C. and D. JONES, 1978, Acta Metall. **26,** 695.
HUNDERI, O. and N. RYUM, 1979, Acta Metall. Mater. **27,** 161.
HUNDERI, O. and N. RYUM, 1981, Acta Metall. Mater. **29,** 1737.
JAIN, S. C. and A. E. HUGHES, 1978, J. Mater. Sci. **13,** 1611.
JANG, H., D. N. SEIDMAN and K. L. MERKLE, 1993, Interface Science, **1,** 61.
JING, J., A. KRAEMER, R. BIRRINGER, H. GLEITER and U. GONSER, 1989, J. Non-Cryst. Solids, **113,** 167.
JOHNSON, K. H. and S. V. PEPPER, 1982, J. Appl. Phys. **53,** 6634.
JOHNSON, R. A. and M. G. LAM, 1976, Phys. Rev. **B13,** 434.
JOHNSON, W. C. and J. K. LEE, 1979, Metallurg. Trans. **10A,** 1141.
JOHNSON, W. C., 1984, Acta Metall. Mater. **32,** 465.
JOHNSON, W. C. and J. I. D. ALEXANDER, 1986, J. Appl. Phys. **59,** 2735.
JONES, D. R. and G. J. MAY, 1975, Acta Metall. **23,** 29.
JUNG, P. and K. TRENZINGER, 1974, Acta Metall. **22,** 123.
KAHLWEIT, H., 1975, Adv. Colloid and Interface Sci. **5,** 1.
KARCH, J. and R. BIRRINGER, 1990, Ceramics International **16,** 291.
KEAR, B. H. and L. E. MCCANDLISH, 1993, Nanostructured Materials **3,** 19.
KHATCHATURYAN, A. G., 1969, Phys. Stat. Sol. **35,** 119.
KHATCHATURYAN, A. and G. SHATALOV, 1969, Sov. Phys. Solid State JETP **11,** 118.

KING, A. H., 1993, Materials Science Forum **126–128,** 221.
KIRCHNER, H., 1971, Metallurg. Trans. **3,** 2861.
KIRK, W. P. and M. A. REED, 1992, Nanostructures and Mesoscopic Systems, Proceedings of an International Symposium held at Santa Fe, New Mexico 20–24 May 1991, (Academic Press, Boston, San Diego, New York), p. 1.
KOHN, W. and L. J. SHAM, 1965, Phys. Rev. **140,** A1133.
KRONBERG, M. L. and F. H. WILSON, 1949, Trans. AIME **185,** 501.
KUHLMANN-WILSDORF, D., 1965, Phys. Rev. **140,** A1599.
KUNC, M. and R. M. MARTIN, 1981, Phys. Rev. **B24,** 3445.
LANGER, J. S. and R. SEKERKA, 1975, Acta Metall. **23,** 1225.
LARCHE, F. C. and J. W. CAHN, 1973, Acta Metall. Mater. **21,** 1051.
LARCHE, F. C. and J. W. CAHN, 1978, Acta Metall. Mater. **26,** 1579.
LEHMANN, V. and U. GÖSELE, 1991, Appl. Phys. Lett. **58,** 856.
LEMMLEIN, G. G., 1952, Dokl. Adad. Neuk SSSR **85,** 325.
LI, J. C. M., 1961, J. Appl. Phys. **32,** 525.
LI, J . C. M ., 1969, Trans. Met. Soc. AIME **245,** 1591.
LIFSHITZ, I. M. and V. V. SLYOZOV, 1961, J. Phys. Chem. Solids **19,** 35.
LIVINGSTON, J. D., 1971, J. Mater. Sci. **7,** 61.
LIVINGSTON, J. D. and J. W. CAHN, 1974, Acta Metall. **22,** 495.
LOEFFLER, J., J. WEISMUELLER and H. GLEITER, 1995, Nanostructured Materials **6,** 567.
LORIMER, G. W. and R. B. NICHOLSON, 1969, Acta Metall. **13,** 109.
LORMAND, G., J. ROUAIS and C. EYRAND, 1974, Acta Metall. **22,** 793.
LOUAT, N. P., 1974, Acta Metall. **22,** 721.
LOUIE, S. G. and M. L. COHEN, 1976, Phys. Rev. **B13,** 2461.
LOUIE, S. G., J. G. CHELIKOWSKY and M. L. COHEN, 1977, Phys. Rev. **B15,** 2154.
LU, K., J. T. WANG and W. D. WEI, 1991, J. Appl. Phys. **69,** 522.
MAC DOWELL, J. F. and G. H. BEALL, 1969, J. Am. Ceram. Soc. **52,** 117.
MAIER, J., S. PRILL and B. REICHERT, 1988, Solid State Ionics **28–30,** 1465.
MANTHIRAM, A., D. L. BOURELL and H. L. MARCUS, 1993, Journal of Metals **11,** November 1993, 67.
MARQUARDT, P., G. NIMTZ and B. MUEHLSCHLEGEL, 1988, Solid State Comm. **65,** 539.
MARQUARDT, P. and H. GLEITER, 1980, Verhandlungen der Deutsch. Physikal. Gesellsch. **15,** 328.
MARRA, W. C., P. EISENBERGER and A. Y. CHO, 1979, J. Appl. Phys. **50,** 6927.
MARTIN, G. and L. P. KUBIN, 1988, editors, Nonlinear Phenomena in Materials Science, Vols. 3 and 4 of Solid State Phenomena (Trans. Tech. Aedermannsdorf, Switzerland).
MARTIN, J. W. and R. D. DOHERTY, 1976, Stability of Microstructure in Metallic Systems (Cambridge University Press) p. 154. (Second edition, 1996, in press).
MARTUSCELLI, E., R. PALUMBO and M. KRYSZEWSKI, 1980, Polymer Blends, Plenum Press, NewYork, p. 1.
MASAMURA, R. A. and M. E. GLICKSMAN, 1974, Can. Met. Quest. **13,** 43.
MAURER, R. and H. GLEITER, 1985, Scripta Metall. **19,** 1009.
MAURER, R. D., 1956, J. Chem. Phys. **25,** 1206.
MAURER, R. D., 1959, J. Chem. Phys. **31,** 244.
MAY, J. E. and D. TURNBULL, 1958, Trans. Metall. Soc. AIMF **212,** 769.
MAYO, M. J. and D. C. HAGUE, 1993, Nanostructured Materials **3,** 43.
MCCANDLISH, L. E., B. H. KEAR and B. K. KIM, 1990, Materials Science and Technology, **6,** 953.
MCLEAN, M., 1973, Phil. Mag. **27,** 1235.
MCLEAN, M ., 1978, Met. Sci. J. **12,** 113.
MCLEAN, M., 1982, Met. Sci. J. **16,** 31.
MCMAHON G., 1994, Ph. D. Thesis Universität des Saarlandes, FB 15, 66041 Saarbruecken, Germany.
MCMICHAEL, R. D., R. D. SHULL, L. H. BENNETT, C. D. FUERST and J. F. HERBST, 1993, Nanostructured Materials **2,** 277.
MENDEZ, E. E. and K. VON KLITZING, 1989, Physics and Applications of Quantum Wells and Superlattices, NATO Advanced Studies Series, Series B: Physics, Vol. **170.**
MERKLE, K. L., J. F. REDDY, C. L. WILEY and D. J. SMITH, 1987, Phys. Rev. Letters **59,** 2887.

MIGAZAKI, T., K. NAKAMURA and H. MORI, 1979, J. Mater. Sci. **14,** 1827.
MORI, T., P. CHENG, M. KATO and T. MURA, 1978, Acta Metall. **26,** 1435.
MORRALL, J. E. and N. P. LOUAT, 1974, Scripta Metall. **8,** 91.
MULLINS, W. W., 1956, Acta Metall. **4,** 421.
MURTY, B. S., M. M. RAO and S. RANGANATHAN, 1993, Nanostructured Materials **3,** 459.
NES, E., 1974, Acta Metall. **22,** 81.
NEUHAEUSER, H. J. and W. PITSCH, 1971, Z. Metalik. **62,** 792.
NICHOLS, F. A., 1976, J. Mater. Sci. **11,** 1077.
NICOLIS, G. and I. PRIGOGINE, 1977, Self Organization in Non-Equilibrium Systems, Wiley-Interscience New York.
NIIHARA, K., 1991, J. Ceram. Soc. Japan, **99,** 974.
OEHRING, M., Z. H. YAN, T. KLASSEN and R. BORMANN, 1992, phys. stat. solidi **(a)131,** 671.
OEHRING, M. and R. BORMANN, 1991, Mater. Sci. and Eng. **A134,** 1330.
ORIANI, R. A., 1964, Acta Metall. **12,** 1399.
OSMOLA, D., P. NOLAN, U. ERB, G. PALUMBO and K. T. AUST, 1992, phys. stat. sol. **(a)131,** 569.
OZAWA, T. and Y. ISHIDA, 1977, Scripta Metall. **11,** 835.
OZIN, G. A., 1992, Advanced Materials **4,** 612.
PALUMBO, G., P. J. KING, K. T. AUST, U. ERB and P. C. LICHTENBERGER, 1991a, Scripta Metall. **25,** 1775.
PALUMBO, G., D. M. DOYLE, A. M. EL-SHERIK, U. ERB and K. T. AUST, 1991b, Scripta Metall. et Mater. **25,** 679.
PASHLEY, D. W., M. H. JAKOBS and J. T. VIETZ, 1967, Phil. Mag. **16,** 51.
PAUL, A., 1975, J. Mat. Sci. **10,** 415.
PAYNE, M. C., P. D. BRISTOWE and J. D. JOANNOPOULOS, 1985, Phys. Rev. Lett. **58,** 1348.
PERKOVIC, V., C. R. PURDY and L. M. BROWN, 1979, Acta Metall. **27,** 1075.
PETERMANN, J., 1991, Bulletin of the Institute of Chemical Research, Kyoto University **69,** 84.
PHILLPOT, S. R., D. WOLF and S. YIP, 1990, MRS Bulletin **11,** 38.
POIRIER, J. and J. M. DUPOUY, 1979, Proc. Int. Conf. on Irradiation Behaviour of Metallic Materials for Reactor Core Compounds, Ajaccio, Corsica (publ. by CEA-DMCEN, 91190, Gif-sur-Yvette, France).
POND, R. C. and V. VITEK, 1977, Proc. Roy. Soc. **A357,** 453.
POND, R. C., D. SMITH and V. VITEK, 1978, Scripta Metall. **12,** 699.
PONTIKIS, V., 1988, J. Physique **49,** C5–327.
POTAPOV, L. P., B. F. GLOWIN and P. H. SHIRYAEV, 1971, Fiz. Met. Metalloved. **32,** 227.
POWELL, R. E. and H. EYRING, 1943, J. Am. Ceram. Soc. **65,** 648.
RADLINSKI, A. P. and A. CALKA, 1991, Mater. Sci. and Eng. **A134,** 1376.
RAHMAN, A., 1977, Correlation Functions and Quasiparticle Interactions in Condensed Matter, NATO Adv. Stud. Ser. **35,** Plenum Press, New York, p. 37.
RAYLEIGH, LORD, 1878, Proc. Lond. Math. Soc. **10,** 4.
READ, W. T. and W. SHOCKLEY, 1950, Phys. Rev. **78,** 275.
RIVIER, N., 1986, J. Physique **47,** C3–299.
ROGERS, J. T., H. M. FLOWERS and R. RAWLINGS, 1975, Met. Sci. **9,** 32.
ROY, R., 1972, Advances in Nucleation and Crystallization in Glasses, eds. L. L. Heck and S. Freiman, Am. Cer. Soc., Columbus, Ohio, USA, p. 57.
RÜHLE, M., K. BURGER and W. MADER, 1986, J. Microsc. Spectr. Electron. **11,** 163.
RÜHLE, M., M. BACKHAUS-RICOULT, K. BURGER and W. MADER, 1987, Ceramic Microstructure, Plenum Press New York, p. 295.
RÜHLE, M. and A. G. EVANS, 1989, Mater. Sci. and Eng. **A107,** 187.
RÜHLE, M., A. H. HEUER, A. G. EVANS and M. F. ASHBY, 1992, Proc. Internat. Symp. on Metal-Ceram. Interfaces, Acta metall. mater. **40,** 1.
RYAZANOV, A. I. and L. A. MAXIMOV, 1981, Rad. Effects **55,** 165.
SASS, S. L., 1980, J. Appl. Cryst. **13,** 109.
SASS, S. L. and P. D. BRISTOWE, 1980, Grain Boundary Structure and Kinetics, eds. R. W. Balluffi, Metals Park Ohio, American Metals Soc., p. 71.
SAUTHOFF, G., 1976, Scripta Metall. **10,** 557.

SCHLUMP, W. and J. WILLBRAND, 1992, VDI Nachrichten **917,** 23.
SCHMIDT, G., 1992, Mat. Res. Soc. Sympos. Proceedings **274,** 121.
SCHONBERGER, U., O. K. ANDERSON and M. METHFESSEL, 1992, Acta Metall. Mater. **40,** 1.
SEEGER, A. and G. SCHOTTKY, 1959, Acta Metall. **7,** 495.
SHINGU, P. H, B. HUANG, J. KUYAMA, K. N. ISHIHARA and S. NASU, 1989, in New Materials by Mechanical Alloying, eds. E. Arzt and L. Schultz (DGM Verlag Oberursel), p. 319.
SHULL, R. D., 1993, Nanostructured Materials **2,** 213.
SIEGEL, R. W., 1993, Mater. Sci. and Eng. **A168,** 189.
SILCOCK, J. M. and W. T. TUNSTALL, 1964, Phil. Mag. **10,** 361.
SIMPSON, C. J., K. T. AUST and C. WINEGARD, 1971, Metall. Trans. **2,** 987.
SMIDODA, K., CH. GOTTSCHALK and H. GLEITER, 1978, Acta Metall. **26,** 1833.
SMITH, C. S., 1948, Trans. AIME **175,** 15.
SMITH, C. S., 1952, Metal Interfaces, Amer. Soc. for Metals, Cleveland, Ohio, USA, p. 65.
SMITH, C. S., 1954, Met. Rev. **9,** 1.
SMITH, D. A. and R. C. Pond, 1976, Internat. Met. Rev. **205,** 61.
STEWART, 1972, Introduction to Glass Science, eds. L. D. Pye, H. J. Stevens, W. C. LaCourse (Plenum Press New York, USA), p. 237.
STIEGLER, J. O. and K. FARRELL, 1974, Scripta Metall. **8,** 651.
STONEHAM, A. M., 1971, J. Phys. **F1,** 118.
STONEHAM, A. M. and P. W. TASKER, 1988, Surface and Near Surface Chemistry of Oxide Materials, eds. J. Nowotny and L. C. Dufour (Elsevier Publ., Amsterdam), p. 1.
SURYANARAYANA, C. and F. H. FROES, 1992, Met. Trans **A23,** 1071.
SUTTON, A. P. and R. W. BALLUFFI, 1987, Acta Metall. **35,** 2177.
SUTTON, A. P., 1988, Interfacial Structure, Properties and Design, in: Mat. Res. Soc. Symp. Proc. **122,** 43 (see also *Further reading*).
SUTTON, A. P., 1989, Phase Transitions **16/17,** 563.
SUTTON, A. P., 1990, J. de Physique suppl no 1 **51,** C1–35.
SUTTON, A. P. and R. W. BALLUFFI, 1995, Interfaces in Crystalline Materials. Oxford University Press.
TANAKOV, M. YU., L. I. TRUSUV and B. YA. LJUBOV, 1991, Scripta Metall. et Mater. **25,** 413.
TEWARY, V. K., 1973, J. Phys. **F3,** 1275.
TIAPKIN, YU. D., N. T. TRAVINA and T. V. YEVTSUSHENKO, 1976, Scripta Metall. **10,** 375.
TIEN, J. and S. COPLEY, 1971, Metallurg. Trans. **2,** 215.
TILLER, W. A. and R. SCHRIEFFER, 1974, Scripta Metall. **8,** 487.
TONG, H. Y., B. Z. DING, J. T. WANG, K. LU, J. JIANG and J. ZHU, 1992, J. Appl. Phys. **72,** 5124.
TRINKHAUS, H., C. ABROMEIT and J. VILLAIN, 1989, Phys. Rev. **B40,** 12531.
TSCHOEPE, A. and J. YING, 1995, Nanostructured Materials, **6,** 1005.
TURNBULL, D., 1951, Trans. AIME **191,** 661.
TURNBULL, D., J. S. C. JANG and C. C. KOCH, 1990, J. Mat. Res. **5,** 1731.
TYLER, S. K. and P. J. GOODHEW, 1980, J. Nucl. Mater. **92,** 201.
UBBELOHDE, A. R., 1965, Melting and Crystal Structure (Oxford Univ. Press).
VAN DER WALLE, C. G. and R. M. MARTIN, 1985, J. Vac. Sci. Techn. **B3,** 1256.
VEITH, M. and K. KUNZE, 1991, Angew. Chem. **103,** 845.
VEITH, M., D. KAEFER, J. KOCH, P. MAY, L. STAHL, V. HUCH, 1992, Chem. Ber. **125,** 1033.
VEPREK, S. and F. A. SAROTT, 1987, Phys. Rev. **B36,** 3344.
VOLKL, J., 1972, Ber. Bunsen Gesell. **76,** 797.
WAGNER, C., 1961, Z. Elektrochem. **65,** 581.
WARLIMONT, H. and G. THOMAS, 1970, Met. Sci. J. **4,** 47.
WARREN, B. E., 1937, J. Appl. Phys. **8,** 645.
WASYNCZUK, J. A. and M. RÜHLE, 1987, Ceramic Microstructure '86: Role of Interfaces, eds.: J. A. Pask and A. G. Evans (Plenum Press, New York), p. 87.
WATANABE, T., 1984, Res. Mechanica **2,** 47.
WATANABE, T., 1993, Mater. Sci. and Eng. **A166,** 11.
WEATHERLY, G. C. and Y. G. NAKAGAWA, 1971, Scripta Metall. **5,** 777.

WEISSMUELLER, J., W. KRAUSS, T. HAUBOLD, R. BIRRINGER and H. GLEITER, 1992, Nanostructured Materials **1,** 439 and ibid **3,** 261.
WEINS, M., H. GLEITER and B. CHALMERS, 1971, J. Appl. Phys. **42,** 2639.
WERT, J., 1976, Acta Metall. **24,** 65.
WHITMAN, W. D ., 1926, Amer. J. Sci., Ser. 5, **11,** 126.
WILLIS, J. R., 1975, Mech. Phys. Sol. **23,** 129.
WILSON, W. L., P. F. SZAJOWSKI and L. E. BRUS, 1993, Science **262,** 1242.
WINGROVE, M. and D. M. TAPLIN, 1969, J. Mater. Sci. **4,** 789.
WIRTH, R. and H. GLEITER, 1981a, Acta Metall. **29,** 1825.
WIRTH, R. and H. GLEITER, 1981b, J. Mater. Sci. **16,** 557.
WITTMER, M., 1985, Mat. Res. Soc. Symp. Proc. **40,** 393.
WOLF, D., 1985, J. Physique **46,** C4–197.
WOLF, D., 1990, J. Appl. Phys. **68,** 3221.
WOLF, D., 1991, Philos. Mag. **A63,** 1117.
WOLF, D. and S. YIP, eds. 1992, Materials Interfaces, Chapman and Hall, London, p. 1 and 139.
WUERSCHUM, R., W. GREINER and H.-E. SCHAEFER, 1993, Nanostructured Materials **2,** 55.
YOSHIZAWA, Y., S. OGUMA and K. YAMAUCHI, 1988, J. Appl. Phys. **64,** 6044.
ZACHARIASEN, W. H., 1932, J. Am. Chem. Soc. **54,** 3841.

Further reading

For further reading we refer to the review articles mentioned in the various sections.

Since this chapter was written, a major text has been published: A. P. Sutton and R. W. Balluffi: "Interfaces in Crystalline Materials". (Oxford University Press, 1995).

– SUBJECT INDEX –

1st Volume: Pages 1–942
2nd Volume: Pages 943–1830
3rd Volume: Pages 1831–2740

"page number ff" signifies that treatment of the topic continues on the following page(s).